JOINT INSTITUTE FOR AERONAUTICS AND ACOUSTICS

National Aeronautics and
Space Administration
Ames Research Center

JIAA TR - 86

Stanford University

NUMERICAL STUDY OF DELTA WING LEADING EDGE BLOWING

BY

David Yeh, Domingo Tavella, and Leonard Roberts

(NASA-CR-183101) NUMERICAL STUDY OF DELTA WING LEADING EDGE BLOWING (Stanford Univ.) 130 p CSCL 01A

N88-26335

Unclas
G3/02 0153009

Stanford University
Department of Aeronautics and Astronautics
Stanford, CA 94305

JULY 1988

Abstract

The vortical flow over a delta wing contributes an important part of the lift - the so called nonlinear vortex lift. Controlling this vortical flow with its favorable influence would enhance the maneuverability and control of the aircraft. Several experiments have revealed that spanwise and tangential leading edge blowing can be applied as a means of controlling the position and strength of the leading edge vortices. The present research studies these effects by numerical solution of the three-dimensional Navier-Stokes equations. The leading edge jet is simulated by defining a permeable boundary, corresponding to the jet slot, where suitable boundary conditions are implemented. Numerical results are shown to compare favorably with experimental measurements. It is found that the use of spanwise leading edge blowing at moderate angle of attack magnifies the size and strength of the leading edge vortices, and moves the vortex cores outboard and upward. The increase in lift primarily comes from the greater nonlinear vortex lift. However, spanwise blowing causes earlier vortex breakdown, thus decreasing the stall angle. The effects of tangential blowing at low to moderate angles of attack tend to reduce the pressure peaks associated with leading edge vortices and to increase the suction peak around the leading edge, such that the integrated value of the surface pressure remains about the same. Tangential leading edge blowing in post-stall conditions is shown to re-establish vortical flow and delay vortex bursting, thus increasing $C_{L_{max}}$ and stall angle.

PRECEDING PAGE BLANK NOT FILMED

Acknowledgements

This research was supported by NASA Grant NCC 2-341.

Contents

1 Introduction 1

1.1 Motivation 1

1.2 Previous Work 4

1.2.1 Experimental Evidence 4

1.2.2 Theoretical Work 6

1.3 Present Approach 8

2 Governing Equations and Numerical Method 14

2.1 Governing Equations and Approximations 14

2.1.1 The Navier-Stokes Equations 15

2.1.2 Coordinate Transformation 17

2.1.3 Thin-Layer Approximation 20

2.2 Numerical Algorithm 22

2.2.1 Beam and Warming Algorithm 22

2.2.2 The LU-ADI Algorithm 24

2.2.3 Numerical Dissipation Model 28

2.2.4 Turbulence Model 30

3 Spanwise Blowing **35**

3.1 Introduction 35

3.2 Grid Generation 36

3.3 Boundary and Jet-Exit Conditions 38

3.4 Results and Physical Interpretation 40

3.4.1 No Blowing 40

3.4.2 Spanwise Blowing 43

4 Tangential Blowing **61**

4.1 Introduction 61

4.2 Multiple-Grid Concept and Grid Generation 62

4.3 Boundary and Jet-Exit Conditions 65

4.4 Results and Physical Interpretation 67

4.4.1 No Blowing 67

4.4.2 Tangential Blowing 70

5 Conclusions and Recommendations **96**

5.1 Conclusions 96

5.2 Recommendations 98

A Jacobian Matrices **100**

B Similarity Transformation Matrices **102**

C Calculation of the Jet Momentum **105**

List of Figures

1.1 Illustration of vortex flow over a delta wing (Bird, Ref. 1). 10

1.2 Schematic representation of the lift characteristics of a delta wing (Hummel, Ref. 2). 11

1.3 Schematic view of a delta wing with spanwise leading edge blowing. 12

1.4 Schematic view of a conical delta wing with tangential leading edge blowing. 13

3.1 Outer boundary (side view) generated by a two-dimensional hyperbolic grid generation method about a delta wing. 47

3.2 Close-up view of a typical chordwise station of a delta wing. 48

3.3 Partial view of the computational domain. 49

3.4 Particle traces emanating near the leading edge of a 70°-sweep delta wing at $\alpha = 10°$ ($C_\mu = 0$). 50

3.5 Particle traces emanating near the leading edge on the conical projection plane at $x/c_0 = 0.5$, $\alpha = 10°$ ($C_\mu = 0$). 51

3.6 Computed spanwise surface pressure coefficient (C_p) distribution at $x/c_0 = 0.5$, $\alpha = 10°$ ($C_\mu = 0$). 51

3.7 Computed near-surface flow pattern for a 70°-sweep delta wing at $\alpha = 10°$ ($C_\mu = 0$). 52

3.8 Schematic view of vortical flow pattern on the upper surface of a delta wing (Ref. 50). 52

3.9 Particle traces emanating near the leading edge of a 70°-sweep delta wing without blowing and with blowing ($C_\mu = 0.047$) at $\alpha = 10°$. . 53

3.10 Effect of spanwise blowing on the vortex traces on the conical projection plane at $x/c_0 = 0.5$, $\alpha = 10°$, for $C_\mu = 0.$, .0235, .0470, .094. 54

3.11 Effect of spanwise blowing on surface pressure distribution at $x/c_0 = 0.5$, $\alpha = 10°$, for $C_\mu = 0.$, .0094, .0235, .0470. 56

3.12 Computed near-surface flow pattern for no blowing (on the left) and $C_\mu = .0705$ (on the right) cases at $\alpha = 10°$. 57

3.13 Comparison of computed and experimental results for a delta wing of AR = 1.4 with leading edge blowing at $\alpha = 10°$. 58

3.14 Variation of computed normal force coefficient with angle of attack for $C_\mu = 0$ and 0.05 59

3.15 Negative-u velocity contours for the no-blowing case at $x/c_0 = 0.77$, $\alpha = 40°$. 60

3.16 Negative-u velocity contours for the blowing case ($C_\mu = 0.05$) at $x/c_0 = 0.77$, $\alpha = 40°$. 60

4.1 Jet-slot geometry and location in the cross-flow plane. 74

4.2 Illustration of Grid 1 arrangement in the cross-flow plane. 75

4.3 Illustration of Grid 2 and Grid 3 arrangements in the cross-flow plane. 75

4.4 Turbulent wall jet velocity profile in tangential blowing. 76

4.5 Delta wing geometry used in the tangential blowing simulations. . . 77

4.6 Illustration of vortex structure with particle traces for $\alpha = 30°$, $C_\mu = 0$. 78

4.7 Illustration of vortex structure with particle traces for $\alpha = 40°$, $C_\mu = 0$. 79

4.8 Reverse-flow velocity contours at selected chordwise locations, $x/c_0 = .17, .29, .42, .54, .67, .79, .92$, for $C_\mu = 0$, $\alpha = 40°$. 80

4.9 Normalized total pressure contours at $x/c_0 = 0.36$ for $\alpha = 30°$ and $\alpha = 40°$ ($C_\mu = 0$). 81

4.10 Comparison of computed spanwise surface pressure distribution with experimental results at $x/c_0 = 0.36$ for $\alpha = 30°$, $40°$ ($C_\mu = 0$). . . . 82

4.11 Computed near-surface streamline patterns for $\alpha = 30°$ and $\alpha = 40°$ ($C_\mu = 0$). 83

4.12 Computed normal force coefficient as a function of angle of attack for $C_\mu = 0$. 84

4.13 Illustration of vortex structure with particle traces, for $\alpha = 30°$, $C_\mu = 0.05$. 85

4.14 Illustration of vortex structure with particle traces, for $\alpha = 40°$, $C_\mu = 0.038$. 86

4.15 Reverse-flow (negative-u) velocity contours at selected chordwise locations, $x/c_0 = .17, .29, .42, .54, .67, .79, .92$, for $\alpha = 40°$, $C_\mu = 0.038$. 87

4.16 Normalized total pressure contours at $x/c_0 = 0.36$ for $\alpha = 30°$, $C_\mu = 0.05$ and $\alpha = 40°$, $C_\mu = 0.038$. 88

4.17 Comparison of computed spanwise surface pressure distribution with experimental results, for $\alpha = 30°$, $C_\mu = 0.05$ and $\alpha = 40°$, $C_\mu =$ 0.0.38 89

4.18 Computed spanwise surface pressure distributions for $\alpha = 30°$, $x/c_0 =$ 0.36, with $C_\mu = 0$ and $C_\mu = 0.05$. 90

4.19 Computed velocity profiles near the leading edge for $\alpha = 30°$, $x/c_0 =$ 0.36, with $C_\mu = 0$ and 0.05. 91

4.20 Computed spanwise surface pressure distributions for $\alpha = 40°$, $x/c_0 =$ 0.36, with $C_\mu = 0$ and 0.038. 92

4.21 Computed velocity profiles near the leading edge for $\alpha = 40°$, $x/c_0 =$ 0.36, with $C_\mu = 0$ and 0.038. 93

4.22 Computed near-surface flow patterns, for $\alpha = 30°$, $C_\mu = 0.05$ and $\alpha = 40°$, $C_\mu = 0.038$. 94

4.23 Effect of tangential leading edge blowing on total wing normal force ($C_\mu = 0$ and 0.05). 95

C.1 Velocity magnitude distribution over a small trapezoidal cell. 106

List of Tables

1.1 Flow regimes as a function of angle of attack. 11

3.1 Effects of spanwise leading blowing on total wing normal force (C_μ = 0 and 0.05). 59

4.1 Effects of tangential leading blowing on total wing normal force (C_μ = 0 and 0.05). 95

List of Principal Symbols

a	speed of sound
a_∞	free stream speed of sound
$\hat{A}$	flux Jacobian matrix in the ξ-direction
A_j	projected area of the jet slot perpendicular to the spanwise direction
AR	delta wing aspect ratio
b	half width of a wall jet at the location of $u = \frac{1}{2}u_m$
$\hat{B}$	flux Jacobian matrix in the η-direction
c_0	length of the root chord
$\hat{C}$	flux Jacobian matrix in the ζ-direction
C_L	lift coefficient
Cp	pressure coefficient
C_p	specific heat at constant pressure
C_μ	blowing momentum coefficient, $\frac{Jet\ Momentum}{q_\infty\ S_{wing}}$
$D_e\|_k$	explicit artificial dissipation terms ($k = \xi$, η or ζ)
$D_i\|_k$	implicit artificial dissipation terms ($k = \xi$, η or ζ)
D_ξ, D_η, D_ζ	diagonal matrices associated with the LU-ADI algorithm (Sec. 2.2.2)

e	total energy per unit volume
e_i	specific internal energy
$\vec{e}_s$	unit vector in the spanwise direction
$\vec{e}_Y, \vec{e}_Z$	unit vectors in the conical projection plane
E	inviscid flux vector in the x-direction
$\hat{E}$	inviscid flux vector in the ξ-direction
E_v	viscous flux vector in the x-direction
$\hat{E}_v$	viscous flux vector in the ξ-direction
F	inviscid flux vector in the y-direction
$\hat{F}$	inviscid flux vector in the η-direction
F_v	viscous flux vector in the y-direction
$\hat{F}_v$	viscous flux vector in the η-direction
$F(\zeta)$	function used in outer region of turbulence model
$F_{Kleb}(\zeta)$	Klebanoff intermittency factor
G	inviscid flux vector in the z-direction
$\hat{G}$	inviscid flux vector in the ζ-direction
G_v	viscous flux vector in the z-direction
$\hat{G}_v$	viscous flux vector in the ζ-direction
h	computational time step; local jet-slot width
I	identity matrix
J	transformation Jacobian
K_e	input constant associated with numerical dissipation (Eq. 2.40)
l	length scale for inner region of turbulence model
L_ξ, L_η, L_ζ	lower diagonal matrices associated with the LU-ADI algorithm (Sec. 2.2.2)

$\hat{\mathcal{L}}_\xi$, $\hat{\mathcal{L}}_\eta$, $\hat{\mathcal{L}}_\zeta$	Alternate Implicit Direction (ADI) operators
M	Mach number
M_∞	free stream Mach number
$\hat{M}$	viscous flux Jacobian matrix in the ζ-direction
$\mathcal{O}$	order of magnitude
p	pressure
p_∞	free stream pressure
P_n	component of the pressure gradient normal to the body surface
Pr, Pr_l	laminar Prandtl number
Pr_t	turbulent Prandtl number
q_∞	free stream dynamic pressure
Q	vector of conserved quantities in cartesian coordinates
$\hat{Q}$	vector of conserved quantities in body-conforming coordinates
R	leading edge radius of curvature
$\hat{R}^n$	right hand side of the finite difference form of the Thin-Layer Navier-Stokes equations
Re, Re_∞	free stream Reynolds number
s	local wing span
$\hat{S}$	viscous flux vector under the Thin-Layer approximation
S_{wing}	wing reference area
t	time
T_ξ, T_ξ^{-1}	similarity transformation matrix associated with flux Jacobian matrix $\hat{A}$
T_η, T_η^{-1}	similarity transformation matrix associated with flux Jacobian matrix $\hat{B}$
T_ζ, T_ζ^{-1}	similarity transformation matrix associated with flux Jacobian matrix $\hat{C}$
u, v, w	velocity components in the cartesian coordinates

$\tilde{u}$	ratio of the maximum negative-u velocity to the free stream velocity
u_m	wall jet maximum velocity
U_ξ, U_η, U_ζ	upper diagonal matrices associated with the LU-ADI algorithm (Sec. 2.2.2)
U, V, W	contravariant velocity components
V_c	cross-flow velocity magnitude
$V_{conical}$, $W_{conical}$	velocity components in the conical projection plane
V_{jet}	jet exit velocity
V_∞	free stream velocity
x, y, z	cartesian coordinates
X, Y, Z	conical coordinates
α	angle of attack
β_x, β_y, β_z	heat flux vector components
γ	ratio of specific heats
δ_ξ, δ_η, δ_ζ	central difference operators
Δ_ξ, Δ_η, Δ_ζ	forward difference operators
∇_ξ, ∇_η, ∇_ζ	backward difference operators
ϵ	numerical dissipation coefficient
ϵ_e	explicit numerical dissipation coefficient
ξ	longitudinal, circumferential and normal coordinates in body conforming system
ζ_m	normal distance from wing surface to where the maximum wall jet velocity occurs
κ	thermal conductivity coefficient
λ	bulk viscosity coefficient

$\hat{\Lambda}_\xi$	diagonal matrix associated with flux Jacobian matrix $\hat{A}$
$\hat{\Lambda}_\eta$	diagonal matrix associated with flux Jacobian matrix $\hat{B}$
$\hat{\Lambda}_\zeta$	diagonal matrix associated with flux Jacobian matrix $\hat{C}$
ν	kinematic viscosity coefficient
μ	viscosity coefficient; effective viscosity coefficient
μ_∞	free stream viscosity coefficient
μ_l	molecular (laminar) viscosity coefficient
μ_t	eddy (turbulent) viscosity coefficient
$\tilde{\mu}_t$	wall jet eddy (turbulent) viscosity coefficient
ρ	density
ρ_∞	free stream density
ρ_{jet}	jet density at exit plane
σ_κ	spectral radius of $\hat{\Lambda}_\kappa$; $\kappa = \xi$, η or ζ
τ	time in body conforming system
τ_{ij}	shear stress tensor, $i, j = x$, y or z
$\lvert\omega\rvert$	vorticity vector magnitude

Chapter 1

Introduction

1.1 Motivation

An improved understanding of the aerodynamics of slender, highly swept wings over a broad range of angle of attack is necessary for the design of aircraft having greater maneuverability and aerodynamic control. The low aspect ratio delta planform wing is typical of that used for highly maneuverable aircraft; the flow about such a wing is characterized by the presence of large scale, organized vortices on the leeward side of the wing which occur at moderate to high angles of attack. The formation of these vortices is responsible for the favorable "nonlinear" effects on the lift and may be used to advantage in both maneuvering and landing configurations. However, at the very high angles of attack attained during post-stall maneuvers, vortex breakdown can occur; *i.e.*, the vortices become unstable and unsteady, resulting in undesirable forces and moments acting on the wing.

The flow pattern about a delta wing can, in general, be classified into four regimes as a function of angle of attack, (table 1.1).

(I) At very low angles of attack, the flow remains attached and vortex-free. The lift is linear with angle of attack.

(II) At moderate to high angles of attack, the boundary layer on the lower surface flows outward and separates at the leading edge resulting in a free shear layer emanating from the edge. This free shear layer rolls up in a spiral fashion to form a pair of vortices on the leeward side of the wing, as shown in figure 1.1 . These vortices are characterized by being both stable and symmetric. A noticeable difference with regime (I), as illustrated in figure 1.2, is that the lift increases nonlinearly as angle of attack increases, due to the low pressure on the wing upper surface induced by the leading edge vortices. This is the so–called "nonlinear lift".

(III) At very large angles of attack, breakdown of the vortex structure occurs near the trailing edge and may be accompanied by an asymmetric and unsteady flow pattern. A distinct indication of the vortex breakdown is an abrupt increase in the cross-sectional area and turbulence level of the vortex cores. With further increase in angle of attack, the vortex breakdown progresses upstream and eventually the vortex system is totally burst. The adverse effects of both vortex breakdown and asymmetric vortices result in large, unfavorable changes in forces and moments on the wing.

(IV) At extremely large angles of attack (up to 90°), the flow on the leeward side is characterized by an unsteady wake and periodic vortex shedding. As a result, the forces acting on the wing are very unpredictable.

Highly maneuverable aircraft operate primarily in the flow regimes (II) and (III), where the "nonlinear" vortex lift can be used to aerodynamic advantage. Since the vortex flow for a delta wing plays such an important role in determining lift in these flow regimes, it is desirable to control these vortices with their favorable influences and thereby enhance maneuverability and control.

This leads to the motivation of present work which is to study leading edge blowing, either spanwise or tangential to the wing surface, as a means of controlling the influence of the leading edge vortices. There are two aspects of interest : one is to enhance the vortical lift at low to moderate angles of attack (in flow regime II); the other is to control and stabilize these leading edge vortices at high angles of attack to delay vortex breakdown (in flow regime III).

Since the leading edge is the region where the vortices are originated, it is logical to have a direct control over the vortical flow at its source. For other blowing concepts, interested readers are referred to spanwise blowing [3] - [10] that utilizes a discrete jet in a variety of blowing directions, and direct vortex core blowing [11] which is used to control vortex breakdown.

1.2 Previous Work

1.2.1 Experimental Evidence

Spanwise Leading Edge Blowing

Preliminary experiments by Trebble [12] on a 70° swept delta wing in the angle-of-attack (α) range of 0° to 16.4° have shown that lift gains (increase in C_L at a given incidence) are obtainable by ejecting a high-momentum jet in the spanwise direction from the leading edge of the wing, as depicted in figure 1.3 . The lift was measured by a force-balance and results demonstrated that there was no appreciable Reynolds number effect in the range of 0.35×10^6 to 1.05×10^6. Five different jet nozzle shapes were tested and the optimum nozzle shape proved to be a tapered slot which was expected to give a momentum distribution appropriate to preserve conical flow.

Alexander [13, 14] conducted a series of experiments on a 70° swept delta wing and a cropped delta wing with leading edge blowing for $\alpha = 0°$ to 25°. The results revealed that blowing increases the size and strength of the leading edge vortices and moves the cores outward and upward. The increase in lift is mainly due to an increase in the nonlinear contribution. In addition, the suppression of the secondary separation due to the entrainment of the leading edge jet was also observed in the experiment.

The same concept was applied to a straight wing and analyzed theoretically and experimentally by Tavella *et al.* [15, 16, 17] Although the dependence of the lift on the vortical flow for a delta wing and a straight wing is quite different, the outward

displacement of tip vortices by the jet and the effective increment of the wing span are observed in both cases.

Tangential Leading Edge Blowing

This blowing concept modifies the vortical flow by controlling the separation of the cross-flow boundary layer with a thin, high-momentum jet ejected tangentially to the leading edge surface. Experimental work on tangential leading edge blowing is more recent, and these investigations were carried out by Wood *et al.* [18, 19] These tests were conducted on a 60°-sweep conical delta wing with a rounded leading edge, as depicted in figure 1.4 . Experimental results show that the use of tangential blowing at post-stall angles of attack (tested up to $\alpha = 60°$) re-establishes vortical flow and delays vortex breakdown, thus increasing the $C_{L_{max}}$ and the stall angle. At pre-stall angles of attack, tangential leading edge blowing tends to reduce the suction peaks at the wing surface associated with the vortices, while increasing the suction peak around the leading edge such that the integrated value of the surface pressure remains about the same. The implication of this pre-stall characteristic of the lift response to blowing is that, when blowing is applied at a given post-stall angle, there is an optimum blowing coefficient to reach $C_{L_{max}}$. Once this maximum $C_{L_{max}}$ is reached, additional lift can not be obtained with further increase in blowing intensity. In other words, as the vortical flow is re-established due to blowing in post-stall conditions, the flow topology resembles that at lower angles of attack, but the lift is greater.

1.2.2 Theoretical Work

Spanwise Leading Edge Blowing

Barsby [20, 21] analyzed the flow field over a delta wing with spanwise blowing using the assumption of a conical flow field. He adapted the vortex-sheet model, applied by Mangler and Smith [22] to the study of leading edge separation, combined with the thin-jet model introduced by Spence [23] in the study of the jet flap. The jet is modeled as an infinitely thin vortex layer which carries a pressure difference between its upper and lower surfaces. This pressure jump across the sheet is proportional to the product of the momentum flux of the jet and the local curvature of the sheet and is related to the distribution of vorticity on the sheet.

In Barsby's solution procedure, the vortex sheet trace in the cross-flow plane is divided into vortex segments, and a concentrated vortex core is introduced which is joined to the last segment by a cut. Three separate nested iterations are performed :

(1) The pressure jump across the jet-vortex sheet is calculated at the center of each segment using the initial approximation for the shape of the sheet.

(2) The vortex position is adjusted by satisfying the force-free condition on the vortex segments, core and cut.

(3) The sheet shape is adjusted to satisfy the velocity tangency condition.

The procedure is repeated until the vortex sheet shape no longer varies. Blowing is shown to increase the lift on the wing and to increase the circulation about the vortex core, while displacing it upward and outboard.

Although Barsby's results closely resemble the actual flow field, general agreement between theoretical predictions and experimental results for subsonic flows is satisfactory only for the front portion of a delta wing. This limitation is due to the absence of the trailing edge in the conical assumption.

Recently, theoretical expressions for the effects of spanwise leading edge blowing were derived by Tavella [24]. In his analysis, the separated flow on the delta wing is represented by a model consisting of a pair of concentrated vortices connected to the leading edges by straight vortex sheets, originally proposed by Brown and Michael [25]. The blowing problem is solved implicitly in the cross-flow plane by requiring the singularity system to be force-free in the presence of the jet momentum. The predicted global quantities showed remarkable agreement with that in the experiments [12]. However, the lack of a detailed structure of the flow field in this analysis limits the insight that can be gained in the physics of spanwise blowing.

Barsby's and Tavella's analyses assume conical flow and therefore cannot account for the vortex breakdown phenomenon.

Tangential Leading Edge Blowing

Mourtos [26] studied the control of vortical separation on a circular cone by tangential blowing. This model utilizes an iterative procedure by matching the solutions of the viscous and the inviscid flow fields. The single line vortex model [27] was used for the inviscid solution, which is similar to that of Brown and Michael [25]. The integral form of the cross-flow boundary layer equation is solved to determine the location of the cross-flow separation point. This iteration continues until the pressure on the upper and lower separation points are matched.

The controlling of the separation point through tangential blowing is demonstrated in Mourtos' analysis as a means of influencing the strength and position of the vortices at low to moderate angles of attack. The predicted separation lines agree well with experiments [18, 19]. However, due to the simplicity of the inviscid model, the detailed flow field agrees only qualitatively with experiments [18, 19] (*i.e.* vortex location and strength). In particular, the absence of trailing edge condition precludes the use of this method to study vortex breakdown.

1.3 Present Approach

The objective of the present research is to study the effects of spanwise and tangential leading edge blowing on the vortical flow field over delta wings. The approach is to solve this three-dimensional problem using Computational Fluid Dynamics (CFD) techniques. The leading edge jet is simulated by defining a permeable boundary, corresponding to the jet slot, where suitable boundary conditions are implemented. A single-grid is used for the spanwise blowing calculations, whereas a multiple-grid zonal type of approach is required in the tangential blowing cases to accomodate the jet-slot geometry. A turbulence model for a wall jet developed by Roberts [28] is incorporated to accurately predict the location of the separation point in the tangential blowing calculations. Aided by available experimental evidence, the structure of the flow field is studied and analyzed through detailed graphical representations. The pressure field, including the surface pressure distribution on the wing, is computed and the variation of lift with angle of attack is determined, with and without blowing. These results are compared with the previous experimental results of Trebble [12] (for spanwise blowing) and Wood *et al* [18, 19]

(for tangential blowing). Such numerical experimentation not only enables one to gain physical insight in the flow field structure, but also reduces the number of configurations or models to be tested during preliminary design.

This work is divided into five chapters. The governing equations and numerical algorithms are presented in Chapter 2. Chapter 3 describes the implications of the spanwise leading edge blowing concept on vortical lift and its physical interpretation. Chapter 4 describes the effects of tangential leading edge blowing on the vortical flow field and its applications to post-stall conditions. Finally, Chapter 5 summarizes the results, presents conclusions and discusses recommendations for future work.

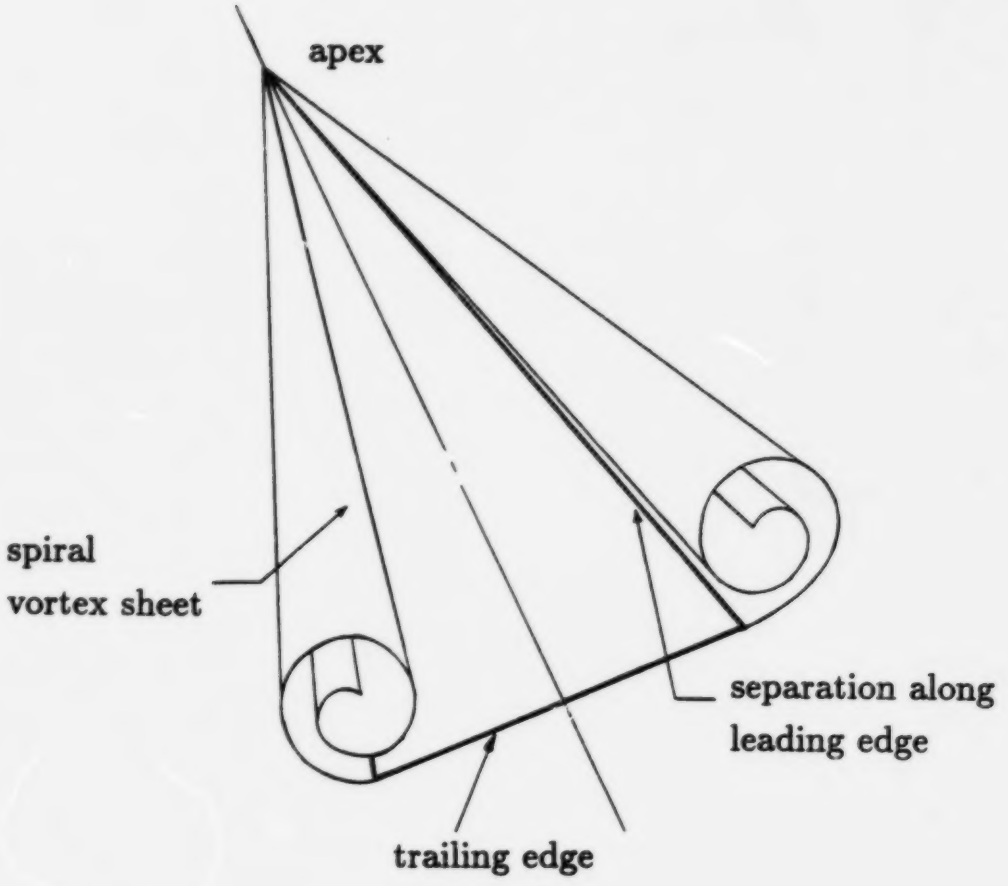

Figure 1.1: Illustration of vortex flow over a delta wing (Bird, Ref. 1).

Regime	Angles of Attack	Flow Characteristics	Delta Wings Forces
I	low	Attached flow	Linear
II	moderate	Stable and symmetric vortical flow	Nonlinear
III	high	Vortex asymmetry and/or vortex breakdown	Large changes in forces and moments
IV	extreme (up to 90°)	Unsteady wake, periodic vortex shedding	Unpredictable

Table 1.1: Flow regimes as a function of angle of attack.

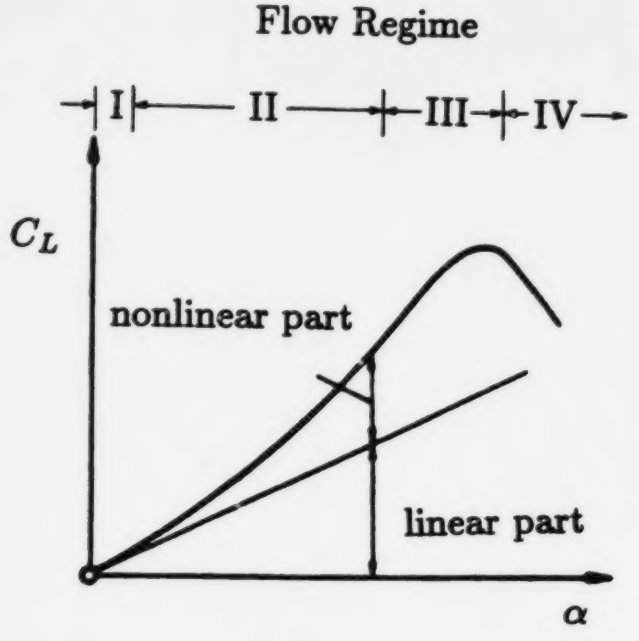

Figure 1.2: Schematic representation of the lift characteristics of a delta wing (Hummel, Ref. 2).

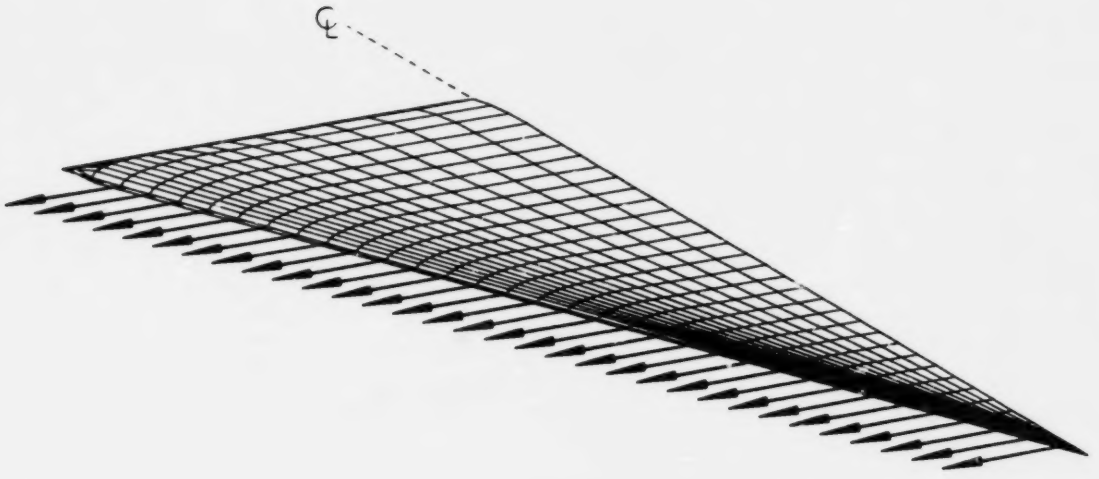

Figure 1.3: Schematic view of a delta wing with spanwise leading edge blowing.

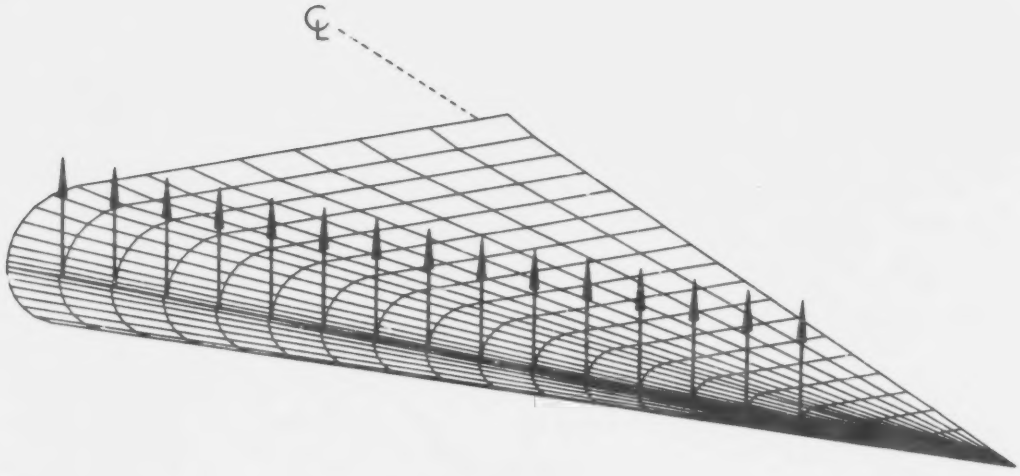

Figure 1.4: Schematic view of a conical delta wing with tangential leading edge blowing.

Chapter 2

Governing Equations and Numerical Method

2.1 Governing Equations and Approximations

The three-dimensional Navier-Stokes equations are used in this problem to describe the physical phenomena of the flow. The equations are solved with the finite-difference algorithm developed by Fujii and Obayashi [29, 30, 31]. To solve the Navier-Stokes equations through a finite-difference or a finite-volume approach, the equations are generally put into nondimensional, conservation-law form and the computation is carried out in a generalized coordinate system, using the thin-layer approximations for high Reynolds number flows. The governing equations and the numerical algorithm will be discussed briefly. More detailed information is found in references [29, 30, 31].

2.1.1 The Navier-Stokes Equations

Under the assumptions of no body force and no external heat addition, the Navier-Stokes equations in nondimensional Cartesian coordinates can be written as (see Ref. [32])

$$\frac{\partial Q}{\partial t}+\frac{\partial E}{\partial x}+\frac{\partial F}{\partial y}+\frac{\partial G}{\partial z}=\frac{\partial E_v}{\partial x}+\frac{\partial F_v}{\partial y}+\frac{\partial G_v}{\partial z} \tag{2.1}$$

where the vector of conserved quantities Q is

$$Q=\begin{bmatrix}\rho\\ \rho u\\ \rho v\\ \rho w\\ e\end{bmatrix} \tag{2.2}$$

the Euler flux vectors E, F, G are defined as

$$E=\begin{bmatrix}\rho u\\ \rho u^2+p\\ \rho uv\\ \rho uw\\ u\,(e+p)\end{bmatrix},\quad F=\begin{bmatrix}\rho v\\ \rho uv\\ \rho v^2+p\\ \rho vw\\ v\,(e+p)\end{bmatrix},\quad G=\begin{bmatrix}\rho w\\ \rho uw\\ \rho vw\\ \rho w^2+p\\ w\,(e+p)\end{bmatrix} \tag{2.3}$$

and the viscous flux vectors E_v, F_v, G_v are given by

$$E_v=Re^{-1}\begin{bmatrix}0\\ \tau_{xx}\\ \tau_{yx}\\ \tau_{zx}\\ \beta_x\end{bmatrix},\quad F_v=Re^{-1}\begin{bmatrix}0\\ \tau_{xy}\\ \tau_{yy}\\ \tau_{zy}\\ \beta_y\end{bmatrix},\quad G_v=Re^{-1}\begin{bmatrix}0\\ \tau_{xz}\\ \tau_{yz}\\ \tau_{zz}\\ \beta_z\end{bmatrix} \tag{2.4}$$

with

$$\begin{aligned}
\tau_{xx} &= \lambda(u_x + v_y + w_z) + 2\mu u_x \\
\tau_{yy} &= \lambda(u_x + v_y + w_z) + 2\mu v_y \\
\tau_{zz} &= \lambda(u_x + v_y + w_z) + 2\mu w_z \\
\tau_{xy} &= \tau_{yx} = \mu(u_y + v_x) \\
\tau_{xz} &= \tau_{zx} = \mu(u_z + w_x) \\
\tau_{yz} &= \tau_{zy} = \mu(v_z + w_y) \\
\beta_x &= \gamma\kappa Pr^{-1}\partial_x e_i + u\tau_{xx} + v\tau_{xy} + w\tau_{xz} \\
\beta_y &= \gamma\kappa Pr^{-1}\partial_y e_i + u\tau_{yx} + v\tau_{yy} + w\tau_{yz} \\
\beta_z &= \gamma\kappa Pr^{-1}\partial_z e_i + u\tau_{zx} + v\tau_{zy} + w\tau_{zz} \\
e_i &= e\rho^{-1} - 0.5\left(u^2 + v^2 + w^2\right)
\end{aligned} \tag{2.5}$$

The density is nondimensionalized by the free stream density ρ_∞, the Cartesian velocity components u, v and w are normalized by the free stream speed of sound a_∞, and the total energy per unit volume e, is scaled by $\rho_\infty a_\infty^2$. Pressure is related to the conservative flow variables, Q, through the equation of state for a perfect gas

$$p = (\gamma - 1)\left[e - \frac{\rho}{2}\left(u^2 + v^2 + w^2\right)\right] \tag{2.6}$$

where γ is the ratio of specific heats. A Newtonian fluid is considered, with the coefficient of bulk viscosity λ obtained from the Stokes' hypothesis, $\lambda = -\frac{2}{3}\mu$. The dynamic viscosity μ is nondimensionalized by μ_∞, κ is the coefficient of thermal conductivity, Re is the Reynolds number and Pr is the Prandtl number.

2.1.2 Coordinate Transformation

In the numerical computation, the governing equations are usually transformed to a general body-conforming curvilinear coordinate system. This makes the formulation of the code general and independent of body geometry, while increasing numerical accuracy (for the approximation that will be introduced in section 2.1.3) and facilitating the handling of boundary conditions. This is achieved by the following transformation :

$$\begin{aligned} \tau &= t \\ \xi &= \xi(x,y,z,t) \\ \eta &= \eta(x,y,z,t) \\ \zeta &= \zeta(x,y,z,t) \end{aligned} \tag{2.7}$$

Thus, the governing equations are transformed from the physical domain (x,y,z) to the computational domain (ξ,η,ζ). Expanding Eq. (2.7) via the chain rule yields,

$$\begin{bmatrix} \frac{\partial}{\partial t} \\ \frac{\partial}{\partial x} \\ \frac{\partial}{\partial y} \\ \frac{\partial}{\partial z} \end{bmatrix} = \begin{bmatrix} 1 & \xi_t & \eta_t & \zeta_t \\ 0 & \xi_x & \eta_x & \zeta_x \\ 0 & \xi_y & \eta_y & \zeta_y \\ 0 & \xi_z & \eta_z & \zeta_z \end{bmatrix} \begin{bmatrix} \frac{\partial}{\partial \tau} \\ \frac{\partial}{\partial \xi} \\ \frac{\partial}{\partial \eta} \\ \frac{\partial}{\partial \zeta} \end{bmatrix} \tag{2.8}$$

or conversely,

$$\begin{bmatrix} \frac{\partial}{\partial \tau} \\ \frac{\partial}{\partial \xi} \\ \frac{\partial}{\partial \eta} \\ \frac{\partial}{\partial \zeta} \end{bmatrix} = \begin{bmatrix} 1 & x_\tau & y_\tau & z_\tau \\ 0 & x_\xi & y_\xi & z_\xi \\ 0 & x_\eta & y_\eta & z_\eta \\ 0 & x_\zeta & y_\zeta & z_\zeta \end{bmatrix} \begin{bmatrix} \frac{\partial}{\partial t} \\ \frac{\partial}{\partial x} \\ \frac{\partial}{\partial y} \\ \frac{\partial}{\partial z} \end{bmatrix} \tag{2.9}$$

The transformation Jacobian is given by

$$J = |\partial(\xi, \eta, \zeta)/\partial(x, y, z)|$$

Using the transformation in Eq. (2.9) and dividing by the transformation Jacobian, the Navier-Stokes equations can be written in strong conservation-law form [33] in a generalized coordinate system (ξ, η, ζ) as follows

$$\frac{\partial \hat{Q}}{\partial \tau} + \frac{\partial\left(\hat{E} - \hat{E}_v\right)}{\partial \xi} + \frac{\partial\left(\hat{F} - \hat{F}_v\right)}{\partial \eta} + \frac{\partial\left(\hat{G} - \hat{G}_v\right)}{\partial \zeta} = 0 \tag{2.10}$$

where

$$\hat{Q} = J^{-1}\begin{bmatrix} \rho \\ \rho u \\ \rho v \\ \rho w \\ e \end{bmatrix}, \quad \hat{E} = J^{-1}\begin{bmatrix} \rho U \\ \rho u U + \xi_x p \\ \rho v U + \xi_y p \\ \rho w U + \xi_z p \\ U(e+p) - \xi_t p \end{bmatrix} \tag{2.11}$$

$$\hat{F} = J^{-1}\begin{bmatrix} \rho V \\ \rho u V + \eta_x p \\ \rho v V + \eta_y p \\ \rho w V + \eta_z p \\ V(e+p) - \eta_t p \end{bmatrix}, \hat{G} = J^{-1}\begin{bmatrix} \rho W \\ \rho u W + \zeta_x p \\ \rho v W + \zeta_y p \\ \rho w W + \zeta_z p \\ W(e+p) - \zeta_t p \end{bmatrix} \tag{2.12}$$

The contravariant velocity components U, V, W are defined as

$$\begin{aligned} U &= \xi_t + \xi_x u + \xi_y v + \xi_z w \\ V &= \eta_t + \eta_x u + \eta_y v + \eta_z w \\ W &= \zeta_t + \zeta_x u + \zeta_y v + \zeta_z w \end{aligned} \tag{2.13}$$

The viscous flux vectors are given by

$$\hat{E}_v = J^{-1}Re^{-1}\begin{bmatrix} 0 \\ \xi_x\tau_{xx} + \xi_y\tau_{xy} + \xi_z\tau_{xz} \\ \xi_x\tau_{yx} + \xi_y\tau_{yy} + \xi_z\tau_{yz} \\ \xi_x\tau_{zx} + \xi_y\tau_{zy} + \xi_z\tau_{zz} \\ \xi_x\beta_x + \xi_y\beta_y + \xi_z\beta_z \end{bmatrix} \tag{2.14}$$

$$\hat{F}_v = J^{-1}Re^{-1}\begin{bmatrix} 0 \\ \eta_x\tau_{xx} + \eta_y\tau_{xy} + \eta_z\tau_{xz} \\ \eta_x\tau_{yx} + \eta_y\tau_{yy} + \eta_z\tau_{yz} \\ \eta_x\tau_{zx} + \eta_y\tau_{zy} + \eta_z\tau_{zz} \\ \eta_x\beta_x + \eta_y\beta_y + \eta_z\beta_z \end{bmatrix} \tag{2.15}$$

$$\hat{G}_v = J^{-1}Re^{-1}\begin{bmatrix} 0 \\ \zeta_x\tau_{xx} + \zeta_y\tau_{xy} + \zeta_z\tau_{xz} \\ \zeta_x\tau_{yx} + \zeta_y\tau_{yy} + \zeta_z\tau_{yz} \\ \zeta_x\tau_{zx} + \zeta_y\tau_{zy} + \zeta_z\tau_{zz} \\ \zeta_x\beta_x + \zeta_y\beta_y + \zeta_z\beta_z \end{bmatrix} \tag{2.16}$$

In the viscous terms, the Cartesian derivatives are transformed to the generalized coordinates using the chain rule, i.e.

$$u_x = \xi_x u_\xi + \eta_x u_\eta + \zeta_x u_\zeta \tag{2.17}$$

Use of the inversion relationship between Eqs. (2.8) and (2.9) leads to the metric

identities as follows

$$\begin{aligned}
\xi_x &= J(y_\eta z_\zeta - y_\zeta z_\eta), & \zeta_x &= J(y_\xi z_\eta - y_\eta z_\xi) \\
\xi_y &= J(x_\zeta z_\eta - x_\eta z_\zeta), & \zeta_y &= J(x_\eta z_\xi - x_\xi z_\eta) \\
\xi_z &= J(x_\eta y_\zeta - x_\zeta y_\eta), & \zeta_z &= J(x_\xi y_\eta - x_\eta y_\xi) \\
\eta_x &= J(y_\zeta z_\xi - y_\xi z_\zeta), & \xi_t &= -x_\tau \xi_x - y_\tau \xi_y - z_\tau \xi_z \\
\eta_y &= J(x_\xi z_\zeta - x_\zeta z_\xi), & \eta_t &= -x_\tau \eta_x - y_\tau \eta_y - z_\tau \eta_z \\
\eta_z &= J(x_\zeta y_\xi - x_\xi y_\zeta), & \zeta_t &= -x_\tau \zeta_x - y_\tau \zeta_y - z_\tau \zeta_z
\end{aligned} \tag{2.18}$$

The inverse of the transformation Jacobian is

$$\begin{aligned}
J^{-1} &= det \begin{bmatrix} x_\xi & x_\eta & x_\zeta \\ y_\xi & y_\eta & y_\zeta \\ z_\xi & z_\eta & z_\zeta \end{bmatrix} \\
&= x_\xi y_\eta z_\zeta + x_\zeta y_\xi z_\eta + x_\eta y_\zeta z_\xi - x_\xi y_\zeta z_\eta - x_\eta y_\xi z_\zeta - x_\zeta y_\eta z_\xi
\end{aligned} \tag{2.19}$$

2.1.3 Thin-Layer Approximation

For high Reynolds number flows, the viscous effects are confined to thin vorticity layers on the walls and in the field. Resolution of the normal component of velocity gradients, and hence of boundary layers, demand high grid point density in the normal (ζ) direction near wall surfaces. Due to memory and time constraints this makes it impossible to have enough grid density in the streamwise (ξ) and circumferential (η) directions to resolve the corresponding derivative components in the

viscous terms. From this point of view it is appropriate to use the thin-layer form of the Navier-Stokes equations.

In the thin layer approach only the ζ-component (normal to the wall) derivatives in the viscous terms are retained. The thin-layer approximation can be summarized as follows,

$$\frac{\partial \hat{E}_v}{\partial \xi} = 0 \quad , \quad \frac{\partial \hat{F}_v}{\partial \eta} = 0 \tag{2.20}$$

and the Cartesian derivatives for viscous terms are approximated by

$$\begin{bmatrix} \frac{\partial}{\partial x} \\ \frac{\partial}{\partial y} \\ \frac{\partial}{\partial z} \end{bmatrix} = \begin{bmatrix} \xi_x & \eta_x & \zeta_x \\ \xi_y & \eta_y & \zeta_y \\ \xi_z & \eta_z & \zeta_z \end{bmatrix} \begin{bmatrix} 0 \\ 0 \\ \frac{\partial}{\partial \zeta} \end{bmatrix} \tag{2.21}$$

where $\frac{\partial}{\partial \xi}$ and $\frac{\partial}{\partial \eta}$ have been set to zero.

The full Navier-Stokes equations (2.10) then simplify to

$$\frac{\partial \hat{Q}}{\partial \tau} + \frac{\partial \hat{E}}{\partial \xi} + \frac{\partial \hat{F}}{\partial \eta} + \frac{\partial \hat{G}}{\partial \zeta} = Re^{-1} \frac{\partial \hat{S}}{\partial \zeta} \tag{2.22}$$

where

$$\hat{S} = J^{-1} \begin{bmatrix} 0 \\ \mu m_1 u_\zeta + (\mu/3)\, m_2 \zeta_x \\ \mu m_1 v_\zeta + (\mu/3)\, m_2 \zeta_y \\ \mu m_1 w_\zeta + (\mu/3)\, m_2 \zeta_z \\ \mu m_1 m_3 + (\mu/3)\, m_2 \left(\eta_x u + \eta_y v + \eta_z w\right) \end{bmatrix} \tag{2.23}$$

with

$$\begin{aligned} m_1 &= \zeta_x^2 + \zeta_y^2 + \zeta_z^2 \\ m_2 &= \zeta_x u_\zeta + \zeta_y v_\zeta + \zeta_z w_\zeta \\ m_3 &= \frac{1}{2}\left(u^2 + v^2 + w^2\right)_\zeta + \kappa Pr^{-1}(\gamma - 1)^{-1}\left(a^2\right)_\zeta \end{aligned} \tag{2.24}$$

Eq. (2.22) represents the thin-layer Navier-Stokes equations in a generalized coordinate system.

2.2 Numerical Algorithm

The numerical method used in this computation is the LU-ADI factorization algorithm proposed by Fujii and Obayashi [29]. This is an implicit, noniterative scheme which is first-order accurate in time and fourth-order accurate in space. The basic structure of this method is based upon the Beam-Warming algorithm [34] and incorporates the concepts of a flux vector splitting technique [35] and diagonally dominant factorization[36, 37] as described in the following sections.

2.2.1 Beam and Warming Algorithm

The Beam and Warming [34] (or Briley and McDonald [38]) implicit approximate factorization algorithm is commonly used in Computational Fluid Dynamics. Basically, this scheme can be either first- or second-order accurate in time, second- or fourth-order in space and is noniterative. At each time step, the equations are factored spatially which reduces the solution process to three one-dimensional

problems. The spatial derivatives are approximated by three-point, second-order central differences, which produces block tridiagonal systems for each spatial direction. Although the linear stability analysis in reference [34] shows the schemes to be unconditionally stable in two-dimensions, stability restrictions are encountered in practice due to the nonlinearity of the equations. However, the Beam-Warming algorithm is unconditionally unstable in three dimensions, the numerical stability is achieved by adding artificial dissipation terms to the equations.

The Beam-Warming factorization applied to (2.10) can be written as

$$\begin{aligned}
&\left(I + h\delta_\xi \hat{A}^n - D_i|_\xi\right)\left(I + h\delta_\eta \hat{B}^n - D_i|_\eta\right) \times \\
&\left(I + h\delta_\zeta \hat{C}^n - hRe^{-1}\delta_\zeta J^{-1}\hat{M}^n J + D_i|_\zeta\right)\Delta\hat{Q}^n \;=\; \hat{R}^n \\
&\quad = -h\left(\delta_\xi \hat{E}^n + \delta_\eta \hat{F}^n + \delta_\zeta \hat{G}^n - Re^{-1}\delta_\zeta \hat{S}^n\right) \\
&\qquad\qquad -\left(D_e|_\xi + D_e|_\eta + D_e|_\zeta\right)\hat{Q}^n
\end{aligned} \tag{2.25}$$

where $\Delta\hat{Q}^n = \hat{Q}^{n+1} - \hat{Q}^n$ and superscript n denotes the n^{th} time step. This method is in the so-called "delta form", which is widely used for solving steady-state problems since the final solutions do not vary with the left-hand-side operators once steady state is reached $\left(i.e.\ \Delta\hat{Q}^n = 0\right)$. In Eq. (2.25), I is the identity matrix and h is the time step, δ is a central finite-difference operator, Δ and ∇ are forward and backward difference operators, respectively. As an example illustrating these operators, consider the ξ-direction

$$\begin{aligned}
\delta_\xi \hat{Q}^n &= \left[\hat{Q}^n(\xi + \Delta\xi, \eta, \zeta) - \hat{Q}^n(\xi - \Delta\xi, \eta, \zeta)\right]/2\Delta\xi \\
\Delta_\xi \hat{Q}^n &= \left[\hat{Q}^n(\xi + \Delta\xi, \eta, \zeta) - \hat{Q}^n(\xi, \eta, \zeta)\right]/\Delta\xi
\end{aligned} \tag{2.26}$$

$$\nabla_\xi \hat{Q}^n = \left[\hat{Q}^n(\xi,\eta,\zeta) - \hat{Q}^n(\xi-\Delta\xi,\eta,\zeta)\right]/\Delta\xi$$

The flux Jacobian matrices $\hat{A}^n$, $\hat{B}^n$ and $\hat{C}^n$ are obtained from a local linearization by taking a Taylor series expansion about $\hat{Q}^n$,

$$\begin{aligned}
\hat{E}^{n+1} &= \hat{E}^n + \hat{A}^n\left(\hat{Q}^{n+1} - \hat{Q}^n\right) + \mathcal{O}\left(h^2\right) \\
\hat{F}^{n+1} &= \hat{F}^n + \hat{B}^n\left(\hat{Q}^{n+1} - \hat{Q}^n\right) + \mathcal{O}\left(h^2\right) \\
\hat{G}^{n+1} &= \hat{G}^n + \hat{C}^n\left(\hat{Q}^{n+1} - \hat{Q}^n\right) + \mathcal{O}\left(h^2\right)
\end{aligned} \tag{2.27}$$

where the flux Jacobian matrices are given by

$$\hat{A} = \frac{\partial \hat{E}}{\partial \hat{Q}} \ , \quad \hat{B} = \frac{\partial \hat{F}}{\partial \hat{Q}} \ , \quad \hat{C} = \frac{\partial \hat{G}}{\partial \hat{Q}} \tag{2.28}$$

Similarly, the viscous coefficient matrix $\hat{M}$ is obtained from the linearization of the viscous vector $\hat{S}$. Expressions for the flux Jacobian matrices, $\hat{A}$, $\hat{B}$, $\hat{C}$ as well as the viscous coefficient matrix $\hat{M}$ are given in Appendix A.

The D_i and D_e terms are implicit and explicit artificial dissipation terms which should be added to the left-hand-side and the right-hand-side, respectively, to maintain numerical stability. The expressions and origins of these numerical dissipation terms will be described later.

2.2.2 The LU-ADI Algorithm

The procedure for solving the block tridiagonal systems associated with the Beam-Warming algorithm [34] requires a large computational time. In order to make the

solution scheme more cost effective, the left hand side of Beam-Warming scheme is modified by introducing the LU-ADI algorithm described in reference[29]. This algorithm incorporates a flux-vector splitting technique [35] and a diagonally dominant factorization [36, 37] such that the Alternate Direction Implicit (ADI) operator is decomposed into a product of lower and upper bidiagonal matrices, In this way, only scalar inversions are required.

The flux Jacobian matrices $\hat{A}$, $\hat{B}$ and $\hat{C}$ given in Eq. (2.28) have real eigenvalues and a complete set of eigenvectors and can then be diagonalized through a similarity transformation,

$$\hat{\Lambda}_\xi = T_\xi^{-1}\,\hat{A}\,T_\xi\,, \quad \hat{\Lambda}_\eta = T_\eta^{-1}\,\hat{B}\,T_\eta\,, \quad \hat{\Lambda}_\zeta = T_\zeta^{-1}\,\hat{C}\,T_\zeta \tag{2.29}$$

The diagonal matrices $\hat{\Lambda}_\xi$, $\hat{\Lambda}_\eta$, $\hat{\Lambda}_\zeta$ contain the eigenvalues in each spatial direction

$$\begin{aligned}
\hat{\Lambda}_\xi &= Diag\left[U,\, U,\, U,\, U + a\sqrt{\xi_x^2+\xi_y^2+\xi_z^2},\, U - a\sqrt{\xi_x^2+\xi_y^2+\xi_z^2}\,\right] \\
\hat{\Lambda}_\eta &= Diag\left[V,\, V,\, V,\, V + a\sqrt{\eta_x^2+\eta_y^2+\eta_z^2},\, V - a\sqrt{\eta_x^2+\eta_y^2+\eta_z^2}\,\right] \\
\hat{\Lambda}_\zeta &= Diag\left[W,\, W,\, W,\, W + a\sqrt{\zeta_x^2+\zeta_y^2+\zeta_z^2},\, W - a\sqrt{\zeta_x^2+\zeta_y^2+\zeta_z^2}\,\right]
\end{aligned} \tag{2.30}$$

where U, V and W are the contravariant velocity components and a is the speed of sound. The similarity transformation matrices T_ξ, T_η, T_ζ and their inverse matrices T_ξ^{-1}, T_η^{-1}, T_ζ^{-1} are given in appendix B.

For the ξ-direction, the Beam-Warming ADI operator ($\hat{\mathcal{L}}$) can be rewritten in diagonal form [36, 37] as follows

$$\begin{aligned}\hat{\mathcal{L}}_\xi &= I + h\delta_\xi \hat{A} + J^{-1}\epsilon_i \delta_\xi^2 J \\ &= T_\xi T_\xi^{-1} + h\delta_\xi \left(T_\xi \hat{\Lambda}_\xi T_\xi^{-1}\right) + T_\xi J^{-1}\epsilon_i \delta_\xi^2 J T_\xi^{-1} \\ &\approx T_\xi \left[I + h\delta_\xi \hat{\Lambda}_\xi + J^{-1}\epsilon_i \delta_\xi^2 J\right] T_\xi^{-1} \end{aligned} \tag{2.31}$$

where an approximation is introduced by factoring the eigenvector matrix T_ξ outside of the spatial derivative operator δ_ξ. Since the eigenvector matrix T_ξ is a function of ξ, this modification reduces the time accuracy to at most first-order in time [37]. It should be pointed out that the explicit side of the diagonal algorithm which contains the steady-state finite difference equations remains the same. If the diagonal algorithm converges, the steady-state solution will be identical to that obtained from the original algorithm. Thus, this modification does not downgrade the final steady state solution.

The central differencing can be decomposed into two-sided differencing by using the flux-vector splitting technique [35]. The right hand side of Eq. (2.31) becomes

$$\hat{\mathcal{L}}_\xi = T_\xi \left[I + \nabla_\xi \hat{\Lambda}_\xi^+ + \Delta_\xi \hat{\Lambda}_\xi^-\right] T_\xi^{-1} \tag{2.32}$$

with

$$\hat{\Lambda}_\xi^\pm = \frac{h}{2}\left(\hat{\Lambda}_\xi \pm \left|\hat{\Lambda}_\xi\right|\right) \pm \underline{J}^{-1}\epsilon_i J \tag{2.33}$$

where $\hat{\Lambda}_\xi^+$ contains the positive eigenvalues and $\hat{\Lambda}_\xi^-$ contains the negative eigenvalues, $\underline{J}^{-1}$ is taken to be the transformation Jacobian at the central point, and ϵ_i is the

magnitude of the implicit artificial dissipation term, to be discussed in the next section.

Using first-order upwind differencing, Eq. (2.32) can be written as

$$\hat{\mathcal{L}}_\xi = T_\xi \left[L_\xi + D_\xi + U_\xi \right] T_\xi^{-1} \tag{2.34}$$

where

$$\begin{aligned} L_\xi &= -\hat{\Lambda}^+_{\xi\ j-1} \\ D_\xi &= I + \left(\hat{\Lambda}^+_{\xi\ j} - \hat{\Lambda}^-_{\xi\ j} \right) \\ U_\xi &= \hat{\Lambda}^-_{\xi\ j+1} \end{aligned} \tag{2.35}$$

where the subscript j, is the grid point index in the ξ-direction. Eq. (2.34) can be approximated as follows

$$L_\xi + D_\xi + U_\xi = \left(L_\xi + D_\xi \right) D_\xi^{-1} \left(D_\xi + U_\xi \right) + \mathcal{O}\left(h^2 \right) \tag{2.36}$$

where higher order terms are dropped since $D_\xi = \mathcal{O}(1)$ and $L_\xi, U_\xi = \mathcal{O}(h)$. Substituting Eq. (2.36) into Eq. (2.34), the LU factorization for the ADI operator in the ξ direction becomes

$$I + h\delta_\xi \hat{A} + J^{-1} \epsilon \delta_\xi^2 J = T_\xi \left(L_\xi + D_\xi \right) D_\xi^{-1} \left(D_\xi + U_\xi \right) T_\xi^{-1} \tag{2.37}$$

The block tridiagonal system has been decomposed into the product of the lower and upper scalar bidiagonal systems $\left[L_\xi + D_\xi \right]$ and $\left[D_\xi^{-1} \left(D_\xi + U_\xi \right) \right]$.

In order to take the thin-layer viscous terms into account while using the diagonal dominant factorization, the split flux Jacobian matrices $\hat{C}^{\pm}$ are modified as

$$\hat{C}^{\pm} = T_\zeta \left(\hat{\Lambda}_\zeta^{\pm} \pm \nu I \right) T_\zeta^{-1} \tag{2.38}$$

where

$$\nu = 2\mu \sqrt{\zeta_x^2 + \zeta_y^2 + \zeta_z^2} \; / \; (Re \, \rho \, \Delta\zeta)$$

By using a similar procedure for the other operators, this method can be summarized as follows :

$$\begin{aligned} & T_\xi \left(L_\xi + D_\xi \right) D_\xi^{-1} \left(D_\xi + U_\xi \right) \left(T_\xi^{-1} T_\eta \right) \left(L_\eta + D_\eta \right) D_\eta^{-1} \left(D_\eta + U_\eta \right) \\ & \left(T_\eta^{-1} T_\zeta \right) \left(L_\zeta + D_\zeta \right) D_\zeta^{-1} \left(D_\zeta + U_\zeta \right) T_\zeta^{-1} \Delta \hat{Q}^n = \hat{R}^n \end{aligned} \tag{2.39}$$

The expressions for $(T_\xi^{-1} T_\eta)$, $(T_\eta^{-1} T_\zeta)$ used in Eq. (2.39) and their inverse matrices $(T_\eta^{-1} T_\xi)$, $(T_\zeta^{-1} T_\eta)$ can be written in a simpler form, given in Appendix B. In the solution process, an inversion in one direction consists of one scalar forward sweep and one scalar backward sweep.

2.2.3 Numerical Dissipation Model

The fourth-order dissipation model has been widely used with central differences in Navier-Stokes computations. This constant dissipation model produces an undesirable oscillatory solution near discontinuities such as shock waves. On the other hand, second-order dissipation produced by proper upwinding works much better

than the fourth-order dissipation model in regions near discontinuities. Such dissipation, however, is not desirable in the rest of the flow field since it reduces the spatial accuracy to first-order.

The numerical dissipation model used here is a non-linear, second- and fourth-order mixed type whose magnitude is controlled by a local flux limiter function based on a simplified version of the Total Variation and Diminishing (TVD) [39] method. In doing so, numerical stability is maintained while the flow physics is captured without an excessive amount of artificial dissipation, as compared to the global constant numerical dissipation model.

For the ξ - direction, the explicit numerical dissipation terms can be expressed as

$$D_e|_\xi \hat{Q}^n = \nabla_\xi \left\{ \phi \left(\frac{\epsilon_e}{J} \right)_{j+\frac{1}{2}} \Delta_\xi \hat{Q}_j + (\phi - 1) \nabla_\xi \Delta_\xi \left[\left(\frac{\epsilon_e}{J} \right)_{j+\frac{1}{2}} \Delta_\xi \hat{Q}_j \right] \right\} \qquad (2.40)$$

where

$$\begin{aligned} \phi &= \text{flux limiter function} \\ \epsilon_e &= K_\epsilon \, h \, \sigma_k \\ K_\epsilon &= \text{an input constant} \\ \sigma_k &= \text{spectral radius of } \hat{\Lambda}_k \\ &= |uk_x + vk_y + wk_z| + a\sqrt{k_x^2 + k_y^2 + k_z^2}\,; \; k = \xi,\, \eta \text{ or } \zeta \end{aligned}$$

The flux limiter function ϕ has values ranging from 0 to 1 depending on the smoothness of the solution. For a relatively smooth solution, for which the signs of forward

and backward differencing at a given point of the solution are the same, and their magnitudes are similar, ϕ takes the value of zero so that only the fourth-order dissipation terms are used. On the other hand, when the flux limiter function detects an oscillation or a large gradient, ϕ will be set close to 1 so that the second-order dissipation terms are dominant.

In order to reduce the influence of the numerical dissipation in the direction normal to wall inside of boundary layer, the magnitude of numerical dissipation is scaled by the ratio of the local contravariant velocity component to the free stream velocity magnitude

$$\tilde{\epsilon}_e|_\zeta = \epsilon_e|_\zeta \times \frac{\sqrt{\frac{(\vec{V}\cdot\nabla\xi)^2}{|\nabla\xi|^2} + \frac{(\vec{V}\cdot\nabla\eta)^2}{|\nabla\eta|^2}}}{|V_\infty|} \tag{2.41}$$

where, for example, $\nabla\xi = (\xi_x, \xi_y, \xi_z)$. The details of the current flux limiter function are given in reference [40].

In the implicit operators, it may not be necessary to include artificial dissipation terms since the LU-ADI implicit operator is based on upwinding. Currently, implicit numerical dissipation terms are included as shown in Eq. (2.33), whose magnitudes are obtained in the same way as that for the one in Eq. (2.40).

2.2.4 Turbulence Model

The Baldwin and Lomax Model

The concept of an effective viscosity coefficient is used to model the turbulent mixing

by introducing the so–called eddy viscosity, μ_t. The eddy viscosity is obtained from the two-layer algebraic model proposed by Baldwin and Lomax [41].

In this model, the eddy viscosity is evaluated in inner and outer layers,

$$\mu_t = \begin{cases} (\mu_t)_{\text{inner}} & , \zeta \leq \zeta_{\text{crossover}} \\ (\mu_t)_{\text{outer}} & , \zeta > \zeta_{\text{crossover}} \end{cases} \tag{2.42}$$

where ζ is the normal distance from the wall and $\zeta_{\text{crossover}}$ is the smallest value of y at which the inner and outer values of μ_t are equal.

The eddy viscosity coefficient in the inner layer is based on the Prandtl-Van Driest expression (i.e. reference [42]),

$$(\mu_t)_{\text{inner}} = \rho l^2 |\omega| \tag{2.43}$$

where the length scale l is obtained from

$$l = k\zeta \left[1 - \exp\left(-\frac{\zeta^+}{A^+}\right)\right]$$

where $k = 0.4$, $\zeta^+ = \frac{(\zeta\sqrt{\rho_w \tau_w})}{\mu_w}$, $A^+ = 26$, and $|\omega|$ is the magnitude of the local vorticity vector

$$|\omega| = |\nabla \times \vec{V}| = \sqrt{(u_y - v_x)^2 + (v_z - w_y)^2 + (w_x - u_z)^2}$$

The expression for the outer layer is given by

$$(\mu_t)_{\text{outer}} = K\, C_{cp}\, F_{wake}\, F_{Kleb}(\zeta) \tag{2.44}$$

with $K = 0.0168$, $C_{cp} = 1.6$ and where F_{wake} is determined as follows

$$F_{wake} = \text{the smaller of} \begin{bmatrix} \zeta_{max} F_{max} \\ \text{or} \\ C_{wk} \zeta_{max} U_{dif}^2 / F_{max} \end{bmatrix}$$

The values of ζ_{max} and F_{max} are obtained from the function

$$F(\zeta) = \zeta |\omega| \left[1 - \exp\left(-\frac{\zeta^+}{A^+} \right) \right]$$

where $C_{wk} = 0.25$ and U_{dif} is the difference between the maximum and the minimum total velocity magnitudes in the profile along the ζ-direction. The minimum total velocity magnitude is zero at the walls and is a finite in wakes. The quantity F_{max} is the maximum value of $F(\zeta)$ in the profile along the ζ-direction, and ζ_{max} is the value of ζ at which it occurs. The function $F_{Kleb}(\zeta)$ is the Klebanoff intermittency factor given by

$$F_{Kleb}(\zeta) = \left[1 + 5.5 \left(\frac{C_{Kleb}\, \zeta}{\zeta_{max}} \right)^6 \right]^{-1}$$

with $C_{Kleb} = 0.3$.

Once the value of the eddy viscosity, μ_t, is determined, the total viscosity is defined as

$$\mu = \mu_l + \mu_t \tag{2.45}$$

where μ_l is the molecular or laminar viscosity. The coefficient of thermal conductivity can be obtained as

$$\kappa = \kappa_l + \kappa_t = \frac{C_p \mu_l}{Pr} + \frac{C_p \mu_t}{Pr_t} \tag{2.46}$$

The quantity Pr_t is the turbulent Prandtl number which is set to 0.9, and the laminar Prandtl number Pr is 0.72.

Turbulence Model for a Wall Jet

Based on the theory of Roberts [28] for turbulent curved wall jets, an algebraic eddy viscosity model, together with the effects of wall curvature, are used in the tangential leading edge blowing cases. This model uses self-similar profiles for the mean velocity and momentum balance to get the expression for eddy viscosity

$$\mu_t = \frac{K}{4\,k^2}\, b\, \rho\, u_m \left(\frac{\zeta}{b}\right)^2 \tag{2.47}$$

where $K = 0.075$, $k = 0.8814$, u_m is the maximum velocity, b is the distance to the point where $u = \frac{1}{2}u_m$ and ζ is the distance normal to wall surface. From the existing experimental results (i.e. [43, 44]) it is found

$$b = 7\,\zeta_m \tag{2.48}$$

where the subscript m denotes the location of the maximum velocity. Evaluating the constants and making use of Eq. (2.47), Eq. (2.46) can be written as

$$\mu_t = 0.0033\,\zeta_m\,\rho\,u_m \left(\frac{\zeta}{\zeta_m}\right)^2 \tag{2.49}$$

where

$$\frac{\zeta}{\zeta_m} = \left\{ \begin{array}{ll} \frac{\zeta}{\zeta_m} & ; \quad \zeta < \zeta_m \\ 1 & ; \quad \zeta \geq \zeta_m \end{array} \right\}$$

To include the effects of wall curvature, the eddy viscosity is modified as follows

$$\tilde{\mu}_t = \mu_t \left(1 - \frac{V_c}{R} \frac{1}{\frac{\partial V_c}{\partial \zeta}} \right) \tag{2.50}$$

where V_c is the cross-flow velocity magnitude and R is the radius of curvature of the wall. This model is applied from the jet exit up to the point where the wall jet separates from the surface.

Chapter 3

Spanwise Blowing

3.1 Introduction

As discussed in Chapter 1, the vortical flow field associated with flow separation from the leading edge of a delta wing plays an important role in determining the lift. It is desirable to control this vortex flow and if possible to enhance its contribution. A promising method of control is to eject a thin, high-momentum jet in the spanwise direction along the leading edge of the delta wing. This jet sheet displaces the flow outboard and rolls up in a similar manner to the rolling-up of the free vortex sheet. As a result, higher suction peaks on the wing surface are induced by the stronger leading edge vortices which produce more lift.

Since spanwise blowing increases the strength of the leading edge vortices at a given incidence (as will be shown in the later sections,) the adverse pressure gradient along the vortex core becomes more pronounced near the trailing edge. Thus, blowing reduces the angle of attack at which vortex breakdown occurs. For this reason, spanwise blowing would be primarily of interest as a lift device, or a

roll control device, at low to moderate angles of attack. Consequently, emphasis in this chapter will focus on this angle-of-attack range. The adverse effects on the vortex flow due to spanwise blowing in the presence of vortex breakdown will be illustrated briefly in section 3.4.2.

The leading edge jet is simulated by defining a permeable boundary, corresponding to the jet slot, where suitable boundary conditions are implemented. The simulations start with the no-blowing case, which will be used to illustrate the main features of delta wing aerodynamics and as a base line for comparisons with blowing cases. The blowing conditions will be chosen from cases for which experimental results [12] are available, and will also serve to validate the jet-exit boundary conditions.

3.2 Grid Generation

The three-dimensional mesh about a delta wing is generated through three steps. The first step is to generate the surface-grid that describes the geometry of the wing. This is done by distributing the grid points on a two-dimensional section at each cross-flow plane, once the chordwise stations are identified. An exponential stretching function is used to cluster the grid points near the leading edge, where the jet slot is located.

The next step is to generate a three-dimensional mesh using a two-dimensional hyperbolic grid-generation method [45, 46] for each chordwise station. This method uses the surface-grid points as a set of initial data and generates the grid by marching away from the body. An inversion of a 2-by-2 block tridiagonal system is required

since there are two unknowns (y, z) at each grid point under the constrains of orthogonality and positive cell volume. As a result of using this hyperbolic grid-generation method, the outer boundary in the streamwise direction is generally not uniform, as shown in figure 3.1. This is because the outer boundary is determined according to an initial distribution of points on the body, while the local span of a delta wing increases toward the trailing edge.

The final step is to redistribute the grid points along each of the radial curves by using a cubic spline such that the outer boundary dimensions can be controlled and the orthogonality condition close to the body be satisfied. An exponential stretching function is used to cluster the grid points along each radial curve near the wall, appropriate to the thin layer approximation. Figure 3.2 shows a close-up view of a typical cross section of a delta wing, where bilateral symmetry is imposed to reduce the computational effort.

The final grid arrangement, as shown in figure 3.3, is cylindrical and corresponds to an H-type topology in the chordwise direction and an O-type topology in the spanwise direction. The grid extends 1 root chord upstream, 1 chord downstream, 2 chords above and laterally, and 1.5 chord below, and results in a total number of $55 \times 65 \times 33 \approx 118{,}000$ grid points. The number of grid points in each direction is chosen judiciously to capture the jet effects, while maintaining the memory requirements within the 4 million 64-bit words of the Cray X-MP at Ames Research Center. Regarding the influence of the over-all dimensions of the computational domain, numerical experimentation shows that increasing the dimensions in all directions by one half of a chord length, while keeping the number of grid points constant, changes the lift coefficient by 0.5% (for AR = 1.4, $\alpha = 15°$).

The global reference frame is expressed in terms of a body-fitted curvilinear system (ξ, η, ζ) where ξ is in the chordwise direction, η is in the circumferential direction, and ζ is in the radial direction such that a right-handed coordinate system is formed.

3.3 Boundary and Jet-Exit Conditions

For a steady viscous flow, no-slip boundary conditions are imposed at the wall, where $U = V = W = 0$. The pressure on the body surface is obtained from the normal momentum equation,

$$\left[\partial_\xi \hat{E} + \partial_\eta \hat{F} + \partial_\zeta \hat{G}\right]^T \begin{bmatrix} \zeta_x \\ \zeta_y \\ \zeta_z \end{bmatrix} = 0 \tag{3.1}$$

or

$$\begin{aligned} & (\xi_x\zeta_x + \xi_y\zeta_y + \xi_z\zeta_z)\, P_\xi + (\eta_x\zeta_x + \eta_y\zeta_y + \eta_z\zeta_z)\, P_\eta + \left(\zeta_x^2 + \zeta_y^2 + \zeta_z^2\right) P_\zeta \\ = \; & -\rho U\,(\zeta_x u_\xi + \zeta_y v_\xi + \zeta_z w_\xi) - \rho V\,(\zeta_x u_\eta + \zeta_y v_\eta + \zeta_z w_\eta) \\ = \; & P_n\sqrt{\zeta_x^2 + \zeta_y^2 + \zeta_z^2} \\ = \; & 0 \end{aligned} \tag{3.2}$$

where P_n is the component of the pressure gradient normal to the body surface. Eq. (3.2) is solved at the surface using central second-order accurate differences in ξ and η, and one-sided second-order accurate differences in ζ. Once the surface pressure distribution is determined, the total energy per unit volume, e, is calculated

according to Eq. (2.6). Adiabatic or constant temperature walls are used such that the density value on the wall is extrapolated from the nearest point normal to the wall. These boundary conditions are updated explicitly at each time step.

At the upstream and circumferential outer boundaries, free stream values are specified and remain fixed. Extrapolated values are used at the downstream boundary except for e, which is calculated based on the free stream static pressure for the present subsonic calculations. Symmetry conditions are imposed on the symmetry plane.

Regarding the boundary conditions at the jet exit, it is necessary to specify two thermodynamic variables and one kinematic variable at the jet exit plane in order to obtain the $\hat{Q}$ vector. The blowing momentum coefficient (C_μ) is introduced as a nondimensional parameter that indicates the intensity of blowing,

$$C_\mu \equiv \frac{\int\int_{A_j} \rho_{jet} V_{jet} \vec{V}_{jet} \cdot \vec{e}_s \, dA_j}{q_\infty \, S_{wing}} \tag{3.3}$$

where the numerator is the total momentum of the jet, $\vec{e}_s$ is the unit vector in the spanwise direction, A_j is the projected area of the jet slot perpendicular to the spanwise direction, q_∞ is the free stream dynamic pressure and S_{wing} is the wing reference area. The jet-exit boundary conditions are summarized as follows:

(1) At the jet boundaries the local static pressure is used, and the pressure across the thin jet is assumed to vary linearly.

(2) The free stream value of density is specified at the jet exit.

(3) The jet-exit velocity distribution is prescribed for convenience as an elliptical profile whose maximum value is determined from a specified C_μ.

As mentioned in the introduction (section 1.2.1), it is desirable to maintain conical blowing conditions over most of the wing. This requires a linearly varying jet momentum flux. This conical blowing condition is approximated through a linearly varying jet-slot width and a constant maximum velocity. This distribution of blowing momentum would be exactly linear if the jet exit velocity profile were uniform. The elliptical distribution was chosen, however, for better numerical conditioning. The analytical calculation of the jet momentum is given in appendix C.

3.4 Results and Physical Interpretation

3.4.1 No Blowing

To understand the effects of leading edge blowing on the vortical flow of a delta wing, a no-blowing case at $\alpha = 10°$ is first simulated and will be used for comparison with the blowing cases and with experimental results [12]. A 70°-sweep delta wing is used in the computation with the free stream conditions of $M_\infty = 0.3$ and $Re_\infty = 1.3 \times 10^6$. Between the apex and 95% of the root chord (c_0), the delta wing geometry is generated numerically with conical symmetry; that is, with linearly increasing thickness of up to 3.5% of c_0. The remaining 5 % of the root chord is closed by an elliptical afterbody. The leading edge shape is modeled as an ellipse of 5 to 1 eccentricity ratio to simulate a leading edge of small radius.

Figure 3.4 illustrates the leading edge vortex sheet in the half-space from the symmetry plane corresponding to 10 degrees angle of attack . The boundary layer on the lower surface separates at the leading edge resulting in a free shear layer emanating from the edge. This free shear layer rolls up in a spiral fashion to form

the leading edge vortex. The particle traces shown in the figure were obtained by "releasing particles" near the wing surface (velocity is zero on the surface) close to the leading edge and tracing their trajectories through numerical integration of the velocity field. This was done by using the PLOT3D [47] interactive plotting software developed at NASA, Ames Research Center.

A conical transformation [48] is performed to better illustrate the size and location of the leading edge vortex in the cross-flow plane. The so-obtained description of a conical particle trace represents the rescaling of space curves describing particle paths of a three-dimensional conical flow [49]. Such a conical transformation can be expressed as follows

$$\underbrace{X, Y, Z}_{\text{Conical variables}} \quad \rightleftharpoons \quad \underbrace{x, y, z}_{\text{3-D variables}}$$

with

$$\begin{aligned} X &= x \\ Y &= \frac{y}{x} \\ Z &= \frac{z}{x} \end{aligned} \tag{3.4}$$

the value of X is chosen to be 1 for simplicity, since the transformation causes X to drop out. The unit vectors in the conical projection plane are

$$\begin{aligned} \vec{e}_Y &= \frac{1}{\sqrt{Y_x^2 + Y_y^2 + Y_z^2}} (Y_x, Y_y, Y_z) \\ \vec{e}_Z &= \frac{1}{\sqrt{Z_x^2 + Z_y^2 + Z_z^2}} (Z_x, Z_y, Z_z) \end{aligned} \tag{3.5}$$

and the conical velocity components are calculated according to

$$V_{\text{conical}} = \vec{V} \cdot \vec{e}_Y \tag{3.6}$$

$$W_{\text{conical}} = \vec{V} \cdot \vec{e}_Z \tag{3.7}$$

Figure 3.5 illustrates the vortex traces in the transformed conical projection plane at 50 % of the root chord ($x/c_0 = 0.5$) In this representation, size and location of the leading edge vortex can be easily identified, as opposed to the three-dimensional view (figure 3.4).

This leading edge vortex induces a suction peak at the wing surface, and contributes appreciably to the lift. To illustrate this characteristic of a delta wing, Figure 3.6 shows the pressure coefficient (C_p) distribution on the wing surface at $x/c_0 = 0.5$ for $\alpha = 10°$. A distinct vortex suction peak is clearly evident on the upper surface. The adverse pressure gradient (slope of the surface pressure curve) outboard of the primary vortex core causes a secondary separation, not shown in figure 3.5, creating a local suction peak near the leading edge. The narrow suction peak located very near the leading edge results from flow acceleration around the leading edge from the lower surface of the wing. This suction peak terminates in the vicinity of the primary separation line.

These flow properties are also inferred from the computed near-surface streamlines. For the same flow conditions, figure 3.7 illustrates a typical example of the streamline pattern on the upper surface. Aided by the schematic view of the vortical flow pattern [50] over a delta wing, as shown in figure 3.8, the following observations can be made about figure 3.7 : The flow drawn into the primary vortex core

moves sideways until the secondary separation line is reached. Beyond this line, the flow separates due to viscous effects, creating a secondary separation region. The flow reattaches at the secondary attachment line and moves further outward. This secondary attachment region ends at the primary separation line, where the flow from the lower surface separates and rolls up to form the leading edge vortex. These attachment and separation lines can be easily identified [51] as follows : the attachment line is distinguished by diverging streamlines and the separation line is characterized by converging streamlines.

3.4.2 Spanwise Blowing

The same delta wing geometry is used for the spanwise blowing calculations. The jet slot geometry is described as a tapered slot that extends approximately from 3% to 94% of the root chord, with a maximum jet width of 5.5% of the local thickness of the delta wing. Such a slot geometry is chosen to simulate conical blowing and to partially match the model used in the experiment [12]. Seven grid points at each streamwise wing-station are used to simulate the leading edge jet. The relative location of the jet on the delta wing and the blowing direction are shown in figure 1.3.

Figure 3.9 shows the particle traces emanating near the leading edge for $C_\mu = 0$ and .047 at $\alpha = 10°$, where the particles are released from the same locations under the same free stream conditions. Two observations can be made by comparing the particle traces for the no-blowing and blowing cases : blowing results in an enlargement as well as an outboard displacement of the rolled-up shear layer.

Figures 3.10 (a) - (d) illustrate the growth of the vortex dimensions as well as the rigidity of the jet as the blowing momentum coefficient is increased for $\alpha = 10°$. These figures are obtained by "releasing particles" from the jet exit in the transformed conical projection plane at $x/c_0 = 0.5$. The vortex position is shown to move outward and upward as C_μ increases. This is due to the fact that the curved jet stream, which originates at the leading edge, can sustain a pressure jump and therefore imparts rigidity to the jet-vortex sheet. Equivalently, the effective aspect ratio of the delta wing is increased due to blowing.

The effects of jet momentum on the spanwise surface pressure coefficient (C_p) distribution are shown in figure 3.11 for $\alpha = 10°$ at $x/c_0 = 0.5$. A higher vortex suction clearly results from higher blowing momentum coefficients. On the other hand, the pressure distribution close to the root chord remains virtually unchanged. As a result, the increment in lift due to blowing comes primarily from the higher nonlinear vortex lift. Figure 3.11 also shows that the high pressure region near the leading edge on the windward side extends outward as C_μ increases. Such a trend is to be expected, since the presence of the leading edge jet stream displaces the flow outboard corresponding to an effective enlargement of the wing-span.

Figure 3.12 shows the computed near-surface flow pattern on the upper surface of the delta wing for $C_\mu = 0$ and $C_\mu = 0.0705$ at $\alpha = 10°$. In the figure, only the region up to 95% of the root chord is shown, where conical conditions are simulated. It is observed that the secondary separation region is "swept" outboard due to the outward movement of the primary vortex, a fact also observed by Alexander [13]. It is to be noted that the inward motion of near-surface particle traces in the secondary separation region is enhanced as compared to that in the no blowing

case. This phenomenon is also revealed by the higher local pressure peak near the leading edge ($C_\mu = 0.0705$), as shown in figure 3.11.

A comparison of the computed results with Trebble's [12] experimental data for a 70°-sweep delta wing at $\alpha = 10°$ is shown in figure 3.13. In this figure, the increment in C_L due to blowing at a constant angle of attack is defined as

$$\Delta C_L \Big|_{\substack{\text{due to} \\ \text{blowing}}} = C_L \Big|_{\substack{\text{with} \\ \text{blowing}}} - C_L \Big|_{\substack{\text{no} \\ \text{blowing}}} \tag{3.8}$$

Agreement between the predicted and experimental results is good.

Figure 3.14 illustrates the variation of normal force coefficient with angle of attack for the no-blowing and blowing ($C_\mu = 0.05$) cases. It clearly shows that higher force is obtained by blowing in the region of low to moderate angles of attack. It also shows that the maximum normal force coefficient for the blowing case occurs at a lower angle of attack compared to that in the no-blowing case, indicating that blowing reduces the angle of attack at which vortex breakdown occurs. The earlier vortex breakdown may be attributed to two factors :

(i) Since spanwise blowing increases the strength of the leading edge vortices at a given incidence, the adverse pressure gradient along the vortex core becomes more pronounced near the trailing edge.

(ii) The angle of attack at which vortex breakdown occurs decreases as the aspect ratio increases, as illustrated in reference [52]. Since the jet effectively increases the wing span, it causes vortex breakdown at lower angles of attack.

To demonstrate the adverse effect of spanwise blowing in post-stall conditions,

Figures 3.15 and 3.16 show the reverse flow velocity contours for the no-blowing and blowing cases at $x/c_0 = .77$ for $\alpha = 40°$, where vortex breakdown has occurred. The outer contour is the interface boundary between the forward and reverse flow velocity, where the velocity magnitude is zero. The reverse flow bubble is clearly enlarged and the maximum negative-u velocity is also greater in the blowing case. This indicates that blowing enhances vortex breakdown in the post stall conditions. Therefore, spanwise leading edge blowing would be primarily of interest as a lift device, or a roll control device, at low to moderate angles of attack.

Since tangential blowing (to be discussed in Chapter 4) is primarily intended for high angles of attack, the discussion of the structure of the leading edge vortices and vortex breakdown at high angles of attack will be delayed until Chapter 4.

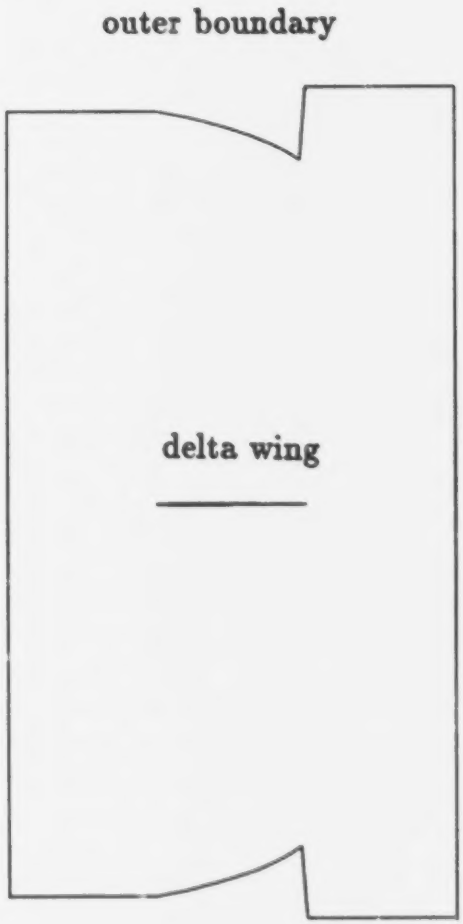

Figure 3.1: Outer boundary (side view) generated by a two-dimensional hyperbolic grid generation method about a delta wing.

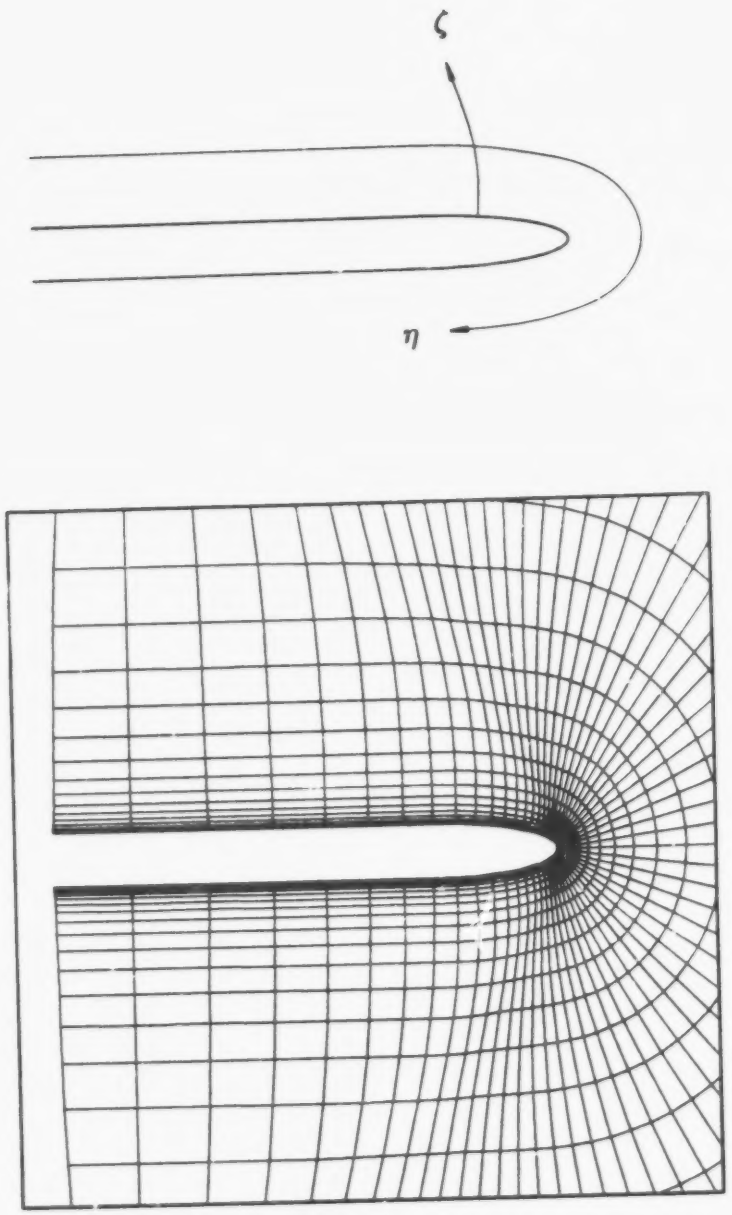

Figure 3.2: Close-up view of a typical chordwise station of a delta wing.

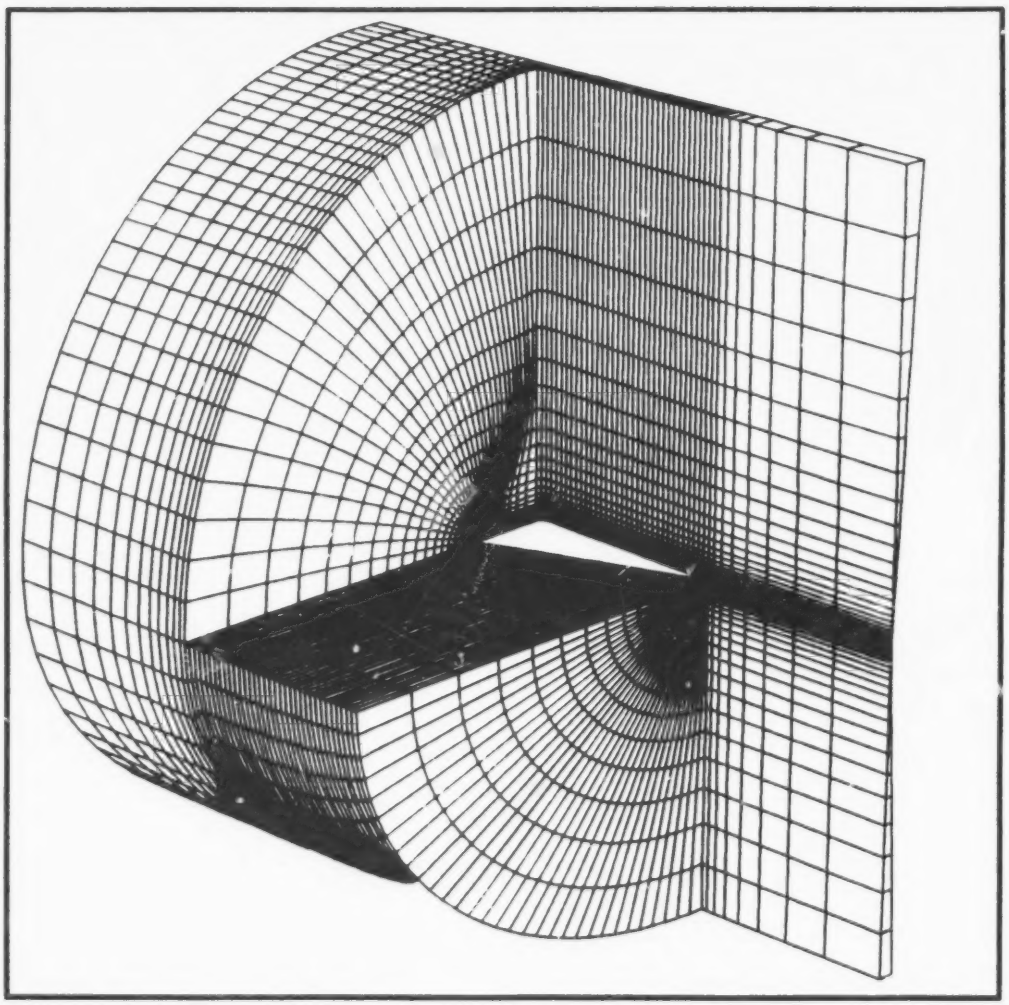

Figure 3.3: Partial view of the computational domain.

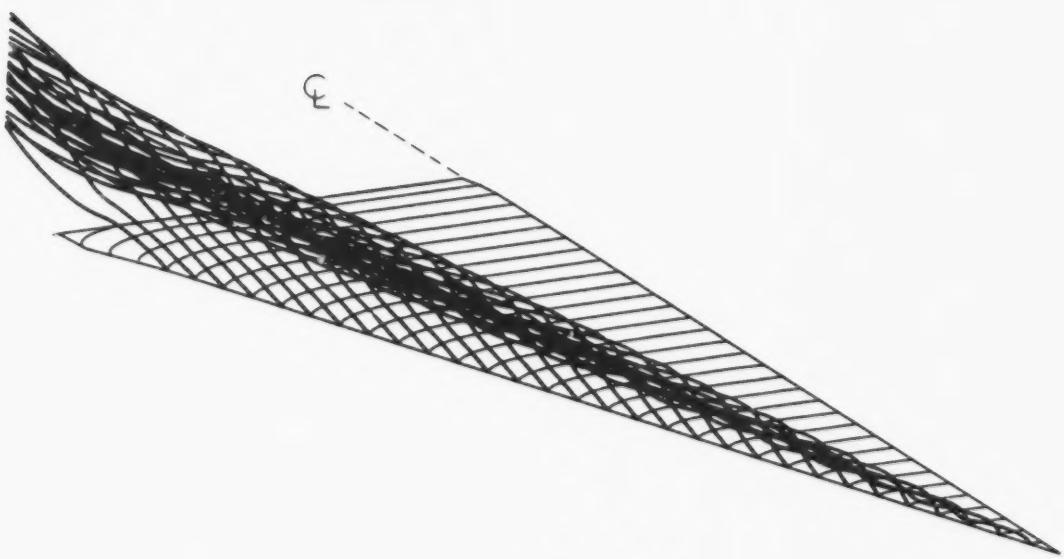

Figure 3.4: Particle traces emanating near the leading edge of a 70°-sweep delta wing at $\alpha = 10°$ ($C_\mu = 0$).

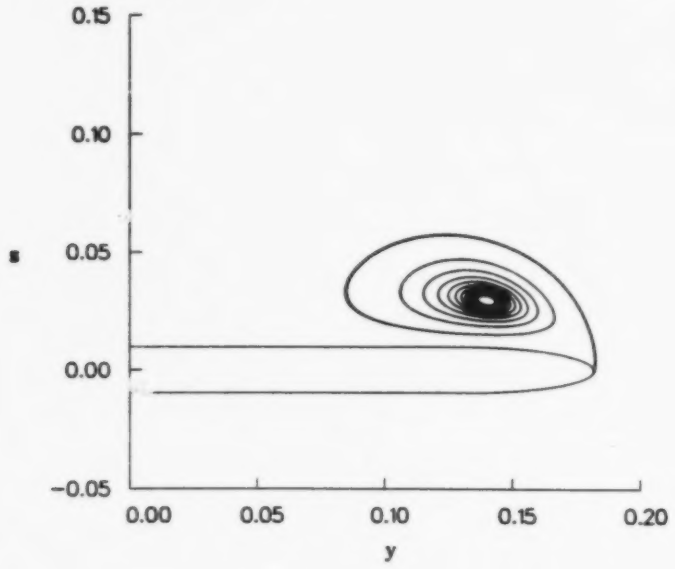

Figure 3.5: Particle traces emanating near the leading edge on the conical projection plane at $x/c_0 = 0.5$, $\alpha = 10°$ ($C_\mu = 0$).

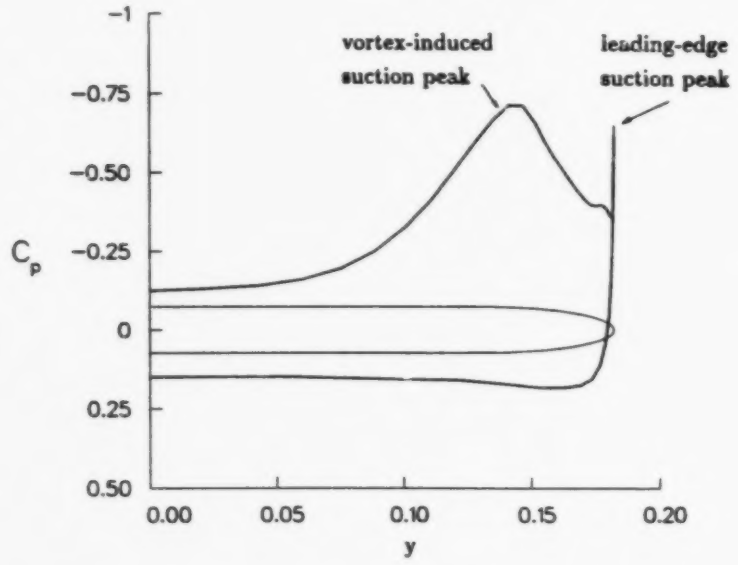

Figure 3.6: Computed spanwise surface pressure coefficient (C_p) distribution at $x/c_0 = 0.5$, $\alpha = 10°$ ($C_\mu = 0$).

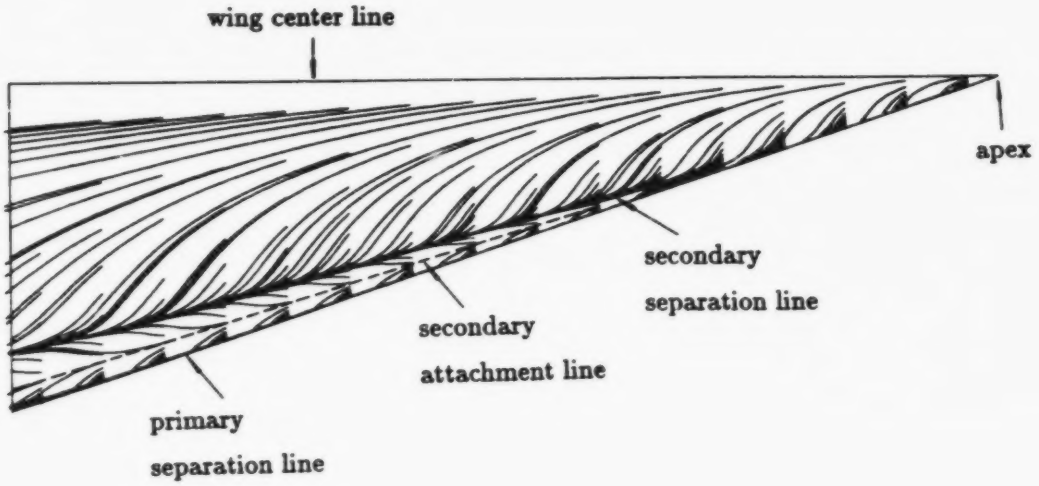

Figure 3.7: Computed near-surface flow pattern for a 70°-sweep delta wing at $\alpha = 10°$ ($C_\mu = 0$).

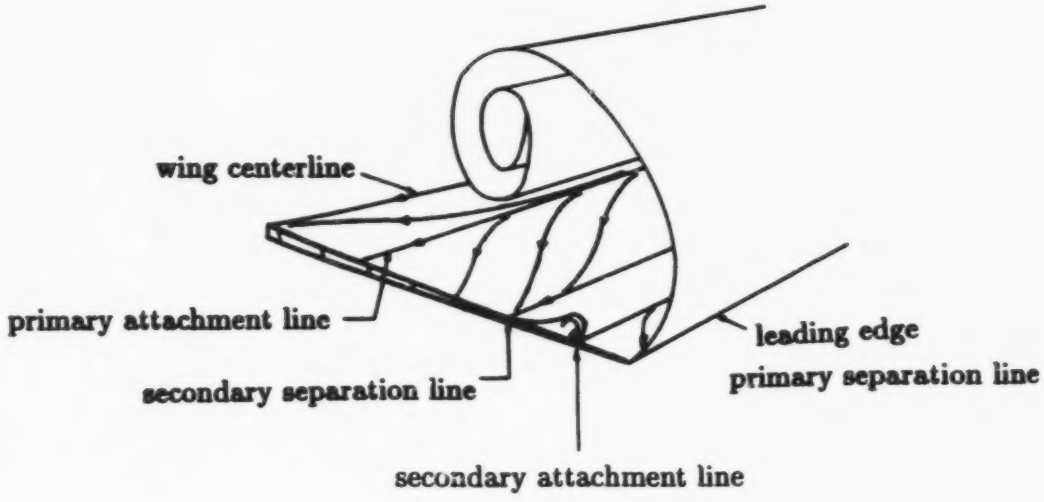

Figure 3.8: Schematic view of vortical flow pattern on the upper surface of a delta wing (Ref. 50).

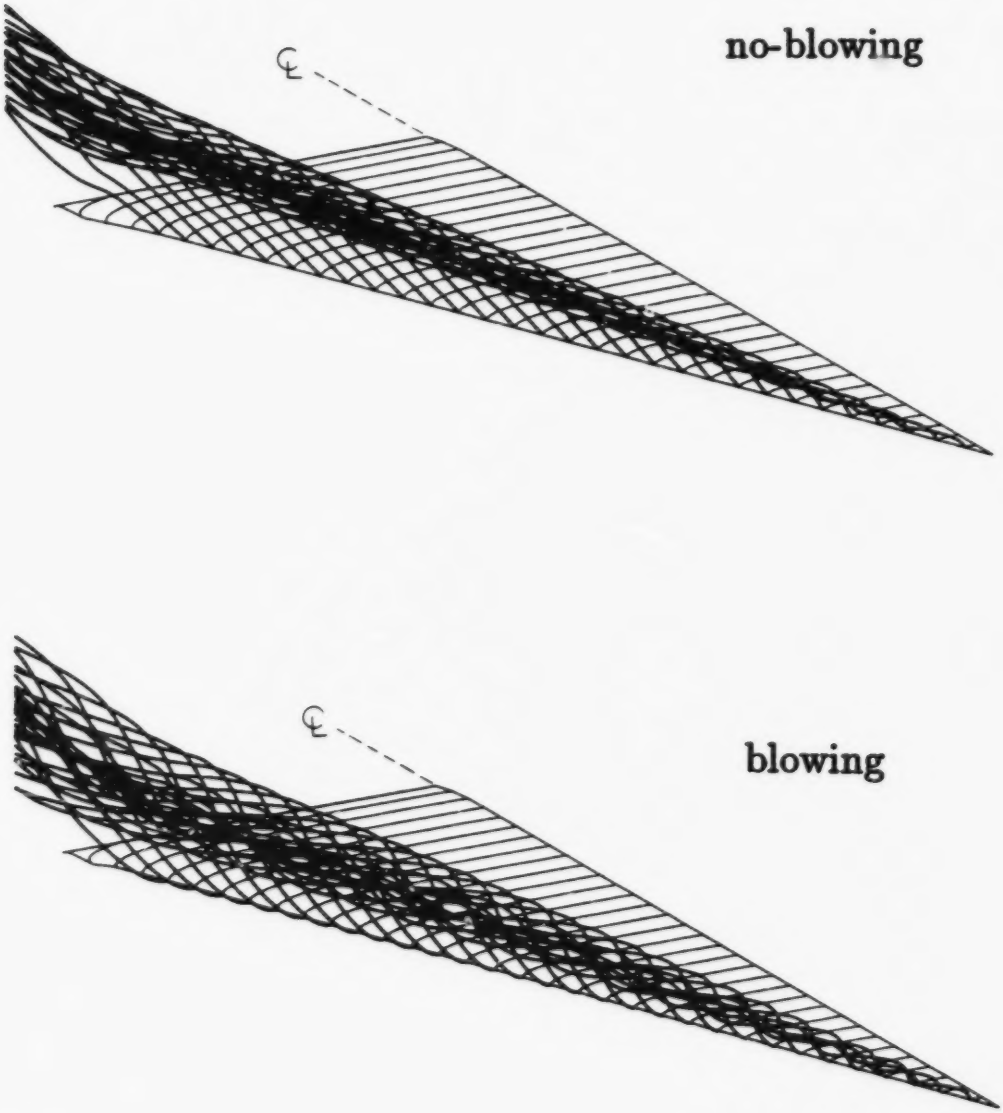

Figure 3.9: Particle traces emanating near the leading edge of a 70°-sweep delta wing without blowing and with blowing ($C_\mu = 0.047$) at $\alpha = 10°$.

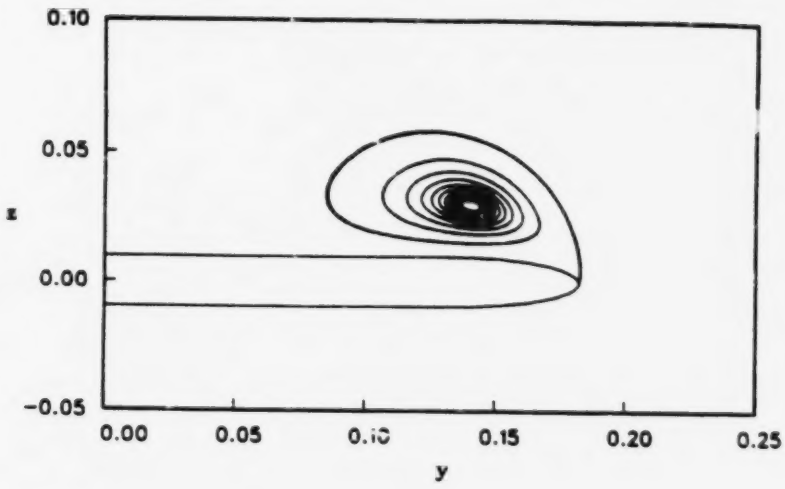

$(a) C_\mu = 0.$

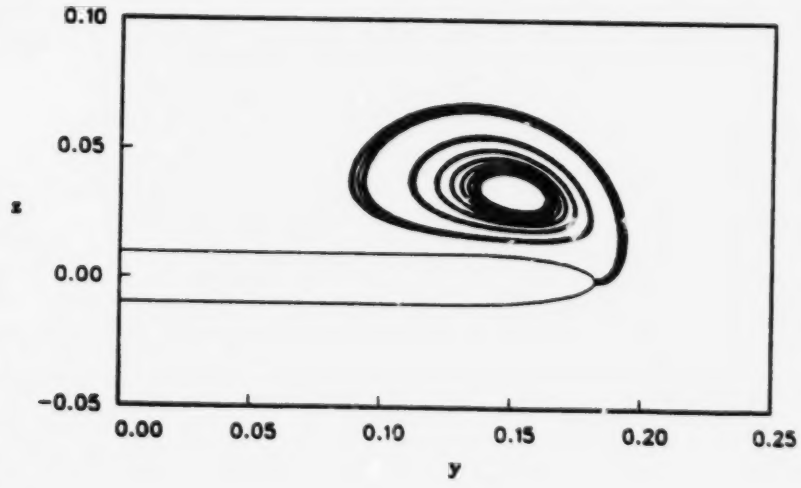

$(b) C_\mu$ .0235

Figure 3.10: Effect of spanwise blowing on the vortex traces on the conical projection plane at $x/c_0 = 0.5$, $\alpha = 10°$, for $C_\mu = 0.$, .0235, .0470, .094.

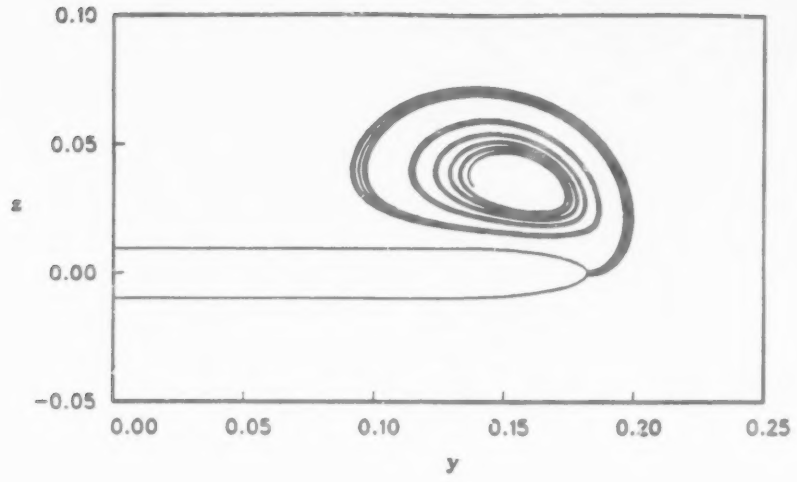

$(c) C_\mu = .0470$

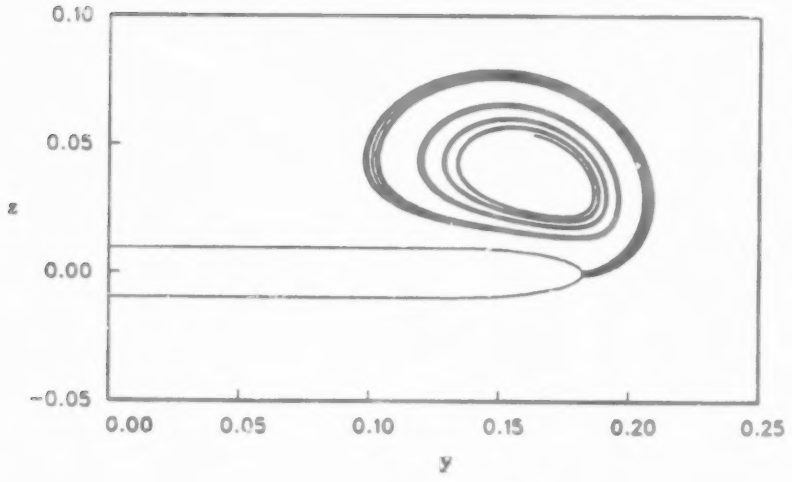

$(d) C_\mu = .0940$

Figure 3.10: Concluded.

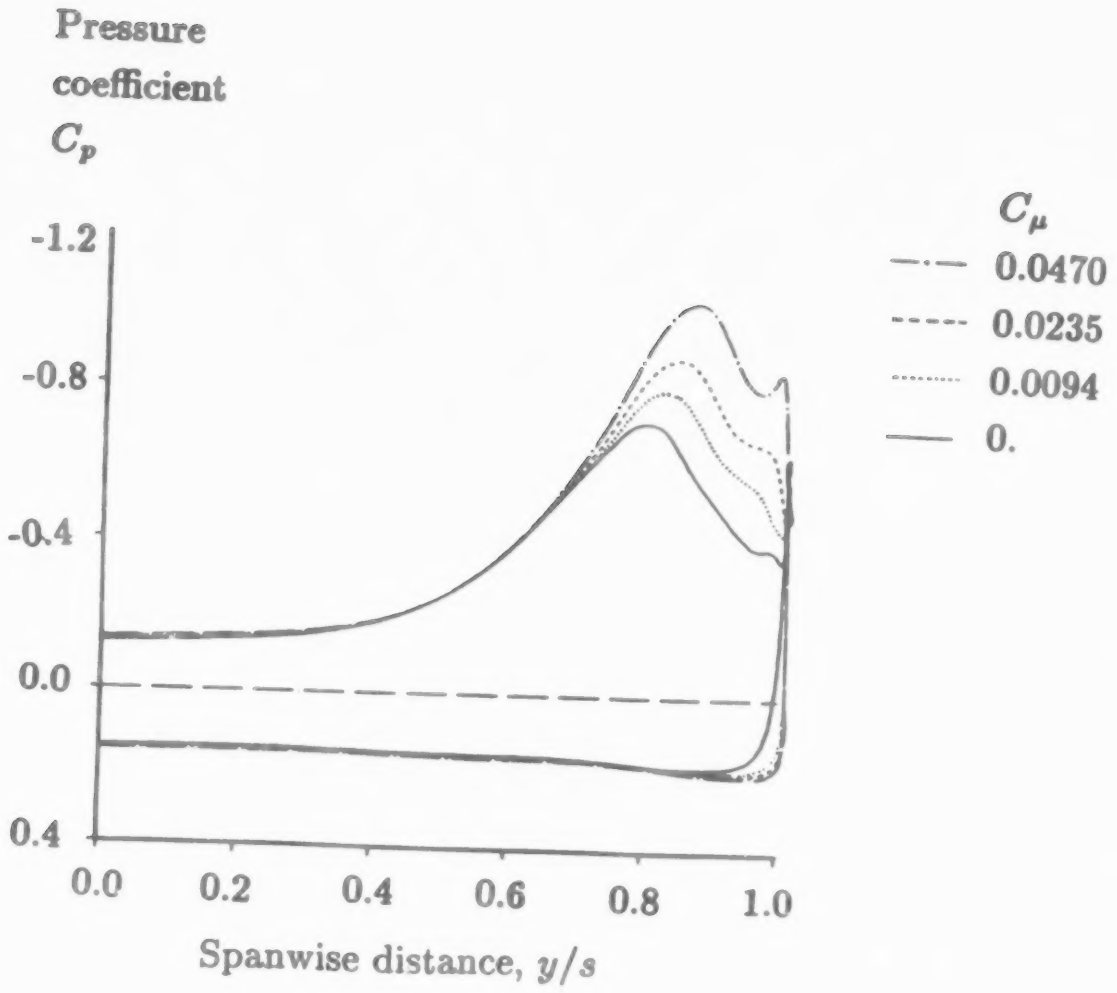

Figure 3.11: Effect of spanwise blowing on surface pressure distribution at $x/c_0 = 0.5$, $\alpha = 10°$, for $C_\mu = 0.$, .0094, .0235, .0470.

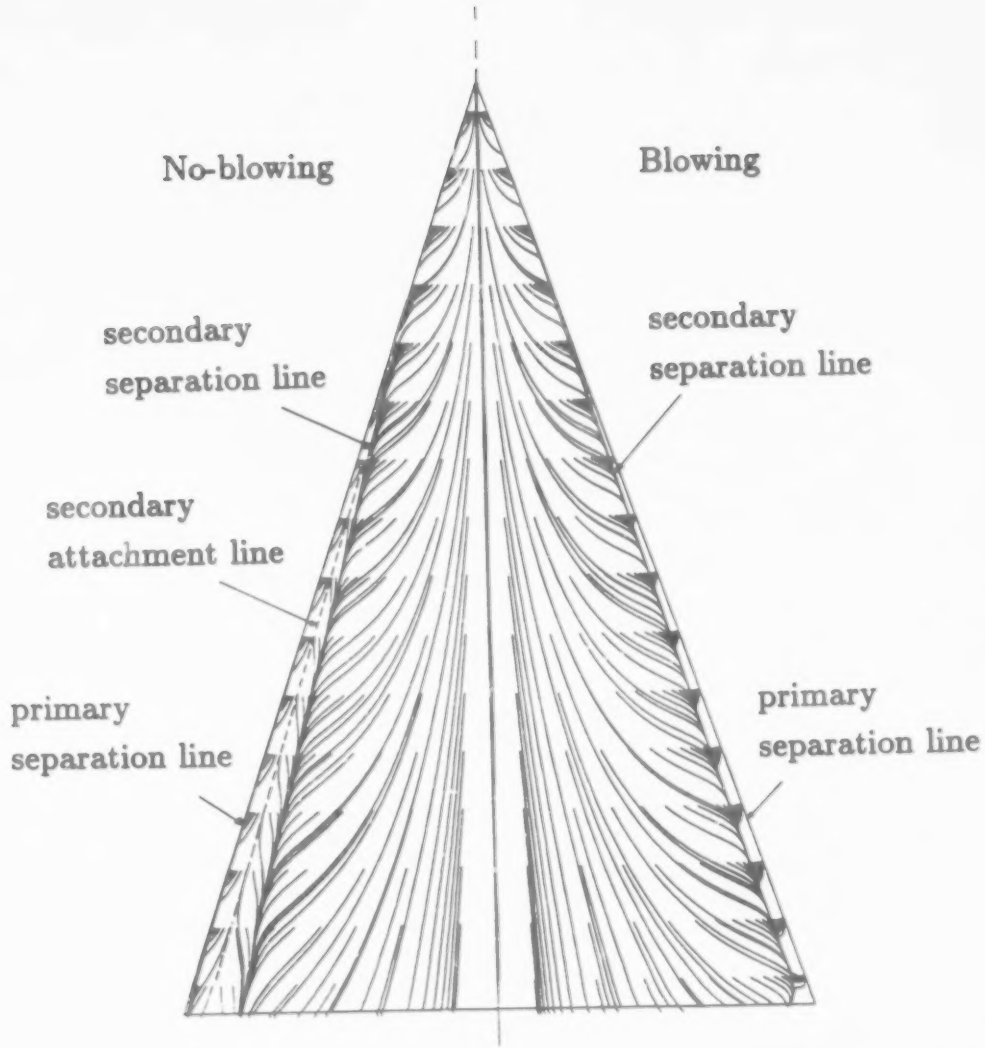

Figure 3.12: Computed near-surface flow pattern for no blowing (on the left) and $C_\mu = .0705$ (on the right) cases at $\alpha = 10°$.

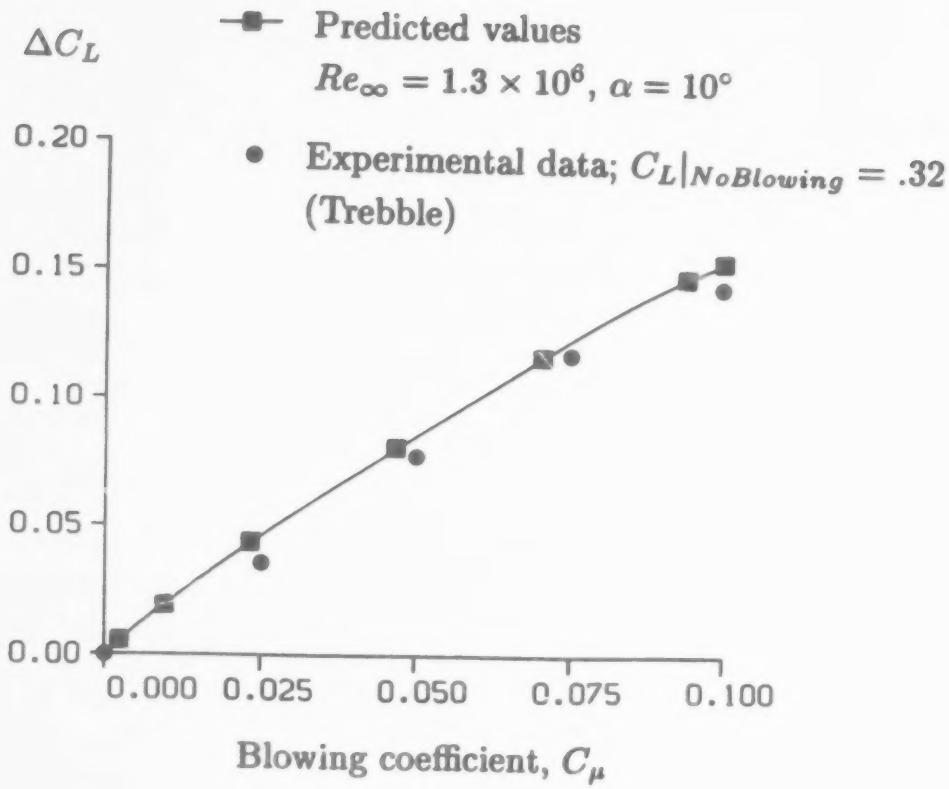

Figure 3.13: Comparison of computed and experimental results for a delta wing of AR = 1.4 with leading edge blowing at $\alpha = 10°$.

Angle of Attack (α) in degrees	Normal Force Coefficient (C_N)	
	$C_\mu = 0.00$	$C_\mu = 0.05$
0	0.00	0.00
10	0.38	0.49
20	0.88	0.99
30	1.33	1.47
35	1.50	1.45
40	1.18	1.30

Table 3.1: Effects of spanwise leading blowing on total wing normal force ($C_\mu = 0$ and 0.05).

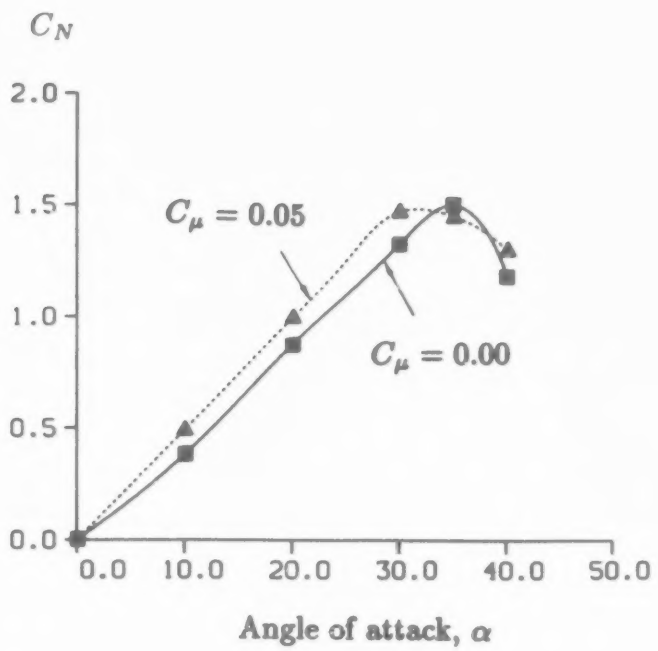

Figure 3.14: Variation of computed normal force coefficient with angle of attack for $C_\mu = 0$ and 0.05 .

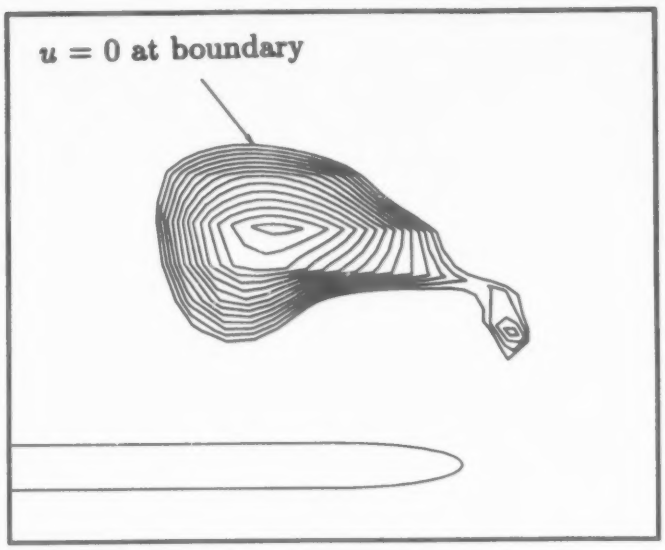

$u_{max} = 0.0$
$u_{min} = -0.14$
$\Delta u = -0.01$

Figure 3.15: Negative-u velocity contour for the no-blowing case at $x/c_0 = 0.77$, $\alpha = 40°$.

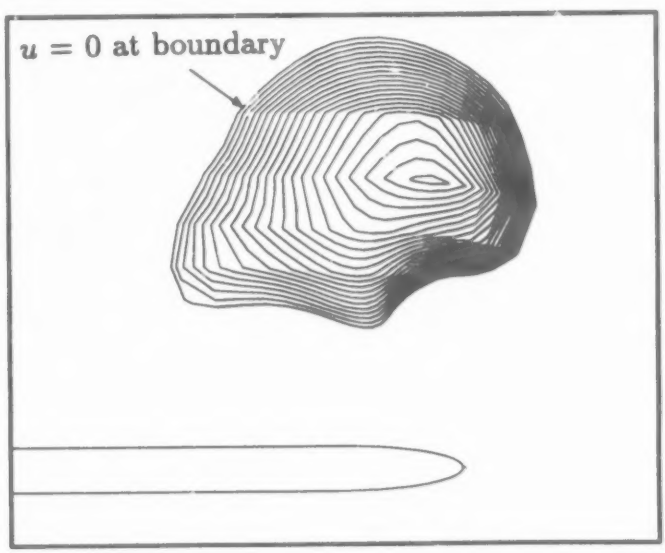

$u_{max} = 0.0$
$u_{min} = -0.20$
$\Delta u = -0.01$

Figure 3.16: Negative-u velocity contour for the blowing case ($C_\mu = 0.05$) at $x/c_0 = 0.77$, $\alpha = 40°$.

Chapter 4

Tangential Blowing

4.1 Introduction

The undesirable forces and moments induced by vortex breakdown and asymmetric vortex shedding during post-stall maneuvering adversely affect the controllability of the aircraft. Experiments [18, 19] have demonstrated that the vortical flow over a rounded leading edge delta wing can be controlled by tangential leading edge blowing. This is accomplished by controlling the cross-flow primary separation point with a thin, high-momentum jet issuing tangentially to the leading edge surface. As a result, the changes in the location of the cross-flow separation point modify the strength, stability and position of the resultant vortex as the flow field adjusts itself to an equilibrium state. This technique is somewhat analogous to the concept of circulation control for rounded trailing edge airfoils, where a thin tangential jet near the trailing edge separation point controls the location of the flow separation point and hence the circulation of the airfoil [53].

In this chapter, a rounded leading edge delta wing similar to that used in the

experiments [18, 19] is used to simulate the flow field at pre-stall and post-stall conditions, with and without tangential blowing. A multiple-grid, zonal approach is incorporated to accommodate the jet-slot geometry. Two types of zonal-interface, overlap and common boundary, are encountered and the interface boundary conditions are treated accordingly, as to be described in section 4.3. The leading edge jet is implemented through a set of "permeable" boundary conditions on the body surface. For the no blowing cases, the solid-wall boundary conditions are imposed at the jet-exit. The algebraic turbulence model of Baldwin and Lomax [41] is utilized near the wing surface. The algebraic turbulence model for a wall jet developed by Roberts [28], as described in section 2.5, is used in the jet region up to the point where the wall jet separates from the wing surface.

The simulations start with the no-blowing cases, illustrating the flow characteristics in pre-stall and post-stall conditions. Tangential blowing is implemented under the same free stream conditions, and the effects of blowing on the vortical flow field are discussed.

4.2 Multiple-Grid Concept and Grid Generation

A proper arrangement of grid distribution contributes to a successful numerical simulation. For solving the tangential leading edge blowing problem, a desirable surface-grid arrangement on a cross-flow plane is shown in figure 4.1, where the grid points are clustered near and at the jet slot.

The use of a single-zone, as described in Chapter 3, poses a major difficulty : the grid points tend to cross one another near the jet-exit due to both the large number

of grid points confined near the small jet-exit region and the orthogonality condition imposed by the hyperbolic grid-generation method [45, 46]. Although a number of other grid-generation schemes, such as algebraic or elliptical grid-generation methods, could be used to accomodate this geometry, the orthogonality condition normal to the wing surface is desirable for using the thin-layer approximations.

This leads to the utilization of a multiple-grid zonal scheme for the tangential blowing problem. Advantages of using this multiple-grid approach are the following :

(1) The grid for any subregion of the computational domain can easily be generated.

(2) Efficient grid distribution can be obtained such that a fine grid distribution can be used in the flow region where large gradients exit.

(3) A different set of equations can be solved, or different turbulence models can be incorporated in the subregion, as necessary.

The computational domain for the present problem consists of 3 zones. Grid 1 (zone 1) is first constructed by specifying an inner boundary surrounding the body at each cross-flow plane, as shown in figure 4.2. The inner boundary is at a local distance of 3 jet-slot widths from the upper wing surface and 2 jet-slot widths from the lower surface. For the regions where the leading edge jet-slot is not present (*i.e.* near the apex, trailing edge, upstream and downstream of the delta wing) the nearest jet-slot dimension is used. This inner boundary for Grid 1 extends from the upstream boundary to the downstream boundary in the computational domain. Once the grid distribution on this inner boundary is specified, Grid 1 is generated

through a two dimensional hyperbolic grid-generation method [35], as described in Chapter 3.

The second zone (Grid 2) fills the upper half of the open domain, which essentially covers the jet region and co-flowing region (where the jet and outer flow merge), as illustrated in figure 4.3. Similarly, Grid 3 is constructed by filling the lower half of the open domain such that Grid 2 and Grid 3 wrap entirely around the delta wing. Both Grid 2 and Grid 3 are generated algebraically under the constraint of the orthogonality condition normal to the wall. An exponential stretching function is used in these two zones to cluster the grid points near the wall. At each cross-flow plane, a common boundary line at the leading edge is shared between Grid 2 and Grid 3. The number of grid points of each zone that lie on a common boundary line is usually different, and their locations do not coincide with one another.

The final step is to redistribute the grid points along each radial curve in zone 1 such that Grid 1 starts from the last interior points of Grids 2 and 3. In other words, there are 2 grid points in Grid 1 that coincide with those in Grids 2 and 3. The spacing of this overlap region (figure 4.3) is determined as follows:

$$\epsilon_1 = \frac{\epsilon_2 + \epsilon_3}{2} \tag{4.1}$$

where the averaged grid spacing of Grid 2 (ϵ_2) and Grid 3 (ϵ_3) just outside of the overlap region is used. This is to ensure a smooth transition of grid spacing between zones. An exponential stretching function is also used in Grid 1 to extend the grid points to the outer boundary, with minimum spacing based on the length of the

overlap region (ϵ_1).

The final grid arrangement is similar to that shown in Chapter 3 (figure 3.3) except that the number of zones and the total number of grid points are different. The breakdown of the grid points for each zone is summarized as follows: Grid 1, $35\times35\times33 = 40,425$; Grid 2, $35\times18\times31 = 19,530$ and Grid 3, $35\times35\times25 = 15,750$, which results in a total number of 75,705 grid points. For each Grid, the numbers of grid points correspond to the ξ, η and ζ directions respectively.

4.3 Boundary and Jet-Exit Conditions

The boundary conditions used in this computation are essentially the same as those described in Chapter 3 with the exception of interface boundary conditions, encountered in the multiple-grid scheme. Since grid points coincide with one another in the overlap region as described in the previous section, the interface boundary conditions for Grid 1 are obtained directly from those of the interior points of Grid 2 and Grid 3. Conversely, the interface boundary conditions for Grid 2 and Grid 3 are determined from Grid 1. A linear interpolation is used at the common boundary between Grids 2 and 3. Since the number of grid points and their locations in these two zones are not the same at the interface boundary, the conservative flow variables ($\hat{Q}$) are fitted with a cubic spline before the interpolation is performed. The boundary conditions are summarized as follows:

(1) Free stream values are specified at the upstream and circumferential boundaries and remain fixed.

(2) Extrapolated values are used at the downstream boundary except for e, which is calculated based on the free stream static pressure for the present subsonic calculations.

(3) Symmetry conditions are imposed on the symmetry plane.

(4) No-slip, adiabatic wall and zero pressure gradient conditions are imposed at the wall, as discussed in section 3.3, except for the jet region when blowing is implemented.

It should be noted that the presence of the wall is felt by Grid 1 only through the interface overlap regions with Grid 2 and Grid 3.

The blowing momentum coefficient for the conical momentum distribution, for a jet exiting with the free-stream density is defined as follows

$$C_\mu = 2 \left(\frac{V_{jet}}{V_\infty}\right)^2 \left(\frac{h}{s}\right) \tag{4.2}$$

where V_{jet} is the jet-exit velocity, h is the local jet-slot width and s is the local span. Since conical flow conditions were intended in the experiments [18, 19], both the external dimension of the delta wing and the jet-slot width increase linearly from the apex, with $\left(\frac{h}{s}\right)$ having a constant value of 0.0046. The jet-exit boundary conditions are summarized as follows:

(1) The local static pressure is used at the jet-exit. This is approximated by taking the static pressure value at the nearest point in the spanwise direction from the leading edge.

(2) The free stream value of density is specified at the jet exit.

(3) The jet-exit velocity distribution is prescribed as a power function given by

$$V_j(y) = V_{jet}\left[1 - \left(\frac{\left|\frac{h}{2} - y\right|}{\frac{h}{2}}\right)^2\right]^{\beta} \tag{4.3}$$

which is modified from the expression for an ellipse ($\beta = \frac{1}{2}$). A distribution was chosen with $\beta = 0.1$ to simulate a turbulent wall jet velocity profile, as shown in figure 4.4. The maximum velocity magnitude is determined according to a specified C_μ from Eq.(4.2).

4.4 Results and Physical Interpretation

4.4.1 No Blowing

A 60°-sweep, rounded leading edge delta wing is used in the computations. The delta wing is modeled to have conical geometry up to 80 % of c_0 with a maximum thickness of 12.5 % of c_0 at $x/c_0 = 0.8$. The aft part of the wing consists of an afterbody whose thickness varies linearly toward the trailing edge, as shown in figure 4.5, to simulate a sharp trailing edge wing. This wing has the same proportions as the one used in Wood's experiments [18, 19] except that the experimental model didn't have the afterbody, thus ending in a blunt trailing edge, as shown in figure 1.4.

The experimentally prescribed values [18, 19] of $\alpha = 30°$ and $\alpha = 40°$, corresponding to pre-stall and post-stall conditions respectively, are used in the present no-blowing simulation, so that the flow characteristics under these conditions can be distinguished.

Figures 4.6(a), (b) show "particle traces" from particles released near the leading edge for 30° angle of attack, in plan and side views. The formation of a well organized vortical flow field is observed in these figures. A conical jet-slot dimension is simulated where the slot width increases linearly from about 20% to 80% (where the maximum body thickness occurs) of the root chord. It is interesting to note that some of the particles just in front of the afterbody are trapped in a recirculatory motion near the jet-slot, where solid wall boundary conditions are implemented. Releasing the particles from the same locations at $\alpha = 40°$, as shown in figures 4.7(a), (b), a chaotic behavior of the flow is revealed above the wing, indicating a reverse flow region associated with vortex breakdown. This representation of vortex breakdown can often be found in recent publications [31, 54]. From observation of the cross-flow velocity profiles at $\alpha = 40°$, (to be shown in the next section), the flow separates near the leading edge just ahead of the jet-slot, so that particles are no longer trapped.

Since the "particle traces" depend on the particle release location, these particle paths can only qualitatively represent the region where vortex breakdown occurs. A more precise representation is to plot the cross-sectional reverse-flow velocity (negative-u velocity) contours at a number of selected streamwise locations, as show in figure 4.8. These streamwise stations are chosen arbitrarily at $x/c_0 \approx .17, .29, .42, .54, .67, .79$, and .92. For $\alpha = 30°$, the reverse flow bubble does not appear (not plotted), whereas at $\alpha = 40°$ large regions of reverse flow are observed indicating extensive vortex breakdown. In addition, the parameter $\tilde{u}$ at each cross-flow plane is defined as the ratio of the maximum reverse-flow (negative-u) velocity to the free stream velocity

$$\tilde{u} = \frac{\text{negative-u}|_{max}}{V_\infty} \tag{4.4}$$

On each cross-flow plane, the outer contour has zero negative-u velocity, which can be interpreted as the reverse flow bubble boundary. The values of $\tilde{u}$ indicated in figure 4.8 refer to the innermost contour of the corresponding station.

Another phenomenon associated with vortex breakdown is the rapid expansion of the vortex core region. This can be demonstrated by means of total pressure contours, as shown in figure 4.9, for the station at $x/c_0 = 0.36$. For $\alpha = 30°$, the vortex is highly concentrated with a strong loss in total pressure in the vortex core region. For $\alpha = 40°$, the vortex appears diffused, the loss in total pressure is less significant and extends over a much larger region.

Figure 4.10 (a) shows the comparison of computed spanwise pressure distribution for $\alpha = 30°$, $x/c_0 = .36$ with that from experiments [18, 19]. Agreement is good in the sense that the predicted and measured location and strength of the vortex-induced suction peak are similar. The discrepancy near the root chord may be attributed to the displacement thickness associated with the formation of the boundary layer on the wind tunnel side wall, which may have translated in an outboard displacement of the pressure curve. Another factor could be the lack of grid resolution in that area.

The comparison for $\alpha = 40°$ at the same chord location is shown in figure 4.10 (b), where good agreement with experiments is also obtained. In this case, a nearly flat pressure distribution on the wing upper surface signifies a weak and diffused vortical flow, another indication that vortex breakdown has occurred.

Figures 4.11 (a) and (b) show the computed near-surface streamline patterns for $\alpha = 30°$ and $\alpha = 40°$. At $\alpha = 30°$, a typical vortical flow pattern on the upper surface similar to that described in Chapter 3 is observed. At $\alpha = 40°$, however, the adverse pressure gradient in the longitudinal direction associated with vortex breakdown, accompanied by the diminishing influence of the vortical flow, causes reverse flow on the wing surface. The afterbody separation due to the rapid change in the slope of the wing surface at 80% of the root chord is apparent in both cases.

The computed normal force coefficient versus angle of attack for no blowing is shown in figure 4.12, where $C_{N_{max}}$ occurs approximately at $\alpha = 30°$. The decrease in normal force at $\alpha = 40°$, due to massive vortex breakdown is evident.

4.4.2 Tangential Blowing

The same delta wing and grid arrangement are used for the tangential blowing simulations. The conical jet slot geometry extends from 17% to 79% of the root chord with a constant jet-slot width (h) to local wing span (s) ratio, $\frac{h}{s} = 0.0047$. The same angles of attack ($\alpha = 30°$ and $40°$), are used in the blowing calculations as in the no-blowing cases, so that the effects of tangential blowing can be identified through parallel comparison.

At $\alpha = 30°$ with $C_\mu = 0.05$, figure 4.13(a) shows the side and plan views of "particle traces" emanating from the same locations as those in the no-blowing case (figure 4.6(a)). Very little difference is observed between the blowing and no-blowing cases, except that the particle traces appear to reduce in extent above the wing due to blowing and particles are not trapped near the jet-slot as in the no-blowing case.

In addition, the flow near the leading edge seems to align with the direction of the jet until the influence of the jet becomes small, which produces the rapid change in slopes of the particle traces near the leading edge, as shown in figure 4.14 (a). At $\alpha = 40°$ with $C_\mu = 0.038$, figures 4.14 (b) reveals the effect of blowing on the vortex traces. The chaotic behavior of the vortical flow as seen in the no-blowing case (figure 4.7) is limited only to the region near the trailing edge, and the extent of the vortical flow is reduced, implying that tangential blowing delays and stabilizes the vortical flow in post-stall conditions. It is interesting to note that the reverse flow bubble extends up to the region where there is a rapid change in body geometry and beyond the extent of the jet-slot.

The favorable influence of tangential blowing on the vortical flow in the presence of vortex breakdown is further illustrated by the reverse-flow velocity contours in the longitudinal direction, as shown in figure 4.15. Strong reductions in extent and strength of the reverse-flow bubble at $\alpha = 40°$ are observed as compared to the no-blowing case shown in figures 4.8.

The effect of blowing is also illustrated by total pressure contours at $x/c_0 = 0.36$, as shown in figure 4.16. At $\alpha = 30°$, blowing tends to move the vortex core region inboard and closer to the upper surface as compared to the no-blowing case (figure 4.9 (a)). For $\alpha = 40°$, a greater loss in total pressure associated with a concentrated vortex core is observed, as compared to that in the no-blowing case (figure 4.9(b)), indicating that blowing re-establishes the vortical flow in the post-stall conditions.

Figure 4.17 shows the comparison of the computed surface pressure distribution

with Wood's experimental results at $x/c_0 = 0.36$ for $\alpha = 30°$ and $40°$. The agreement is good for both angle-of-attack cases. However, the predicted suction peak associated with the jet is not as high as that obtained experimentally. This discrepancy may be attributed to the lack of grid resolution near the jet region. Grid refinement studies were not conducted due to limitations of computer memory.

Figure 4.18 shows the computed spanwise surface pressure distribution at $x/c_0 = 0.36$ for $\alpha = 30°$, with and without blowing, to illustrate the effects of blowing in pre-stall condition. It is observed that blowing tends to reduce the vortex-induced pressure peak while increasing the suction peak around the leading edge. This indicates that the delayed separation of the cross-flow boundary layer modifies the strength and position of the resultant vortex as the flow field adjusts itself to a new equilibrium state. Figure 4.19 illustrates the changes of the primary separation point in the cross-flow plane, with and without blowing.

Figure 4.20 illustrates the effect of blowing momentum on the spanwise pressure distribution at $x/c_0 = 0.36$ for $\alpha = 40°$. The effect of blowing is quite apparent: blowing re-establishes the vortical flow, as indicated by the vortex induced suction peak, and creates an additional suction peak around the leading edge. These phenomena may be attributed to the reduction of vortex strength brought about by altering the cross-flow separation point through the wall jet, as shown in figure 4.21. In the absence of blowing, the vortex would burst. As a result of the re-establishment of orderly vortical flow, the integrated value of the surface pressure increases, which translates into higher normal force on the wing.

The effect of blowing on the computed near-surface flow patterns on the upper

surface of the delta wing for $\alpha = 30°$ and $40°$ are shown in figures 4.22 (a) and (b). At $\alpha = 30°$, the surface flow pattern is similar to that in the no-blowing case (figure 4.11(a)), except that the secondary separation line appears to move inboard slightly indicating an inward motion of the vortex due to blowing. For $\alpha = 40°$, the recovery of the familiar vortical flow pattern due to blowing is quite obvious as compared to the no-blowing case (figure 4.11(b)). The reverse flow region due to vortex breakdown in the no-blowing case has been removed, an indication of the restoration of orderly vortical flow. Due to the rapid change in body geometry and the finite extent of the leading edge jet (17% - 79% of c_0), the afterbody separation still remains, as shown in figures 4.22 (a) and (b).

Figure 4.23 illustrates the computed normal force coefficient as a function of the angle of attack for no blowing and blowing with a constant blowing momentum coefficient of 0.05. Three observations can be made about these results :

(1) Tangential blowing delays vortex breakdown at high angles of attack, thereby increasing the stall angle or the angle of attack at which $C_{N_{max}}$ occurs.

(2) Tangential blowing restores the vortical flow in the post-stall conditions, increasing the maximum normal force on the wing.

(3) In pre-stall conditions, tangential blowing tends to reduce the pressure peak associated with the vortex and to increase the suction peak around the leading edge such that the integrated value of the surface pressure remains about the same. In other words, these two pressure peaks offset one another resulting in a nearly constant pressure-induced lift.

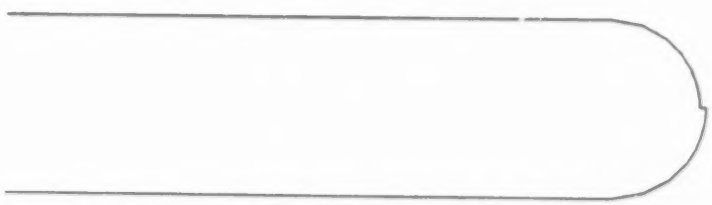

(*a*) Geometry of a typical cross section.

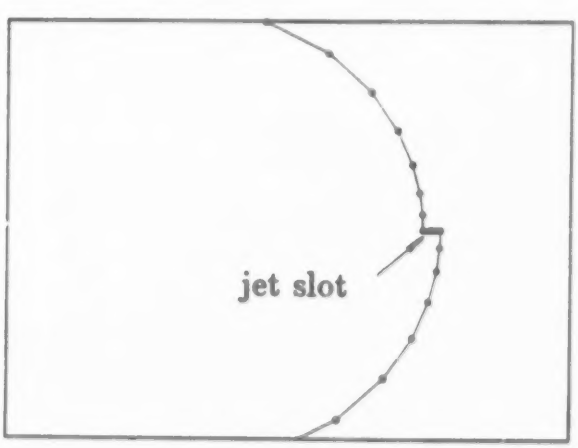

(*b*) Close-up view of the jet-slot geometry.

Figure 4.1: Jet-slot geometry and location in the cross-flow plane.

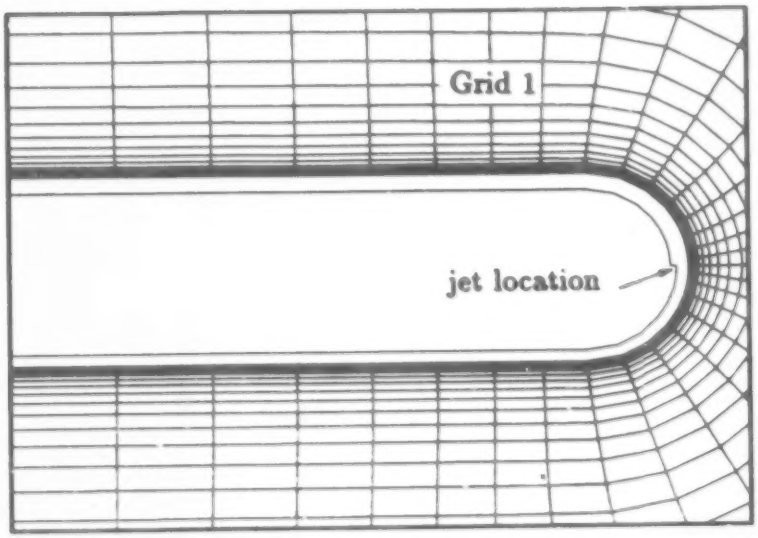

Figure 4.2: Illustration of Grid 1 arrangement in the cross-flow plane.

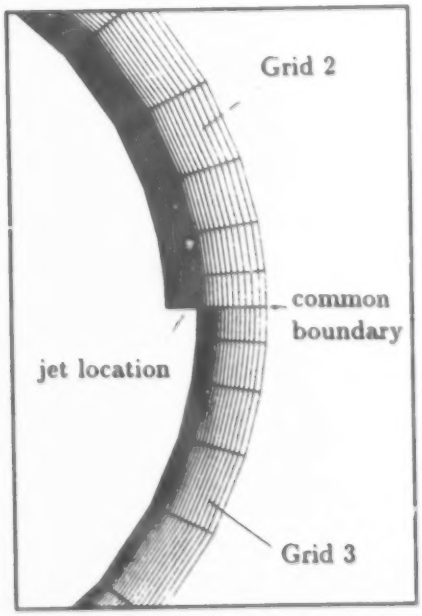

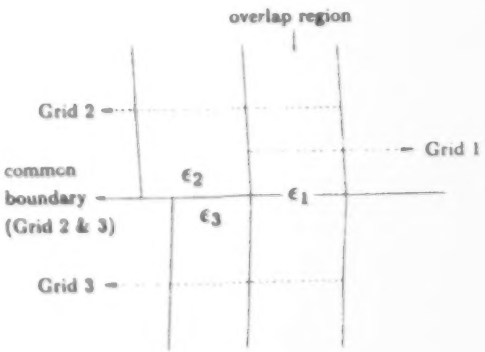

Figure 4.3: Illustration of Grid 2 and Grid 3 arrangements in the cross-flow plane.

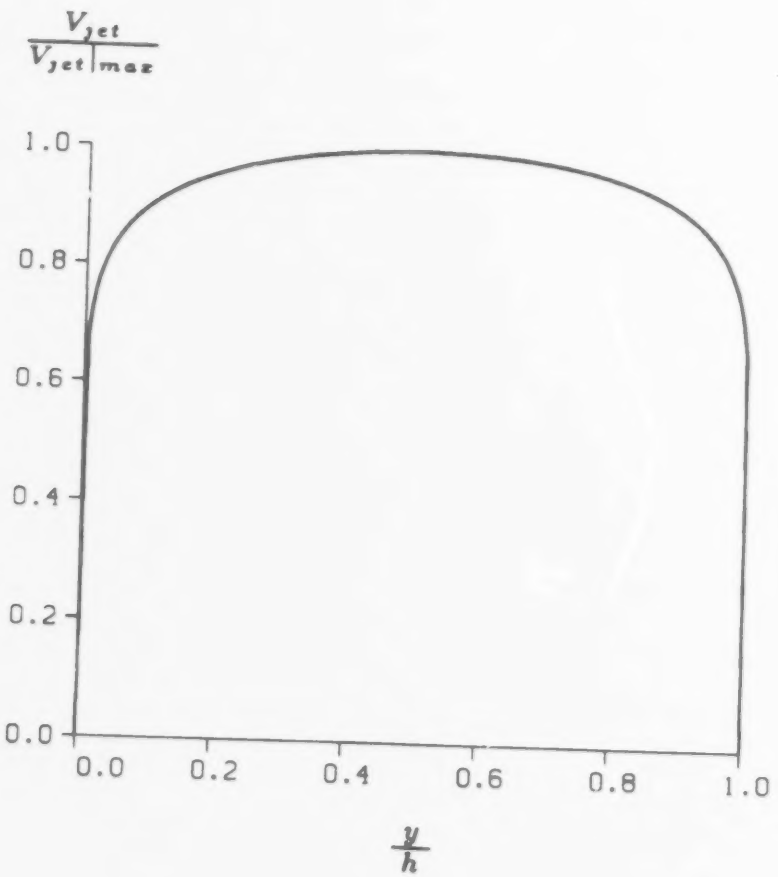

Figure 4.4: Turbulence wall jet velocity profile in tangential blowing.

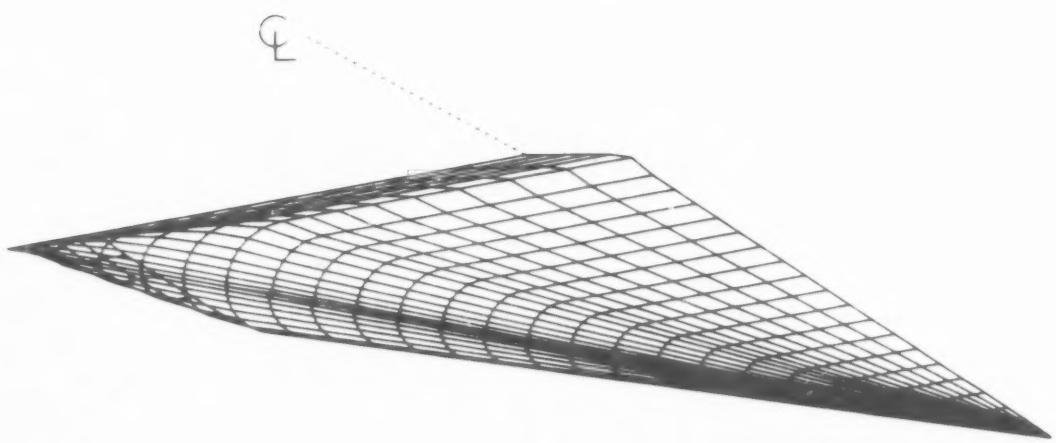

Figure 4.5: Delta wing geometry used in the tangential blowing simulations.

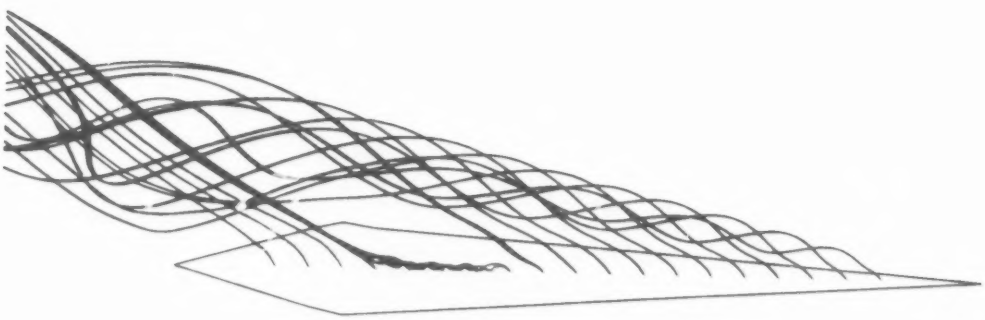

(*a*) Side view.

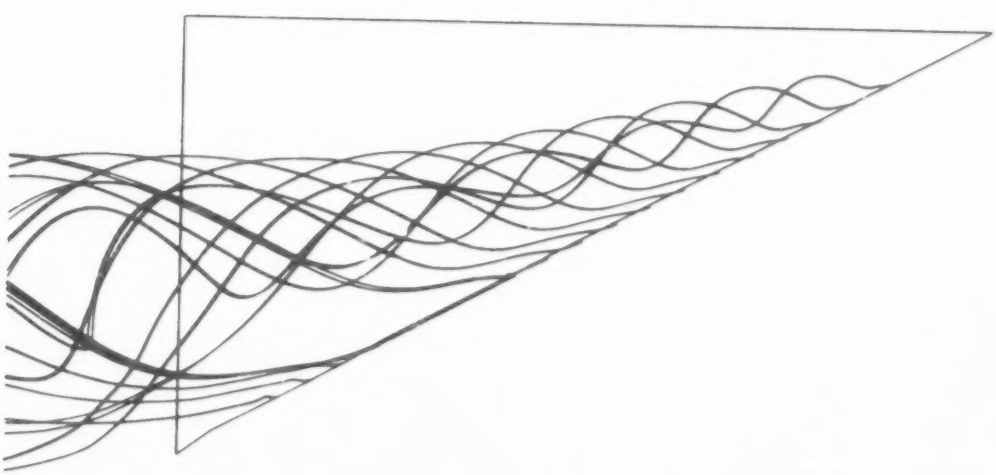

(*b*) Plan view.

Figure 4.6: Illustration of vortex structure with particle traces for $\alpha = 30°$, $C_\mu = 0$.

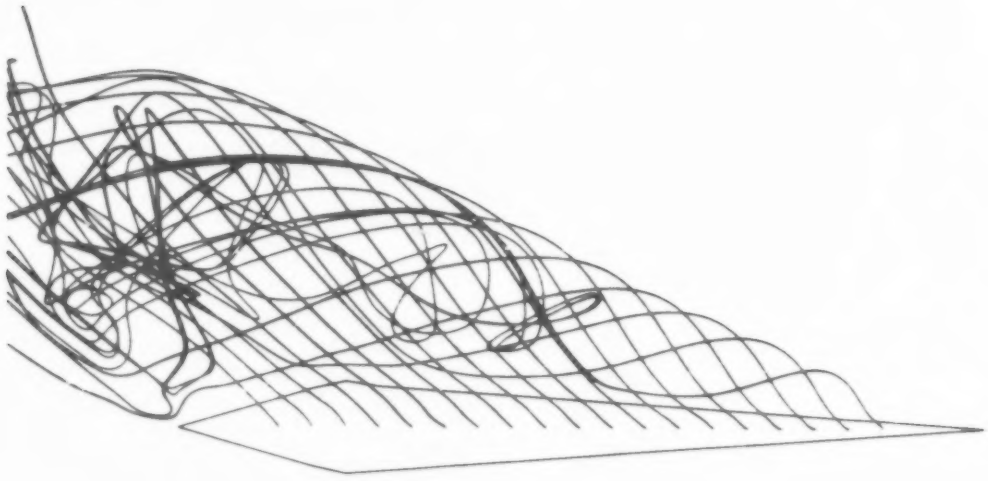

(*a*) Side view.

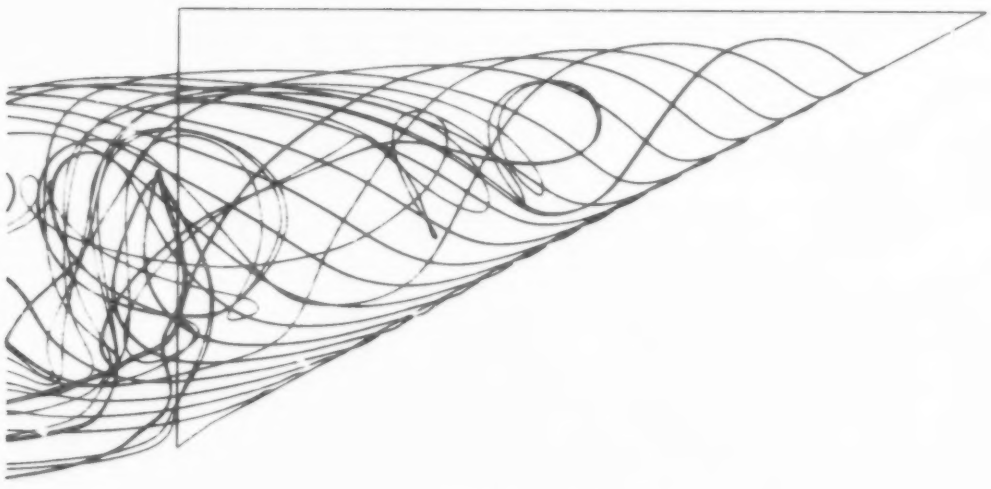

(*b*) Plan view.

Figure 4.7: Illustration of vortex structure with particle traces for $\alpha = 40°, C_\mu = 0$.

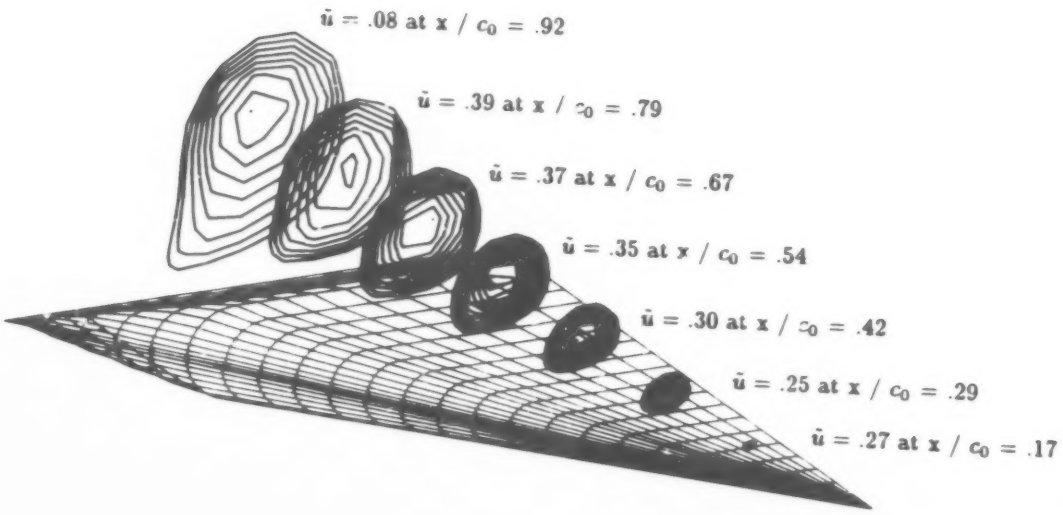
$\tilde{u}$ = .08 at x / c_0 = .92
$\tilde{u}$ = .39 at x / c_0 = .79
$\tilde{u}$ = .37 at x / c_0 = .67
$\tilde{u}$ = .35 at x / c_0 = .54
$\tilde{u}$ = .30 at x / c_0 = .42
$\tilde{u}$ = .25 at x / c_0 = .29
$\tilde{u}$ = .27 at x / c_0 = .17

Figure 4.8: Reverse-flow velocity contours at selected chordwise locations, $x/c_0 =$ .17, .29, .42, .54, .67, .79, .92, for $C_\mu = 0$, $\alpha = 40°$.

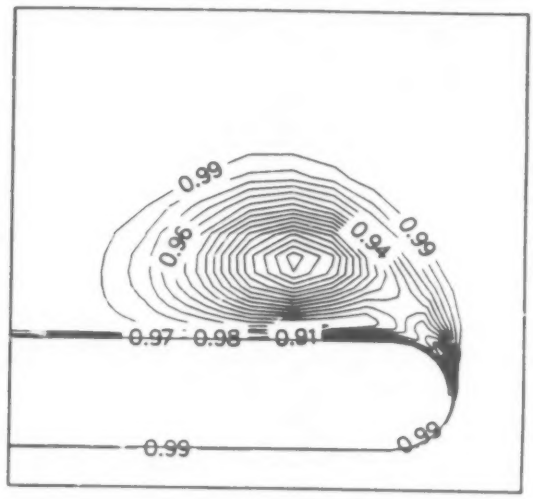

(a) $\alpha = 30°, C_\mu = 0.$

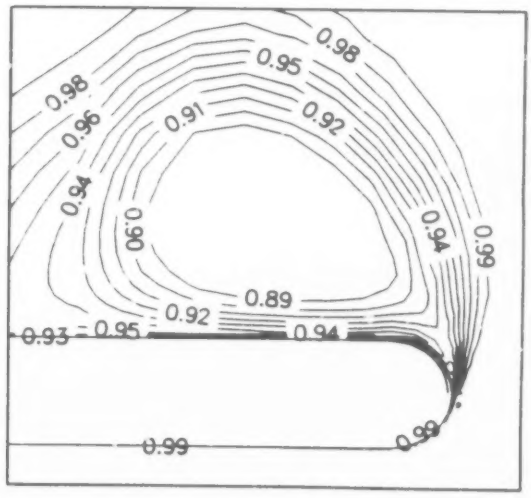

(b) $\alpha = 40°, C_\mu = 0.$

Figure 4.9: Normalized total pressure contours at $x/c_0 = 0.36$ for $\alpha = 30°$ and $\alpha = 40°$ ($C_\mu = 0$).

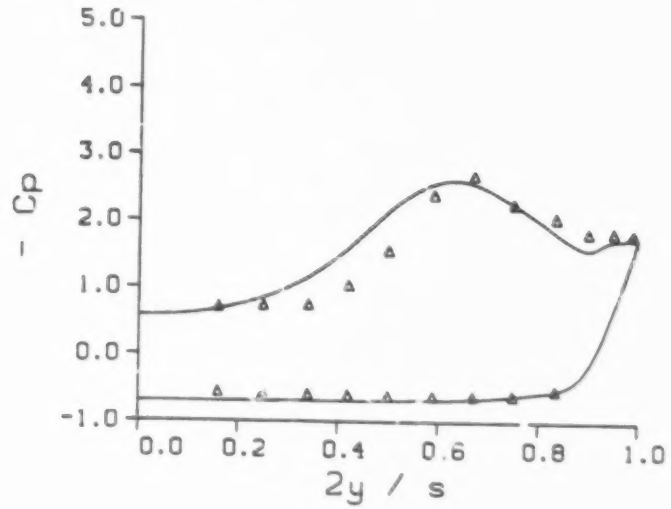

(*a*) $\alpha = 30°$

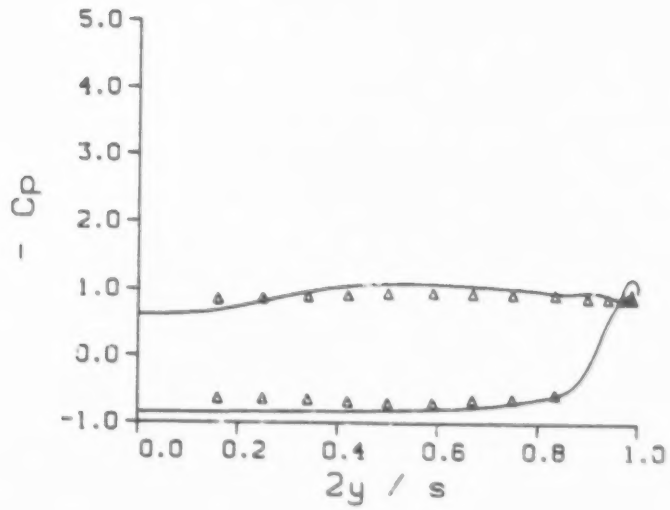

(*b*) $\alpha = 40°$

Figure 4.10: Comparison of computed spanwise surface pressure distribution with experimental results at $x/c_0 = 0.36$ for $\alpha = 30°$, $40°$ and $C_\mu = 0$.

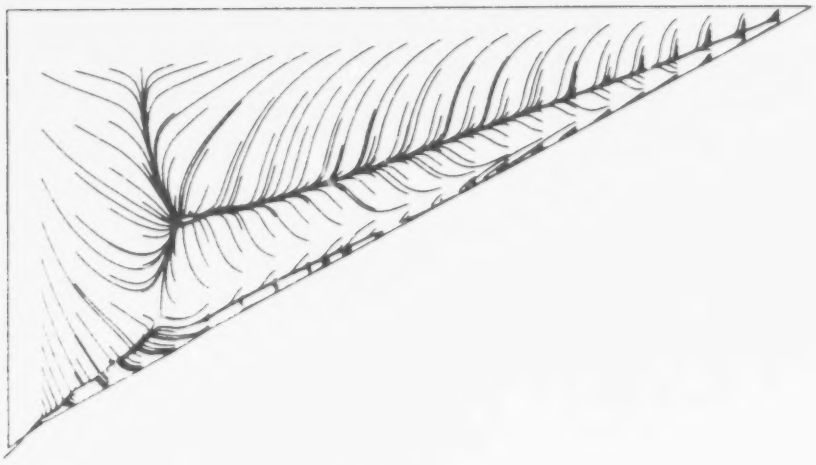

(*a*) $\alpha = 30°$.

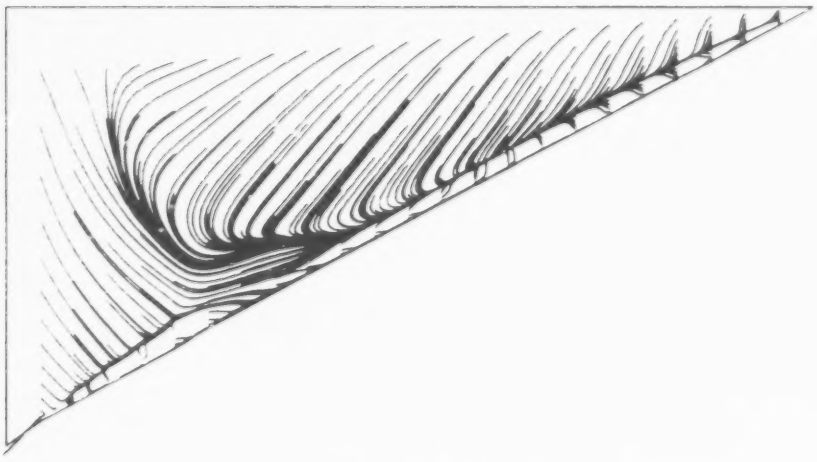

(*b*) $\alpha = 40°$.

Figure 4.11: Computed near-surface streamline patterns for $C_\mu = 0$, $\alpha = 30°$ and $\alpha = 40°$.

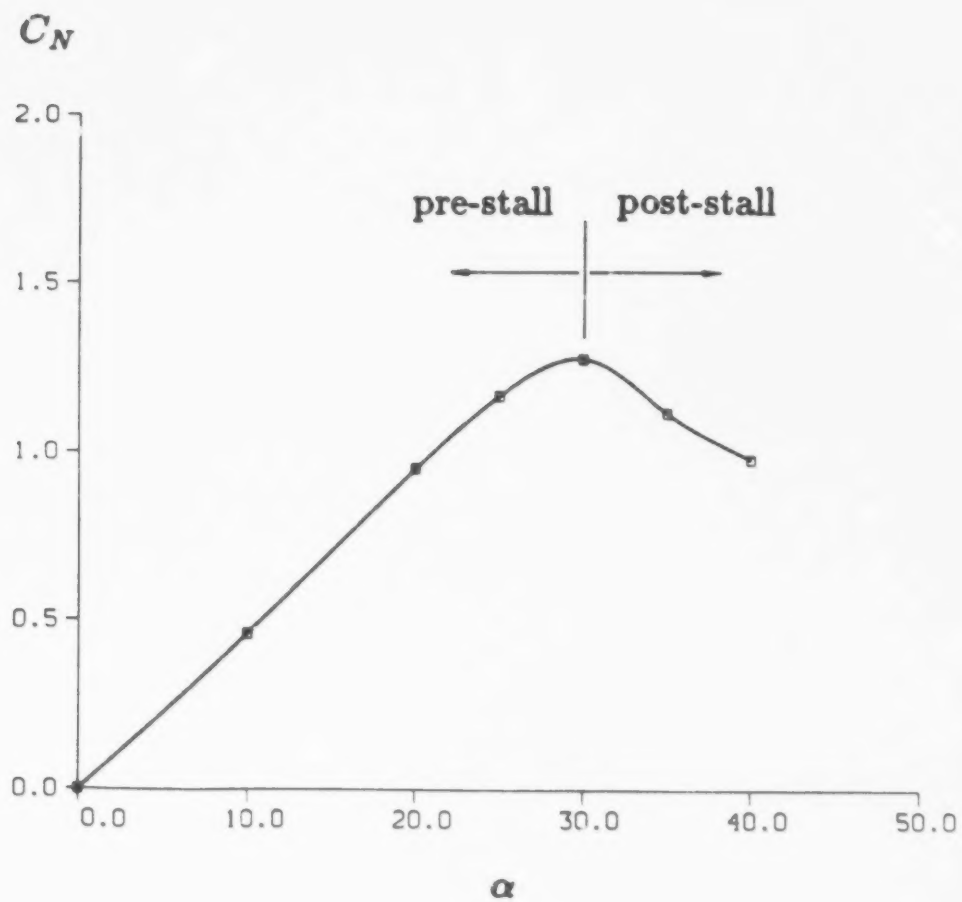

gure 4.12: Computed normal force coefficient as a function of angle of attack for $C_\mu = 0$.

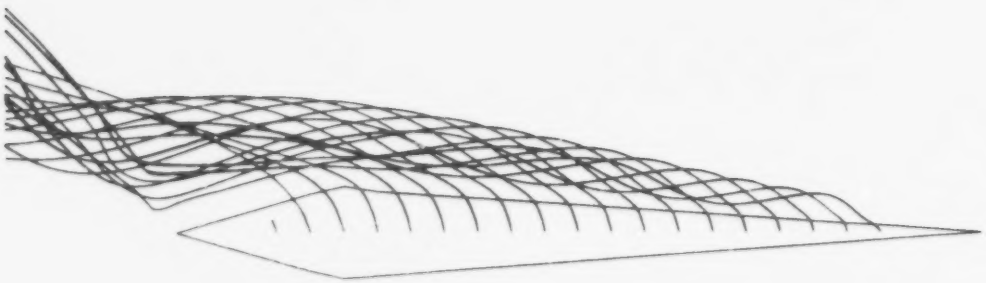

(*a*) Side view.

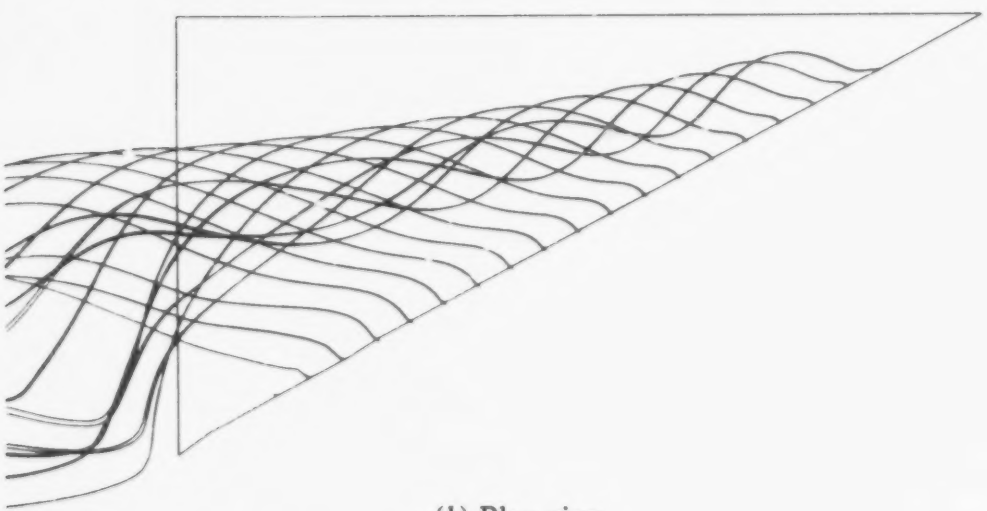

(*b*) Plan view.

Figure 4.13: Illustration of vortex structure with particle traces, for $\alpha = 30°$, $C_\mu = 0.05$.

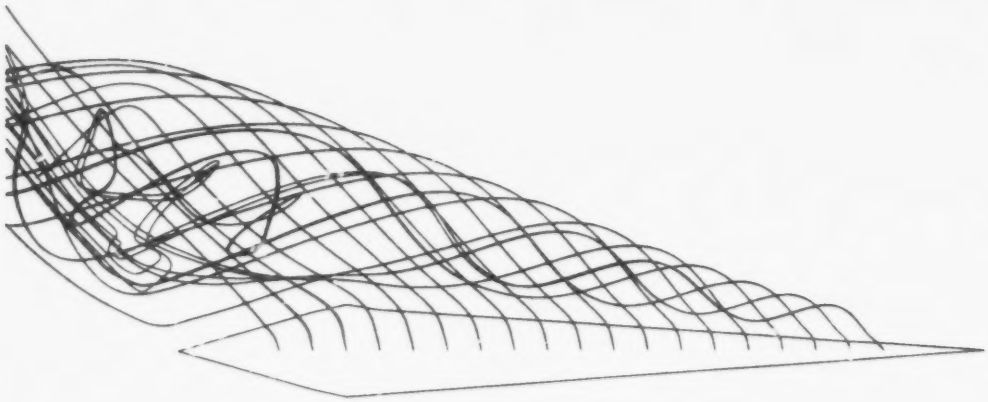

(*a*) Side view.

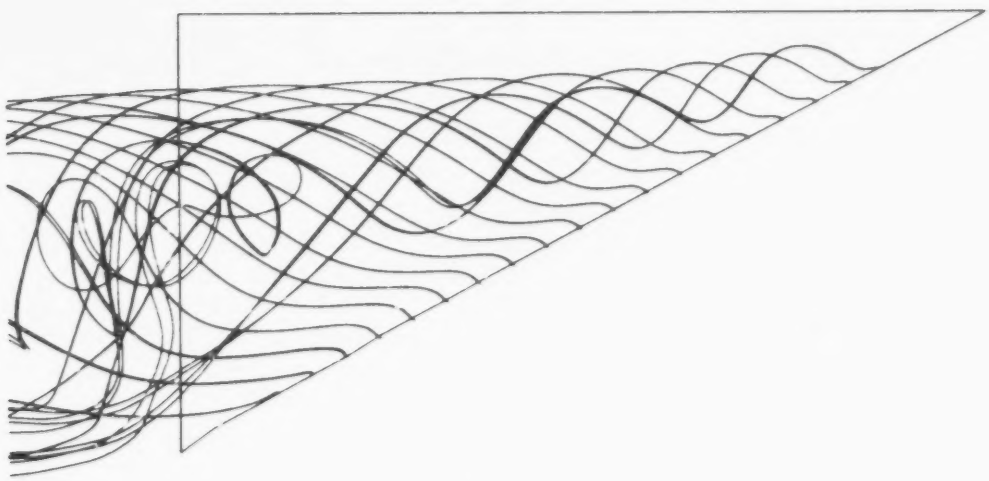

(*b*) Plan view.

Figure 4.14: Illustration of vortex structure with particle traces, for $\alpha = 40°$, $C_\mu = 0.038$.

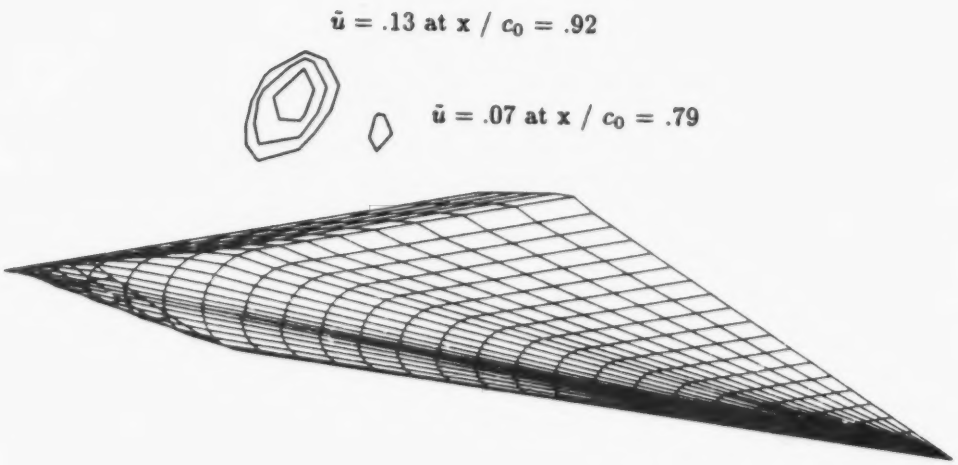

Figure 4.15: Reverse-flow (negative-u) velocity contours at selected chordwise locations, x/c_0 = .17, .29, .42, .54, .67, .79, .92, for $\alpha = 40°$, $C_\mu = 0.038$.

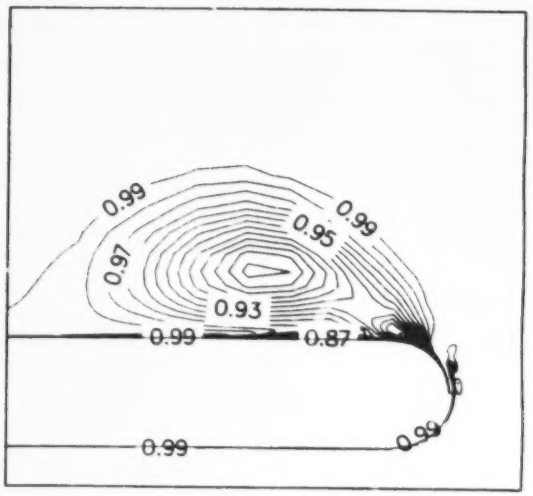

(*a*) $\alpha = 30°, C_\mu = 0.05$.

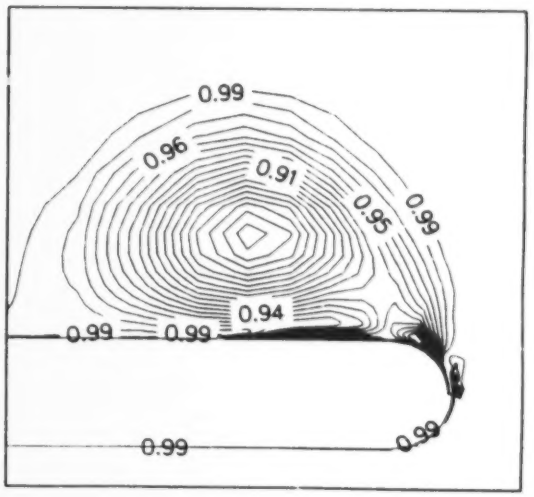

(*b*) $\alpha = 40°, C_\mu = 0.038$.

Figure 4.16: Normalized total pressure contours at $x/c_0 = 0.36$ for $\alpha = 30°$, $C_\mu = 0.05$ and $\alpha = 40°$, $C_\mu = 0.038$.

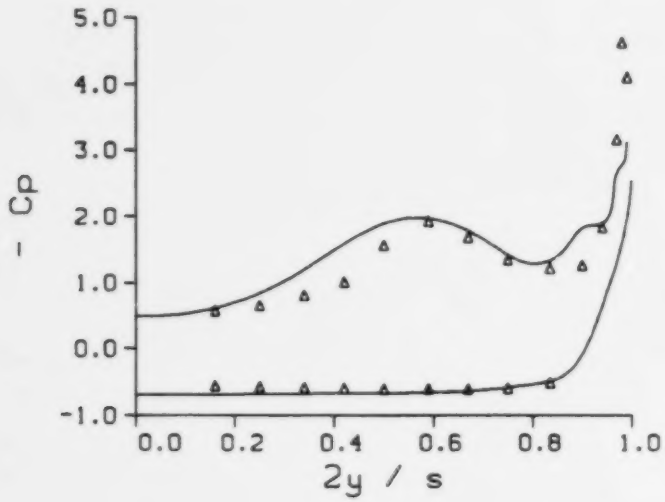

(*a*) $\alpha = 30°, C_\mu = 0.05$.

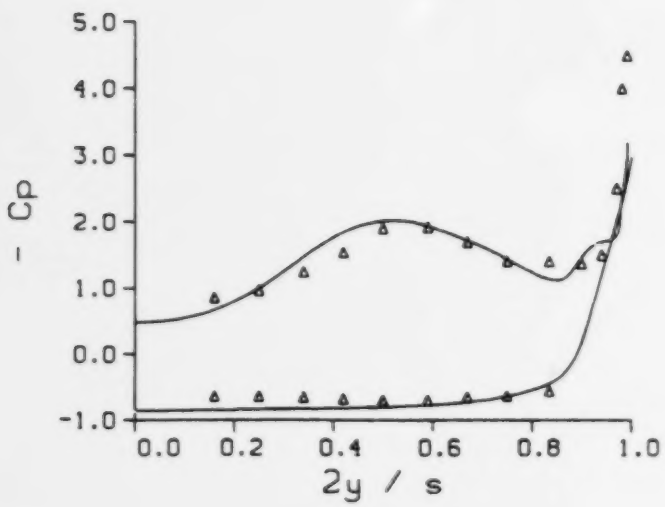

(*b*) $\alpha = 40°, C_\mu = 0.038$.

Figure 4.17: Comparison of computed spanwise surface pressure distribution with experimental results, for $\alpha = 30°$, $C_\mu = 0.05$ and $\alpha = 40°$, $C_\mu = 0.0.38$.

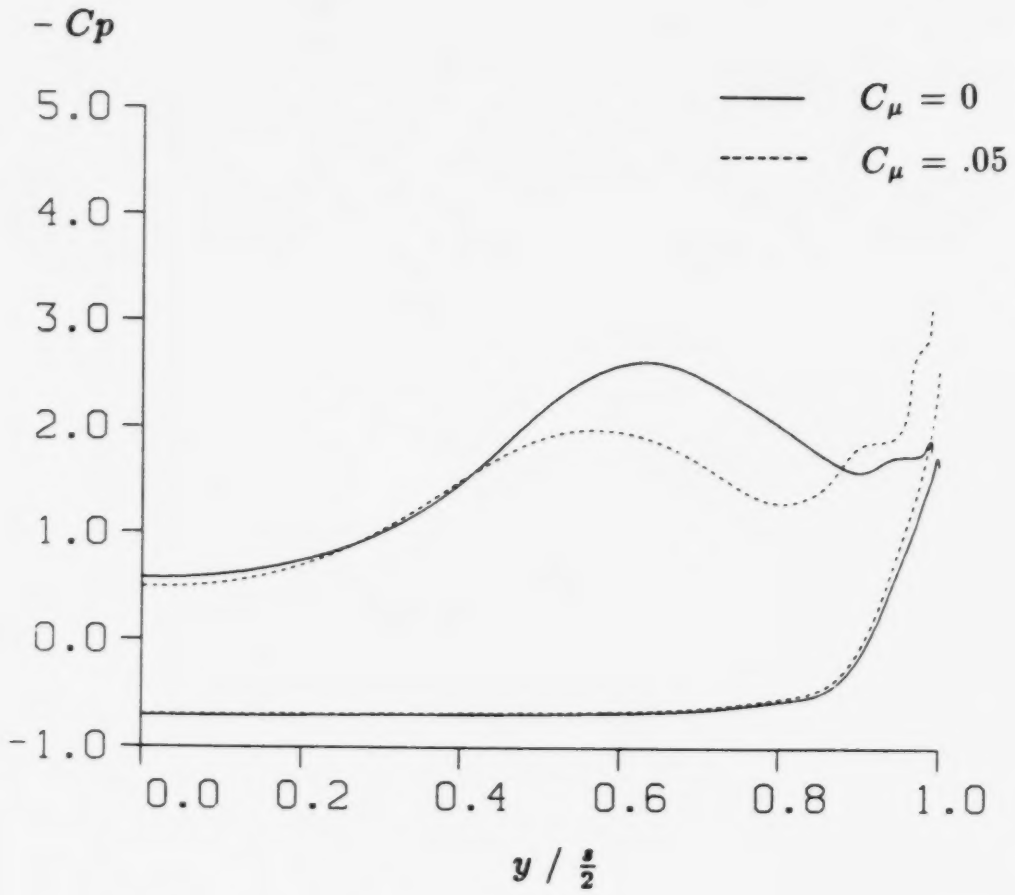

Figure 4.18: Computed spanwise surface pressure distributions for $\alpha = 30°$, $x/c_0 = 0.36$, with $C_\mu = 0$ and $C_\mu = 0.05$.

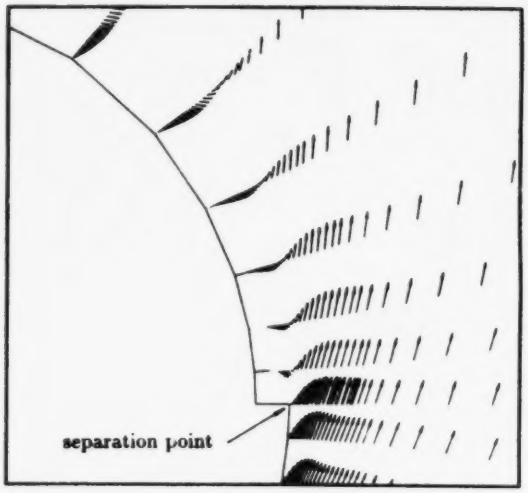

(a) $C_\mu = 0$.

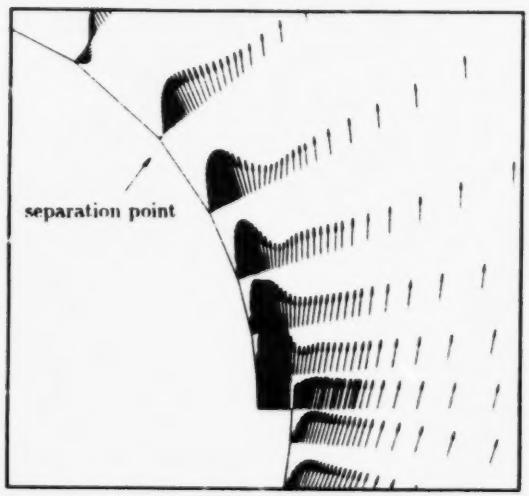

(b) $C_\mu = 0.05$.

Figure 4.19: Computed velocity profiles near the leading edge for $\alpha = 30°$, $x/c_0 = 0.36$, with $C_\mu = 0$ and 0.05.

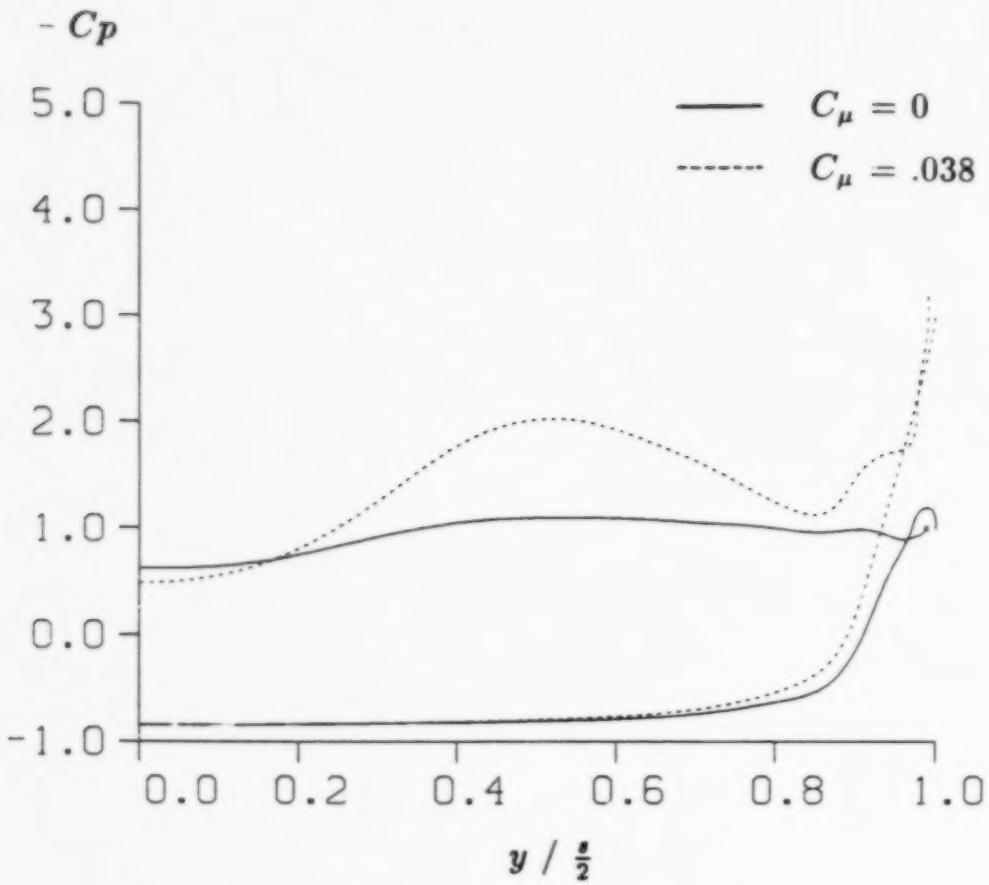

Figure 4.20: Computed spanwise surface pressure distributions for $\alpha = 40°$, $x/c_0 = 0.36$, with $C_\mu = 0$ and 0.038.

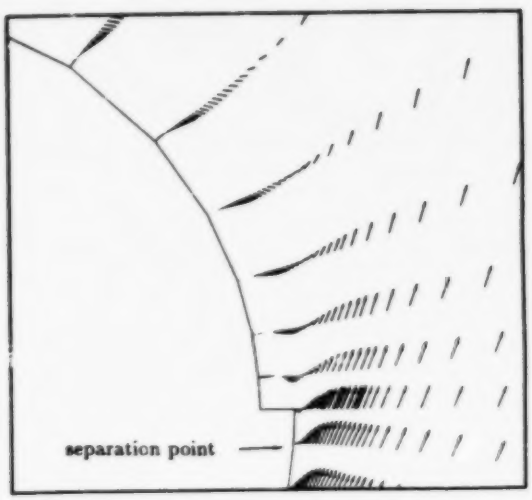

(a) $C_\mu = 0$.

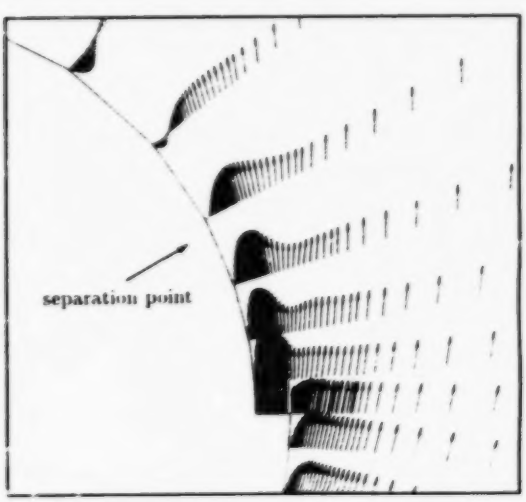

(b) $C_\mu = 0.038$.

Figure 4.21: Computed velocity profiles near the leading edge for $\alpha = 40°$, $x/c_0 = 0.36$, with $C_\mu = 0$ and 0.038.

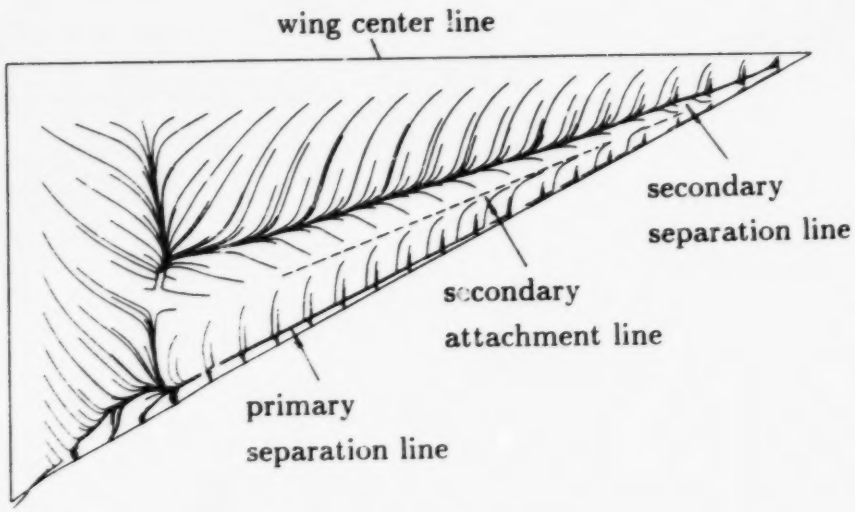

(*a*) $\alpha = 30°, C_\mu = 0.05$.

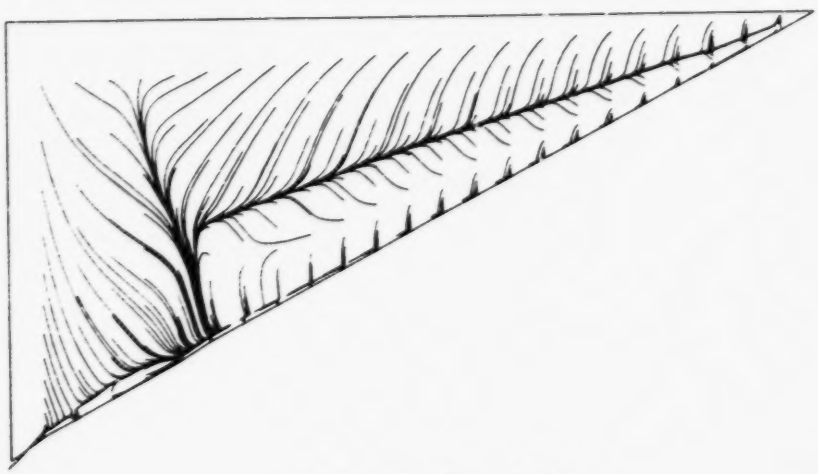

(*b*) $\alpha = 40°, C_\mu = 0.038$.

Figure 4.22: Computed near-surface flow patterns, for $\alpha = 30°$, $C_\mu = 0.05$ and $\alpha = 40°$, $C_\mu = 0.038$.

Angle of Attack (α) in degrees	Normal Force Coefficient (C_N)	
	$C_\mu = 0.00$	$C_\mu = 0.05$
0	0.00	—
10	0.46	0.47
20	0.95	0.90
25	1.17	1.13
30	1.28	1.29
35	1.12	1.39
40	0.98	1.32
45	—	1.15
50	—	0.98

Table 4.1: Effects of tangential leading blowing on total wing normal force ($C_\mu = 0$ and 0.05).

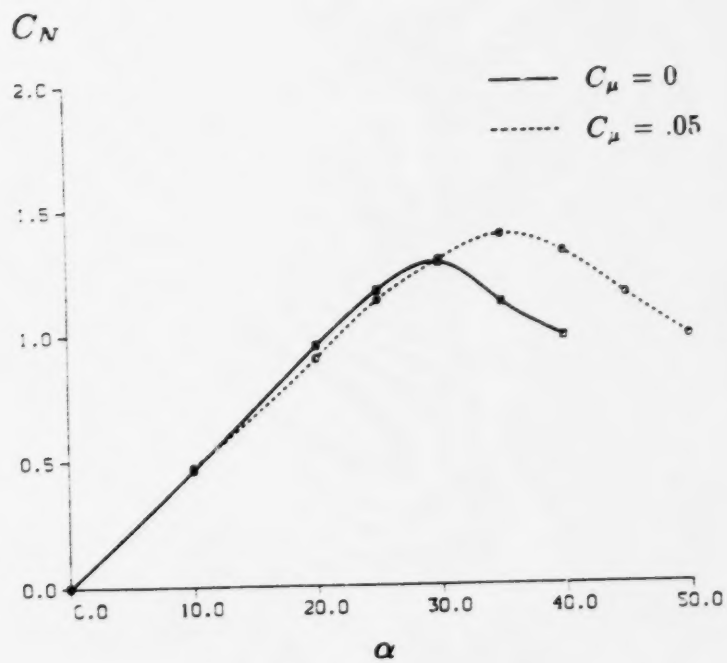

Figure 4.23: Effect of tangential leading edge blowing on total wing normal force ($C_\mu = 0$ and 0.05).

Chapter 5

Conclusions and Recommendations

5.1 Conclusions

Numerical simulations of spanwise and tangential leading edge blowing on delta wings have been successfully carried out by using Computational Fluid Dynamics techniques for solving the three-dimensional Thin-Layer Navier-Stokes equations. This is a substantial departure from the previous theoretical studies, where the assumption of a conical flow field was a requirement for solving the blowing problem. A single grid is used for the spanwise blowing cases, whereas a multiple-grid zonal approach is utilized in the tangential blowing calculations to accomodate the jet-slot geometry. In both cases, the leading edge jet is simulated by defining a permeable boundary, corresponding to the jet slot, where suitable boundary conditions are implemented. The algebraic turbulence model for a wall jet is incorporated to accurately predict the location of the primary separation point in the tangential

blowing calculations. For both blowing schemes, the numerical results are in good general agreement with data from wind tunnel tests. An understanding of the vortical flow field structure over a wide range of angle of attack, with and without blowing, was facilitated by detailed graphical representations.

It is found that spanwise blowing is useful at low to moderate angles of attack, where an increase in lift is obtainable through the enhancement of the strength of the leading edge vortices. The main conclusions for spanwise leading edge blowing are summarized as follows :

(1) Spanwise blowing is mainly an inviscid phenomenon, as suggested by previous inviscid calculations and verified by the present thin-layer approximations.

(2) Blowing increases the lift by magnifying the size and strength of the leading edge vortices at a given angle of attack. As a consequence, the increase in lift is primarily due to the non-linear vortical contribution.

(3) Blowing displaces the flow outboard corresponding to an effective enlargement of the wing-span.

(4) Blowing causes vortex breakdown at a lower angle of attack.

The use of tangential leading edge blowing is found to be useful at high angles of attack for delaying vortex breakdown and restoring orderly vortical flow. The effects of tangential blowing are summarized as follows :

(1) Tangential blowing is mainly a viscous phenomenon since the tangential jet delays primary separation.

(2) If the vortical flow is orderly (*i.e.* pre-stall regime), blowing tends to reduce the vortex induced pressure peak and to increase the jet induced suction peak around the leading edge such that the integrated value of surface pressure remains about the same.

(3) Blowing delays vortex breakdown.

(4) Blowing preserves orderly vortical flow to higher angle of attack, leading to an increase of $C_{N_{max}}$ and stall angle.

In summary, spanwise and tangential leading edge blowing can be used, within different ranges of angle of attack, to control the vortical flow over delta wings or delta-like lifting bodies. The physical phenomena for these two kinds of blowing are quite different in the sense that the effects of spanwise blowing are dominated by inertia forces while the changes in the structure of the flow field due to tangential blowing are brought about by viscous effects. It appears that spanwise blowing is useful at low to moderate angles of attack to gain lift. On the other hand, tangential blowing is useful at high angles of attack to delay vortex breakdown and to restore the orderly vortical flow field. The use of either one of the blowing schemes can be beneficial depending on the operational envelope and angle of attack regime of the aircraft.

5.2 Recommendations

The first recommendation is to do grid refinement studies on both blowing schemes. The lack of sufficient grid resolution may, in part, provides the discrepancy between

computational results and experimental measurements. One approach is to utilize the Solid State Device (SSD) on the Cray X-MP for the multiple-grid zonal program such that zonal information not currently in use could be stored in the SSD. In this way, less demand for on-core memory would allow an increase in the number of grid points. An easier approach would be to use the Cray-2 machine, which has substantially more memory than the Cray X-MP.

The second recommendation is to simulate the blowing schemes by solving the full Navier-Stokes equations. For high angles of attack, massive separation extends over a large region where the coarse grid spacing may not be sufficient to resolve high flow gradients associated with a wake structure. Inaccuracies stemming from the thin layer approximations may be another cause for discrepancy between computation and experiment.

Concerning future work, two additional recommendations are made.

(1) Asymmetric blowing conditions should be considered in order to study blowing as a means of roll control.

(2) The numerical results should be used to formulate simple scaling laws relating the pre-stall and post-stall aerodynamics to angle of attack, aspect ratio and blowing momentum coefficient. The correlation of these parameters from numerical results would allow for a substantial reduction of effort in an experimental program.

Appendix A

Jacobian Matrices

The three-dimensional, inviscid flux Jacobian matrices in generalized curvilinear coordinates are given by ([37])

$$\hat{A}.\ \hat{B} \text{ or } \hat{C} \ = \ \begin{bmatrix} \kappa_t & \kappa_x & \kappa_y & \kappa_z & 0 \\ \kappa_x\phi^2 - u\theta & \kappa_t + \theta - \kappa_x(\gamma-2)u & \kappa_y u - \kappa_x(\gamma-1)v & \kappa_z u - \kappa_x(\gamma-1)w & \kappa_x(\gamma-1) \\ \kappa_y\phi^2 - v\theta & \kappa_x v - \kappa_y(\gamma-1)u & \kappa_t + \theta - \kappa_y(\gamma-2)v & \kappa_z v - \kappa_y(\gamma-1)w & \kappa_y(\gamma-1) \\ \kappa_z\phi^2 - w\theta & \kappa_x w - \kappa_z(\gamma-1)u & \kappa_y w - \kappa_z(\gamma-1)v & \kappa_t + \theta - \kappa_z(\gamma-2)w & \kappa_z(\gamma-1) \\ \theta(2\phi^2 - \gamma e\rho^{-1}) & \kappa_x(\gamma e\rho^{-1} - \phi^2) - (\gamma-1)u\theta & \kappa_y(\gamma e\rho^{-1} - \phi^2) - (\gamma-1)v\theta & \kappa_z(\gamma e\rho^{-1} - \phi^2) - (\gamma-1)w\theta & \kappa_t + \gamma\theta \end{bmatrix} \tag{A.1}$$

where

$$\theta \ = \ \kappa_x u + \kappa_y v + \kappa_z w$$

$$\phi^2 = \frac{1}{2}(\gamma-1)\left(u^2+v^2+w^2\right)$$

with $\kappa = \xi$, η or ζ for $\hat{A}$, $\hat{B}$ or $\hat{C}$, respectively.

The viscous flux Jacobian matrix [36] is

$$\hat{M}^n = \begin{bmatrix} 0 & 0 & 0 & 0 & 0 \\ m_{21} & \alpha_1\delta_\zeta(\rho^{-1}) & \alpha_2\delta_\zeta(\rho^{-1}) & \alpha_3\delta_\zeta(\rho^{-1}) & 0 \\ m_{31} & \alpha_2\delta_\zeta(\rho^{-1}) & \alpha_4\delta_\zeta(\rho^{-1}) & \alpha_5\delta_\zeta(\rho^{-1}) & 0 \\ m_{41} & \alpha_3\delta_\zeta(\rho^{-1}) & \alpha_5\delta_\zeta(\rho^{-1}) & \alpha_6\delta_\zeta(\rho^{-1}) & 0 \\ m_{51} & m_{52} & m_{53} & m_{54} & \alpha_0\delta_\zeta(\rho^{-1}) \end{bmatrix} \tag{A.2}$$

where

$$\begin{aligned}
m_{21} &= -\alpha_1\delta_\zeta(u/\rho) - \alpha_2\delta_\zeta(v/\rho) - \alpha_3\delta_\zeta(w/\rho) \\
m_{31} &= -\alpha_2\delta_\zeta(u/\rho) - \alpha_4\delta_\zeta(v/\rho) - \alpha_5\delta_\zeta(w/\rho) \\
m_{41} &= -\alpha_3\delta_\zeta(u/\rho) - \alpha_5\delta_\zeta(v/\rho) - \alpha_6\delta_\zeta(w/\rho) \\
m_{51} &= -\alpha_1\delta_\zeta\left(u^2/\rho\right) - \alpha_2\delta_\zeta(2uv/\rho) - \alpha_3\delta_\zeta(2uw/\rho) \\
&\quad -\alpha_4\delta_\zeta\left(v^2/\rho\right) - \alpha_6\delta_\zeta\left(w^2/\rho\right) - \alpha_5\delta_\zeta(2vw/\rho) \\
&\quad -\alpha_0\delta_\zeta\left(e/\rho^2\right) - \alpha_0\delta_\zeta\left[\left(u^2+v^2+w^2\right)/\rho\right] \\
m_{52} &= -m_{21} - \alpha_0\delta_\zeta(u/\rho) \\
m_{53} &= -m_{31} - \alpha_0\delta_\zeta(v/\rho) \\
m_{54} &= -m_{41} - \alpha_0\delta_\zeta(w/\rho) \\
\alpha_0 &= \gamma\kappa Pr^{-1}\left(\zeta_x^2+\zeta_y^2+\zeta_z^2\right), \quad \alpha_4 = \mu\left(\zeta_x^2+\frac{4}{3}\zeta_y^2+\zeta_z^2\right) \\
\alpha_1 &= \mu\left(\frac{4}{3}\zeta_x^2+\zeta_y^2+\zeta_z^2\right), \qquad \alpha_5 = \frac{\mu}{3}\zeta_y\zeta_z \\
\alpha_2 &= \frac{\mu}{3}\zeta_x\zeta_y, \qquad\qquad\qquad \alpha_6 = \mu\left(\zeta_x^2+\zeta_y^2+\frac{4}{3}\zeta_z^2\right) \\
\alpha_3 &= \frac{\mu}{3}\zeta_x\zeta_z
\end{aligned}$$

Appendix B

Similarity Transformation Matrices

The similarity transformation matrix [37] for the Jacobian matrices $\hat{A}$, $\hat{B}$ or $\hat{C}$ is

$$T_\kappa = \begin{bmatrix} \tilde{\kappa}_x & \tilde{\kappa}_y & \\ \tilde{\kappa}_x u & \tilde{\kappa}_y u - \tilde{\kappa}_z \rho & \\ \tilde{\kappa}_x v + \tilde{\kappa}_z \rho & \tilde{\kappa}_y v & \\ \tilde{\kappa}_x w - \tilde{\kappa}_y \rho & \tilde{\kappa}_y w + \tilde{\kappa}_x \rho & \\ \left[\tilde{\kappa}_x \frac{\phi^2}{(\gamma-1)} + \rho(\tilde{\kappa}_z v - \tilde{\kappa}_y w)\right] & \left[\tilde{\kappa}_y \frac{\phi^2}{(\gamma-1)} + \rho(\tilde{\kappa}_x v - \tilde{\kappa}_z w)\right] & \end{bmatrix}$$

$$\begin{bmatrix} \tilde{\kappa}_z & \alpha & \alpha \\ \tilde{\kappa}_z u + \tilde{\kappa}_y \rho & \alpha(u + \tilde{\kappa}_x a) & \alpha(u + \tilde{\kappa}_x a) \\ \tilde{\kappa}_z v - \tilde{\kappa}_x \rho & \alpha(v + \tilde{\kappa}_y a) & \alpha(v + \tilde{\kappa}_y a) \\ \tilde{\kappa}_z w & \alpha(w + \tilde{\kappa}_z a) & \alpha(w + \tilde{\kappa}_z a) \\ \left[\tilde{\kappa}_z \frac{\phi^2}{(\gamma-1)} + \rho(\tilde{\kappa}_y v - \tilde{\kappa}_z w)\right] & \alpha\left[\frac{\phi^2+a^2}{(\gamma-1)} + a\tilde{\theta}\right] & \alpha\left[\frac{\phi^2+a^2}{(\gamma-1)} + a\tilde{\theta}\right] \end{bmatrix} \quad \text{(B.1)}$$

where

$$
\begin{aligned}
\tilde{\kappa}_x &= \kappa_x/\sqrt{\kappa_x^2+\kappa_y^2+\kappa_z^2} \\
\tilde{\kappa}_y &= \kappa_y/\sqrt{\kappa_x^2+\kappa_y^2+\kappa_z^2} \\
\tilde{\kappa}_z &= \kappa_z/\sqrt{\kappa_x^2+\kappa_y^2+\kappa_z^2} \\
\alpha &= \frac{\rho}{\sqrt{2}a} \\
\phi^2 &= \frac{1}{2}(\gamma-1)\left(u^2+v^2+w^2\right) \\
\tilde{\theta} &= \kappa_x u+\kappa_y v+\kappa_z w \\
\kappa &= \xi,\ \eta \text{ or } \zeta
\end{aligned}
$$

The analytical expression for the inverse of T_κ is

$$
T_\kappa^{-1}=\begin{bmatrix}
\left[\tilde{\kappa}_x\left(1-\frac{\phi^2}{a^2}\right)-\rho^{-1}\left(\tilde{\kappa}_z v-\tilde{\kappa}_y w\right)\right] & \tilde{\kappa}_x(\gamma-1)ua^{-2} \\
\left[\tilde{\kappa}_y\left(1-\frac{\phi^2}{a^2}\right)-\rho^{-1}\left(\tilde{\kappa}_x w-\tilde{\kappa}_z u\right)\right] & \left[-\tilde{\kappa}_z\rho^{-1}+\tilde{\kappa}_y(\gamma-1)ua^{-2}\right] \\
\left[\tilde{\kappa}_z\left(1-\frac{\phi^2}{a^2}\right)-\rho^{-1}\left(\tilde{\kappa}_y u-\tilde{\kappa}_x v\right)\right] & \left[-\tilde{\kappa}_y\rho^{-1}+\tilde{\kappa}_z(\gamma-1)ua^{-2}\right] \\
\beta\left(\phi^2-a\tilde{\phi}\right) & \beta\left[\tilde{\kappa}_x a-(\gamma-1)u\right] \\
\beta\left(\phi^2+a\tilde{\phi}\right) & -\beta\left[\tilde{\kappa}_x a+(\gamma+1)u\right]
\end{bmatrix}
$$

$$
\begin{bmatrix}
\left[\tilde{\kappa}_z\rho^{-1}+\tilde{\kappa}_x(\gamma-1)va^{-2}\right] & \left[-\tilde{\kappa}_y\rho^{-1}+\tilde{\kappa}_x(\gamma-1)wa^{-2}\right] & -\tilde{\kappa}_x(\gamma-1)a^{-2} \\
\tilde{\kappa}_y(\gamma-1)va^{-2} & \left[-\tilde{\kappa}_x\rho^{-1}+\tilde{\kappa}_y(\gamma-1)wa^{-2}\right] & -\tilde{\kappa}_y(\gamma-1)a^{-2} \\
\left[-\tilde{\kappa}_x\rho^{-1}+\tilde{\kappa}_z(\gamma-1)va^{-2}\right] & \tilde{\kappa}_z(\gamma-1)wa^{-2} & -\tilde{\kappa}_z(\gamma-1)a^{-2} \\
\beta\left[\tilde{\kappa}_y a-(\gamma-1)v\right] & \beta\left[\tilde{\kappa}_z a-(\gamma-1)w\right] & \beta(\gamma-1) \\
-\beta\left[\tilde{\kappa}_y a+(\gamma-1)v\right] & -\beta\left[\tilde{\kappa}_z a+(\gamma-1)w\right] & \beta(\gamma-1)
\end{bmatrix} \tag{B.2}
$$

where $\beta = 1/\sqrt{2}\rho a$

The analytical expressions for $(T_\xi^{-1}T_\eta)$, $(T_\eta^{-1}T_\zeta)$ used in Eq. (2.39) and their inverse matrices $(T_\eta^{-1}T_\xi)$, $(T_\zeta^{-1}T_\eta)$ can be written in a simple form,

$$T_\kappa^{-1}\,T_l \;=\; \begin{bmatrix} m_1 & m_2 & m_3 & -\mu m_4 & \mu m_4 \\ -m_2 & m_1 & m_4 & \mu m_3 & -\mu m_3 \\ -m_3 & -m_4 & m_1 & -\mu m_2 & \mu m_2 \\ \mu m_4 & -\mu m_3 & \mu m_2 & \mu^2(1+m_1) & \mu^2(1-m_1) \\ -\mu m_4 & \mu m_3 & \mu m_2 & \mu^2(1-m_1) & \mu^2(1+m_1) \end{bmatrix} \tag{B.3}$$

where

$$\begin{aligned} \mu &= \frac{1}{\sqrt{2}} \\ m_1 &= \tilde{\kappa}_x\tilde{l}_x + \tilde{\kappa}_y\tilde{l}_y + \tilde{\kappa}_z\tilde{l}_z \\ m_2 &= \tilde{\kappa}_x\tilde{l}_y - \tilde{\kappa}_y\tilde{l}_x \\ m_3 &= \tilde{\kappa}_x\tilde{l}_z - \tilde{\kappa}_z\tilde{l}_x \\ m_4 &= \tilde{\kappa}_y\tilde{l}_z - \tilde{\kappa}_z\tilde{l}_y \\ \kappa,\, l &= \xi,\ \eta \text{ or } \zeta \end{aligned}$$

Appendix C

Calculation of the Jet Momentum

The jet momentum (J) in the absence of compressibility can be expressed as follows

$$J = \rho \int \int V \vec{V} \cdot \vec{n} \; dy \, dx \tag{C.1}$$

The expression for the velocity distribution for a small trapezoidal cell, as shown in figure C.1, can be written as

$$V(x,y) = \frac{V_6 - V_5}{\Delta y(x)} \, y + V_5 \tag{C.2}$$

where V_1, V_2, V_3 and V_4 are the velocity magnitudes at the cell corners, with

$$\begin{aligned} V_5(x) &= \frac{V_3 - V_1}{\Delta x} \, x + V_1 \\ V_6(x) &= \frac{V_4 - V_2}{\Delta x} \, x + V_2 \\ \Delta y(x) &= \frac{L_2 - L_1}{\Delta x} \, x + L_1 \end{aligned} \tag{C.3}$$

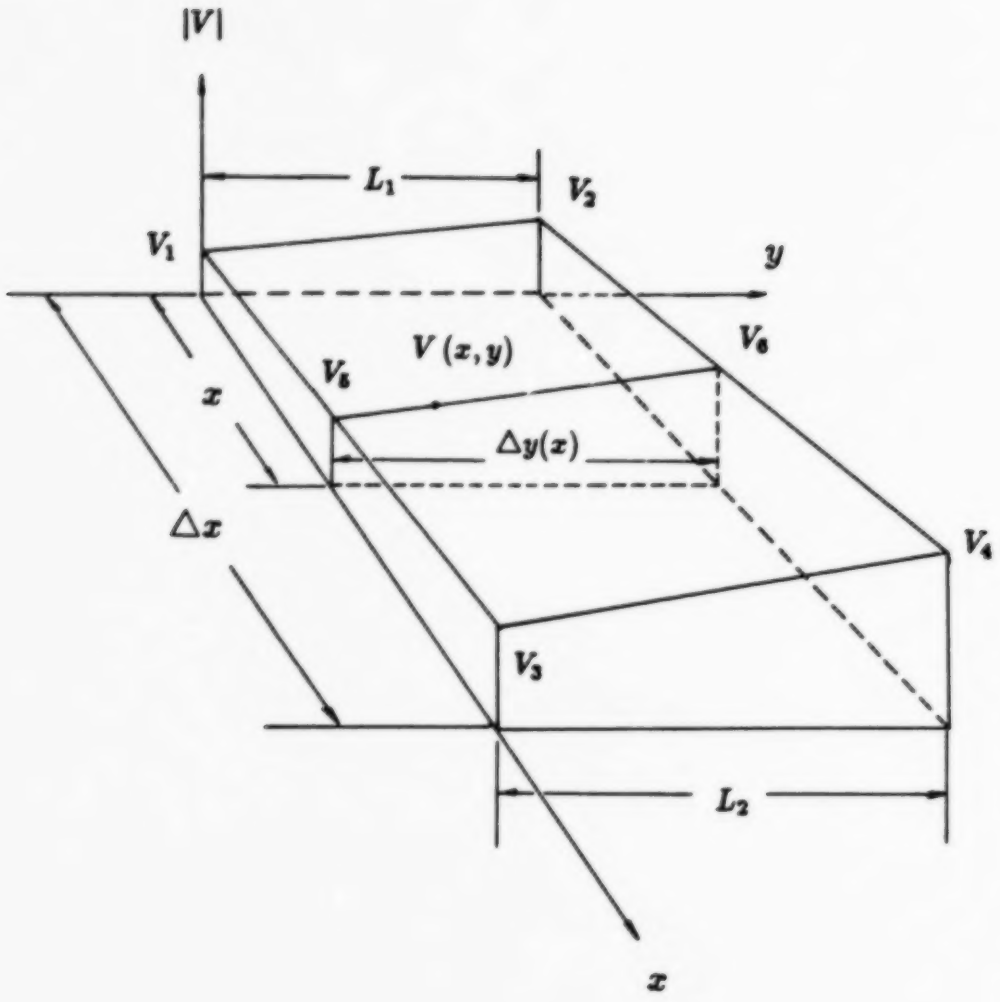

Figure C.1: Velocity magnitude distribution over a small trapezoidal cell

Integrating Eq. (C.2) at a constant x yields

$$\int_0^{\Delta y(x)} V^2(x,y)\, dy = \frac{\Delta y(x)}{3}\left[V_5^2 + V_5 V_6 + V_6^2\right] \tag{C.4}$$

Substituting the expressions for $V_5(x)$, $V_6(x)$ and $\Delta y(x)$ from (A.3) into (A.4) and integrating along the x-axis yields

$$\begin{aligned} J &= \rho \int_0^{\Delta x} \int_0^{\Delta y(x)} V^2(x,y)\; dy\, dx \\ &= \frac{\rho}{3}\left[PF\frac{\Delta x^4}{4} + (PE+FQ)\frac{\Delta x^3}{3} + (QE+FR)\frac{\Delta x^2}{2} + RE\Delta x\right] \end{aligned} \tag{C.5}$$

where

$$\begin{aligned} E &= L_1 \\ F &= \frac{L_2 - L_1}{\Delta x} \\ P &= (A+C)^2 \\ Q &= 2(AB+CD) + AD + BC \\ R &= B^2 + BD + D^2 \\ A &= \frac{V_3 - V_1}{\Delta x} \\ B &= V_1 \\ C &= \frac{V_4 - V_2}{\Delta x} \\ D &= V_2 \end{aligned}$$

Bibliography

[1] Bird, J. D., " Tuft-Grid Surveys at Low Speeds for Delta Wings ", NASA TN D-5045.

[2] Hummel, D., " On the Vortex Formation over a Slender Wing at Large Angles of Incidence ", High Angle of Attack Aerodynamics , AGARD CP-247, Paper No. 15, Jan. 1979.

[3] Cornish III, J. J., " High Lift Applications of Spanwise Blowing ", ICAS Paper 70-09, Sept. 1970.

[4] Bradley, R. G., Wray, W. D. and Smith, C. W., " An Experimental Investigation of Leading-Edge Vortex Augmentation by Blowing ", NASA CR-132415, 1974.

[5] Campbell, J. F., " Effect of Spanwise Blowing on the Pressure Field and Vortex-Lift Characteristics of a 44° Swept Trapezoidal Wing ", NASA TN D-7907, 1975.

[6] Campbell, J. F., " Augmentation of Vortex Lift by Spanwise Blowing ", Journal of Aircraft , Vol. 13, Sept. 1976, pp. 727-732.

[7] Ericksen, G. E., " Effect of Spanwise Blowing on the Aerodynamic Characteristics of the F-5E ", Journal of Aircraft , Vol. 16, No. 3, Oct. 1979.

[8] Anglin, E. L. and Satran, D., " Effects of Spanwise Blowing on Two Fighter Airplane Configurations ", Journal of Aircraft , Vol. 17, Dec. 1980, pp. 883-889.

[9] Aeginer, A. and Salomon, M., " Augmentation of Fighter Aircraft Performance by Spanwise Blowing Over the Wing Leading Edge ", NASA TM 84330, March 1983.

[10] Shi, Z., Wu, J. M. and Vakili, A. D., " An Investigation of Leading-Edge Vortices on Delta Wings with Jet Blowing ", AIAA Paper 87-0330, Jan. 1987.

[11] Visser, K. D., Iwanski, K. P., Nelson, R. C. and Ng, T. T., " Control of Leading Edge Vortex Breakdown by Blowing ", AIAA Paper 88-0504, Jan. 1988.

[12] Trebble, W. J. B., " Exploratory Investigation of the Effects of Blowing from the Leading Edge of a Delta Wing ", Aero. Research Council R&M 3518, April, 1966.

[13] Alexander, A. J., " Experiments on a Delta Wing Using Leading Edge Blowing to Remove the Secondary Separation ", Report No. 161, The college of Aeronautics, Cranfield, May 1963.

[14] Alexander, A. J., " Experimental Investigation on a Cropped Delta Wing with Edge Blowing ", Aero. Research Council 25213. June 1963.

[15] Tavella, D. A., Wood, C. S., Lee, C. S. and Roberts, L., " Two Blowing Concepts for Roll and Lateral Control of Aircraft ", JIAA TR - 75, Stanford University, Oct. 1986.

[16] Tavella, D. A. and Wood, N. J., " Influence of Tip Blowing on Rectangular Wings ", AIAA Paper No. 855001, 1985.

[17] Lee, C. S., Tavella, D., Wood, N. J., and Roberts, L., " Flow Structure of Lateral Wing-Tip Blowing ", Paper No. 871810, Proceedings AIAA 4th Applied Aerodynamics Conference, San Diego, CA 1986.

[18] Wood, N. J. and Roberts, L., " The Control of Vortical Lift on Delta Wings by Tangential Leading Edge Blowing ", AIAA Paper No. 87-0158, 1987.

[19] Wood, N. J., Roberts, L. and Lee, K. T., " The Control of Vortical Flow on a Delta Wing at High Angles of Attack ", AIAA Paper No. 87-2278, 1987.

[20] Barsby, J. E., " Calculations of the Effect of Blowing from the Leading Edges of a Slender Delta Wing ", Aero Research Council R&M 3692, 1972.

[21] Barsby, J. E., " Calculation of the Effects of Blowing from the Leading Edge of a Cambered Delta Wing ", ARC R&M 3800, 1978.

[22] Smith, J. H. B., " Improved Calculations of Leading Edge Separation from Slender Delta Wings ", RAE TR 66070, February 1966.

[23] Spence, D. A., " The Lift Coefficient of a Thin, Jet Flapped Wing ", Proc. Roy. Soc. , 238, 46-68, 1965.

[24] Tavella, D. A., " The lift of Sharp-Leading-Edge Delta Wings with Blowing ", JIAA TR-68, Stanford University, December 1985.

[25] Brown, C. E. and Michael, W. H., " On Slender Delta Wings with Leading Edge Separation ", NACA TN 3430, April 1955; Journal of the Aerospace Sciences, Vol 21, pp. 134-135, 1954.

[26] Mourtos, N. J. and Roberts L., " Control of Vortical Separation on a Circular Cone ", AIAA Paper No. 88-0482, 1988.

[27] Bryson, A. E., " Symmetric Vortex Separation on Circular Cylinders and Cones ", Journal of Applied Mechanics , December 1959.

[28] Roberts, L., " A Theory for Turbulent Curved Wall Jets ", AIAA Paper No. 87-0004, 1987.

[29] Fujii, K. and Obayashi, S., " Practical Applications of New LU-ADI Scheme for the Three-Dimensional Navier-Stokes Computation of Transonic Viscous Flow ", AIAA Paper No. 86-0513, 1986.

[30] Fujii, K. and Obayashi, S., " Navier-Stokes Simulation of Transonic Flow over Wing-Fuselage Combinations ", AIAA Paper No. 86-1831, 1986.

[31] Fujii, K. and Schiff, L. B., " Numerical Simulation of Vortical Flows over a Strake-Delta Wing ", AIAA Paper No. 87-1229, 1987.

[32] Peyret, R. and Viviand, H., " Computation of Viscous Compressible Flows Based on the Navier-Stokes Equations ", AGARD-AG-212, 1975.

[33] Anderson, D. A., Tannehill, J. C. and Pletcher, R. H., Computational Fluid Mechanics and Heat Transfer, McGraw-Hill, 1984.

[34] Beam, R. M. and Warming, R. F., " An Implicit Finite-Difference Algorithm for Hyperbolic Systems in Conservation-Law Form ", Journal of Computational Physics , Vol. 22, 1976, pp. 87-109.

[35] Steger, J. L., and Warming, R. F., " Flux Vector Splitting of the Inviscid Gas Dynamic Equations with Applications for Finite-Difference Methods ",

Journal of Computational Physics , Vol. 40, pp.263-293, 1981.

[36] Pulliam, T. H. and Chaussee, D. S., " A Diagonal Form of an Implicit Approximate Factorization Algorithm ", Journal of Computational Physics 39, pp. 347-363.

[37] Pulliam, T. H. and Steger, J. L., " Recent Improvements in Efficiency, Accuracy, and Convergence for Implicit Approximate Factorization Algorithms ", AIAA Paper No. 85-0360, 1985.

[38] Briley, W. R. and McDonald, H., " Solution of the Multidimensional Compressible Navier-Stokes Equations by a Generalized Implicit Method ", Journal of Computational Physics 24, pp. 372-397, 1977.

[39] Chakravarthy, S. R., Osher, S., " A New Class of High Accuracy TVD Schemes for Hyperbolic Conservation Laws ", AIAA Paper No. 85-0363, Jan. 1985.

[40] Obayashi, S., Fujii, K. and Gavali, S., " Navier-Stokes Simulation of Wind-Tunnel Flow Using LU-ADI Factorization Algorithm ", NASA TM 100042, February 1988.

[41] Baldwin B. S. and Lomax, H., " Thin Layer Approximation and Algebraic Model for Separated Turbulent Flows ", AIAA Paper No. 78-257, 1978.

[42] Schliching, H., Boundary-Layer Theory , Mcgraw-Hill, 1979.

[43] Sigalla, A., " Measurements of Skin Friction in a Plane Turbulent Wall Jet ", J. Royal Aeronautical Society Vol. 62 873, 1958.

[44] Bradshaw, P. and Gee, M. T., " Turbulent Wall Jets with and without an External Stream ", Aero. Research Council, R&M 3252, 1960.

[45] Steger J. L. and Chaussee, D. S., " Generation of Body-Fitted Coordinates Using Hyperbolic Partial Differential Equations ", J. of Sci. Stat. Comp. Vol. 1, No.4, Dec. 1980.

[46] Steger, J. L. and Rizk, Y. M., " Generation of Three-Dimensional Body-Fitted Coordinates Using Hyperbolic Partial Differential Equations ", NASA TM-86753, 1985.

[47] Buning, G. P. and Steger, J. L., " Graphics and Flow Visualization in Computational Fluid Dynamics ", AIAA Paper No 85-1507, July 1985.

[48] Fujii, K. and Obayashi, S., " Evaluation of Euler and Navier-Stokes Solutions for Leading-Edge and Shock-Induced Separations ", National Aerospace Laboratory, Japan, TR-886T, October, 1985.

[49] Küchemann, D., The Aerodynamic Design of Aircraft , Pergamon Press, Oxford, England 1978.

[50] DeJarnette, F. R. and Woodson, S. H., " Numerical and Experimental Determination of Secondary Separation on Delta Wings in Subsonic Flow ", Journal of Aircraft , Vol. 22, No. 7, 1985, pp. 602-608.

[51] White, F. M., Viscous Fluid Flow McGraw-Hill, New York, 1974.

[52] Ericsson, L. E., " The Fluid Mechanics of Slender Wing Rock ", Journal of Aircraft Vol. 21, No 5, pp.322-328.

[53] Wood, N. J. and Nielsen J., " Circulation Control Airfoils - Past, Present and Future ", AIAA Paper No. 85-0204, 1985.

[54] Hartwich, P.-M., Hsu, C.-H., Luckring, J. M. and Liu, C. H., " Numerical Study of the Vortex Burst Phenomenon for Delta Wings ", AIAA Paper No. 88-0505, Jan. 1988.